UNIVERSITY OF CALIFORNIA, SAN DIEGO

Illuminating Spatial and Temporal Patterns of Ocean Mixing as Inferred from Argo Profiling Floats

A dissertation submitted in partial satisfaction of the
requirements for the degree
Doctor of Philosophy

in

Oceanography

by

Caitlin Beth Whalen

Committee in charge:

Professor Lynne Talley, Chair
Professor Jennifer MacKinnon, Co-Chair
Professor Peter Franks
Professor Eugene Pawlak
Professor Robert Pinkel
Professor Dean Roemmich

2015

The dissertation of Caitlin Beth Whalen is approved, and it is acceptable in quality and form for publication on microfilm and electronically:

_____

_____

_____

_____

_____
Co-Chair

_____
Chair

University of California, San Diego

2015

TABLE OF CONTENTS

LIST OF FIGURES

ACKNOWLEDGEMENTS

Since it is difficult to place the precise beginning of my thesis-journey, I would like to thank both of my parents who catalyzed my interest in learning by providing ample opportunity for exploration over the years.

I am indebted to both of my advisors, Jennifer MacKinnon and Lynne Talley, who shared with me their keen physical oceanographic insight and provided me with the freedom to investigate the questions in the field that I find the most tantalizing. Thanks to my committee, Peter Franks, Eugene Pawlak, Robert Pinkel, and Dean Roemmich for spending the time to share their perspective on my work and Amy Waterhouse for co-authoring a paper with me. Faculty both at Scripps and elsewhere contributed significantly to my growth as an oceanographer, I'd especially like to acknowledge Myrl Hendershott, Sonya Legg, and Peter Rhines in this regard.

Many thanks to UC Ship Funds for providing me with the opportunity to lead a research cruise and the students who fearlessly volunteered to go to sea with me including Magdalena Carranza, Tonia Capuano, Felipe Gomez Valdivia, Martin Hoecker-Martinez, Bryce Inman, and Caroline Miller. Your tireless work was invaluable. The cruise would not have been possible without the Captain and Crew abroad the R/V Roger Revelle, and the technical expertise of Steve Lambert and generous loan of instrumentation and gear by Jonathan Nash, Emily Shroyer, Harper Simmons, and Lou St. Laurent.

Finally, I would like to extend thanks to the many, many people who provided a moment of fun or enthusiastic help throughout my tenure in graduate school.

Chapters 2, and 3 of the dissertation have been published in peer reviewed journals. Chapter 2 is published in its entirety in:

- **Whalen**, C.B., L. D. Talley and J. A. MacKinnon, 2012. Spatial and temporal variability of global ocean mixing inferred from Argo profiles. *Geophys. Res. Lett.*, 39, L18.

Chapter 3 has been published in its entirety in:

- **Whalen**, C. B., J. A. MacKinnon, L. D. Talley and A. F. Waterhouse, 2015. Estimating the mean diapycnal mixing using a finescale strain parameterization. *J. Phys. Oceanogr.*, 45, 1174-1188

VITA

2008	B.A. in Physics, Reed College, Portland, Oregon
2015	Ph.D. in Oceanography, University of California, San Diego

PUBLICATIONS

Wijesekera, H. W., et al., 2015. Decrypting a Mystery Bay - The ASIRI Ocean-Atmosphere Initiatives on Bay of Bengal. *(submitted)*

Salehipour, H., W. R. Peltier, C. B. **Whalen**, J. A. MacKinnon, 2015. A parameterization of ocean diapycnal mixing efficiency and turbulent Prandtl number: global estimates inferred from Argo-float based profiles. *(in revision)*

Buijsman, M. C., et al., 2015. The effect of wave drag on the tidal energy balance in a realistically forced forward global ocean model. *(in revision)*

Whalen, C. B., J. A. MacKinnon, L. D. Talley and A. F. Waterhouse, 2015. Estimating the Mean Diapycnal Mixing Using a Finescale Strain Parameterization. *J. Phys. Oceanogr.,* 45, 1174-1188

Waterhouse, A. F., et al., 2014. Global patterns of diapycnal mixing from measurements of the turbulent dissipation rate. *J. Phys. Oceanogr.,* 44, 1854-1872.

Whalen, C.B., L. D. Talley and J. A. MacKinnon, 2012. Spatial and temporal variability of global ocean mixing inferred from Argo profiles. *Geophys. Res. Lett.,* 39, L18.

ABSTRACT OF THE DISSERTATION

Illuminating Spatial and Temporal Patterns of Ocean Mixing as Inferred from Argo Profiling Floats

by

Caitlin Beth Whalen

Doctor of Philosophy in Oceanography

University of California, San Diego, 2015

Professor Lynne Talley, Chair
Professor Jennifer MacKinnon, Co-Chair

Small-scale turbulent mixing in the ocean is an important piece in many larger scale questions in ocean physics and climate. Measurements that can resolve the details of these centimeter and meter scale dynamics are often demanding to undertake, and typically not practical for addressing questions posed on regional and global scales. Here we utilize the global Argo array of profiling floats, and a previously developed finescale method for approximating the open ocean dissipation rate, to produce 800,000 estimates of this value distributed throughout the ocean. We show that average profiles calculated using this finestructure method agree with average microstructure profiles at the same location within a 2-3 for

96% of the comparisons. This indicates that it is a viable method for exploring large-scale patterns of ocean mixing. The near global maps of the average dissipation rate we generate indicate that the values are spread over multiple orders of magnitude, and that there are distinct spatial patterns present. These spatial patterns are correlated with seafloor roughness, near-inertial kinetic energy, tidal kinetic energy, and eddy kinetic energy. Dissipation rate estimates are also elevated in the equatorial band. The correlation to eddy kinetic energy is not observed to be related to the proximity to a particular eddy, nor the sign of the vorticity of that eddy, but it is correlated with the magnitude of the velocity of the nearest eddy. In zonally averaged profiles a seasonal cycle of a factor of 2-5 is observed beneath storm tracks, especially between (30°-40°) in both hemispheres. This seasonal cycle extends to the full depth of our 2000 m measurements and has a larger amplitude in places with strong eddy kinetic energy. Our observations suggest that this could be caused by a modulating effect of stronger eddy kinetic energy regions on the near-inertial energy flux from the winds at the surface into the thermocline.

Chapter 1

Introduction

In the ocean turbulent mixing across surfaces of constant density is a process that takes place on very small scales, yet has consequences for dynamics up to the largest scale. Mixing water is important for global-scale circulatory processes in the ocean, dissipating the kinetic energy that the tumultuous water possesses, and vertically transporting quantities such as heat, salt, and nutrients. These in turn have wider reverberations through different facets of oceanography. For example, mixing results in energy dissipation, vertical mixing of heat, and water mass transformation, which all have climatic implications, and are therefore are key to our understanding of the current climate and for accurately representing the past and future climate in models. From a biological perspective, transporting nutrients from the abyss to shallower water that is exposed to the light can make it available for plankton growth, and thus have critical ecological implications. Turbulent mixing has a large-scale importance. However, we currently only have a nascent understanding of *where*, *when*, and *how* turbulent mixing occurs from a large-scale perspective.

The primary mechanism for this diapycnal mixing in the deep ocean is the breaking of internal waves. Similarly to surface waves that exist on the density interface between air and water, internal waves are supported by the layers of density stratification in the ocean interior. These waves have fascinating properties; they can have skyscraper-high vertical scales due to the small density differences involved compared to surface waves. Also, since the ocean is generally composed

of a smooth gradient in density rather than one single air-sea interface, these waves can propagate in the vertical in addition to the horizontal. Some of these waves have expression on the ocean's surface, as seen with the sun-glint satellite image from the Banda Sea shown in Figure 1.1.

When internal waves break they mix ocean water and dissipate kinetic energy. Quantities measured to facilitate our understanding of this process include an diapycnal diffusivity and a rate of energy dissipation. Tracking when, where, and why this breaking and subsequent mixing occurs across the globe is a mystery that we would care to solve. Internal waves are prevalent, and subsequently often break close to where they are generated through a variety of mechanisms. The tides transfer water over bathymetric features in the ocean, forcing internal waves. These waves may either propagate away, or locally break and dissipate their energy. Figure 1.2a shows an example of this near the Hawaiian ridge (*Klymak et al.*, 2008). The tide flowing over the ridge triggers internal waves, shown by the isopycnals oscillating with time, which are in phase with the elevated energy dissipation rate. The rotating, gusty winds that are prevalent in storms (specifically 'near-inertial' winds) are another source of inertial waves. Figure 1.2b shows one example of wintertime propagation of internal wave energy from the surface downward (*Alford et al.*, 2012). Internal waves that originate from these and other sources can subsequently dissipate if they encounter rough seafloor topography by scattering and breaking. An example where this may be one of the processes present is shown in Figure 1.2c where the diffusivity, diagnostic of the diapycnal mixing, is elevated above the bumpy topography and low over the smooth topography (*Polzin et al.*, 1997).

The ocean's mesoscale is a lesser-studied piece to the story of the life cycle and dissipation of internal waves. Mesoscale dynamics include phenomena that typically have horizontal scales 10s to 100s of kilometers across, and include rotating vortices of water called eddies, fronts such as the Kuroshio Current and the Gulf Stream, and a host of other swirlingly complex dynamics. Figure 1.3 shows an example of a mesoscale eddy containing a plankton bloom in addition to other structures in the ocean on similar scales. One way the strength of the mesoscale

can be quantified by calculating the eddy kinetic energy, essentially the energy in the perturbations from the time-mean water velocity. These mesoscale features are thought to potentially generate, and facilitate the dissipation of internal waves, and thus determine the distribution of mixing in the ocean.

The methods frequently employed to measure internal waves and the subsequent dissipation of their energy are well-suited for scrutinizing regions over timescales of weeks or months. However, they become more difficult or impossible to utilize over longer time or larger spatial scales. Since we wish to explore turbulent diapycnal mixing on these larger scales, for this work we apply a method to use coarser, more commonly acquired data to estimate the mixing due to internal waves in the ocean. This finescale method uses profiles of the density in the ocean, and focuses on the finestructure in 200 m segments of that profile. Internal waves cause the isopycnals to oscillate, which is mapped into the density profile as wiggles. We can measure these wiggles and form an estimate of the energy in the internal waves at that spot at that instant in time. This estimate can be subsequently used to measure the approximate rate of energy dissipation from the internal waves. This approach only uses density profiles with meter or coarser resolutions, which are significantly easier to collect than methods used to measure turbulence directly on centimeter scales.

Argo floats collect the density profiles utilized in this work to estimate the energy dissipation rate. As of September 17, 2015 a total of 3881 Argo floats are in the ocean, scattered around the globe (Figure 1.4). Typically these floats remain at 1000 m for the majority of their lifetime, punctuated every 10 days by a 2000 m dive and rise to the ocean's surface as they record measurements of pressure, temperature and salinity. At the surface they communicate via satellite, providing near real-time data. The Argo program is a global effort that has produced an immense dataset that is used for a myriad of applications, from global warming studies to, as we demonstrate here, queries concerning ocean turbulence.

Chapter 1 applies the finescale method to Argo float profiles to generate nearly global maps of the dissipation rate and diffusivity (*Whalen et al.*, 2012). The averaged dissipation rate and diffusivity ranges over multiple orders of magnitude

around the globe, and distinct spatial patterns can be observed in these maps. Correlations are shown between the dissipation rate and environmental variables including the sea floor roughness, the tidal kinetic energy, the near-inertial kinetic energy from the winds, and the eddy kinetic energy. An example seasonal cycle in the dissipation rate is also shown from the North Pacific.

The finestructure method for estimating the dissipation rate using Argo profiles is explored deeply in Chapter 2, and compared to a more direct method of inferring the dissipation rate using microstructure measurements from various locations from around the globe (*Whalen et al.*, 2015). We find good (a factor of 2-3) agreement between these two methods, thus justifying the use of this approach to investigate global mixing patterns. The role of temporal variability in these comparisons is also explored, revealing a seasonal cycle in the mixing beneath storm tracks.

Chapter 3 focuses on exploring the correlation between the dissipation rate and eddy kinetic energy that was observed in Chapter 1 in more detail. We find that dissipation rate is positively correlated with the magnitude of the velocity of the closest mesoscale eddy. The amplitude of the seasonal cycle in areas of high eddy kinetic energy is slightly larger than in areas of low eddy kinetic energy. The observations also suggest that the dissipation rate has a stronger positive correlation with near-inertial winds in regions of high eddy kinetic energy as opposed to low eddy kinetic energy.

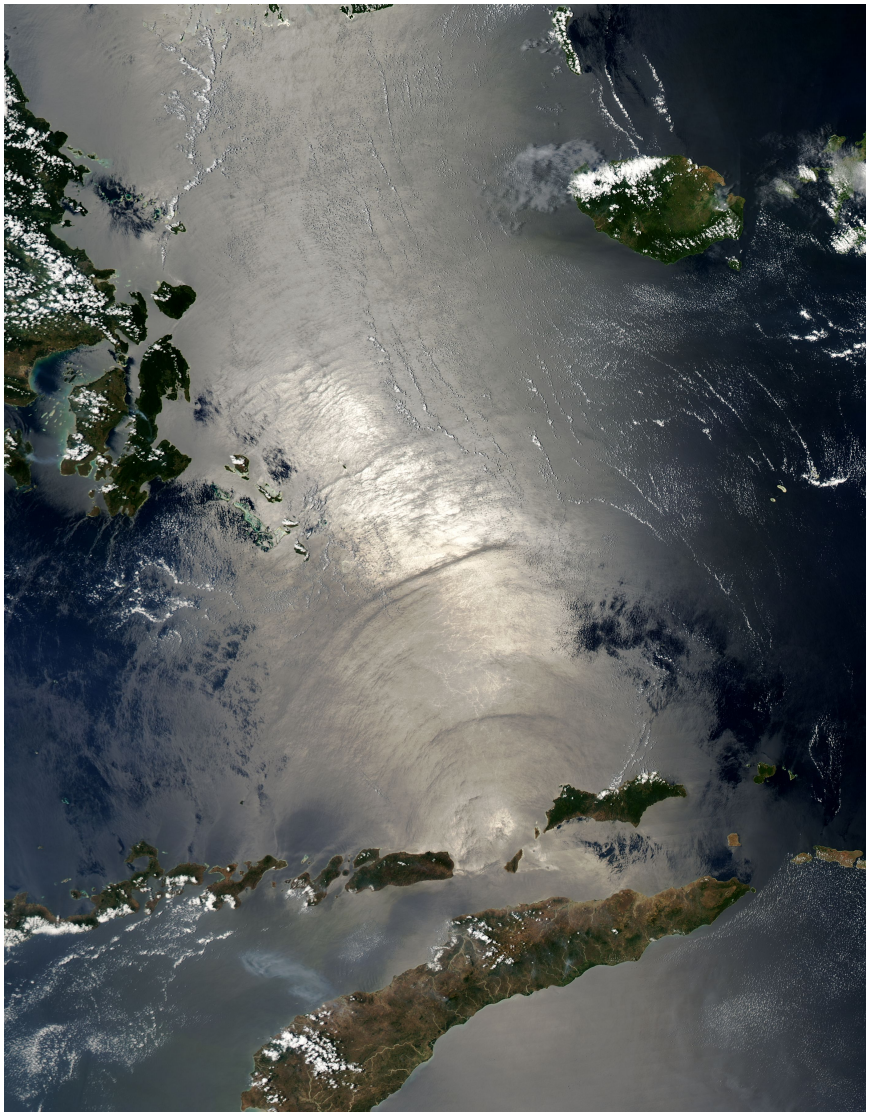

Figure 1.1: The surface expression of internal waves propagating across the Banda Sea imaged using sun-glint via the Aqua/Modis Satellite in 2004 (http://earthdata.nasa.gov/lance/rapid-response)

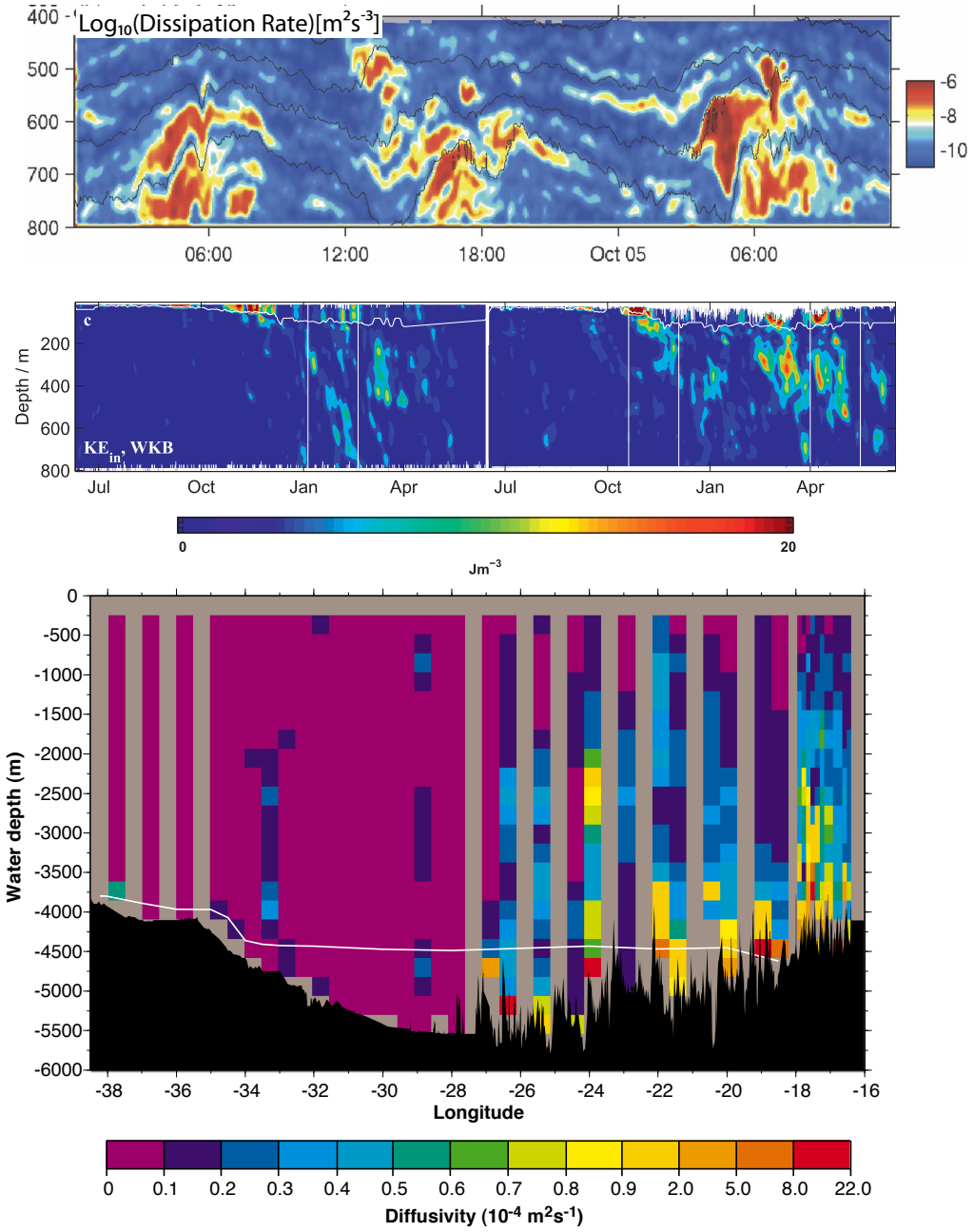

Figure 1.2: Elevated turbulent energy dissipation from breaking inertial waves is found in a variety of locations including: (a) close to generation from the tides near the Hawaiian Ridge (*Klymak et al.*, 2008), (b) near generation from windy storms perturbing the ocean's surface (*Alford et al.*, 2012), and (c) near rough topography scattering waves and allowing them to dissipation their energy (*Polzin et al.*, 1997). .

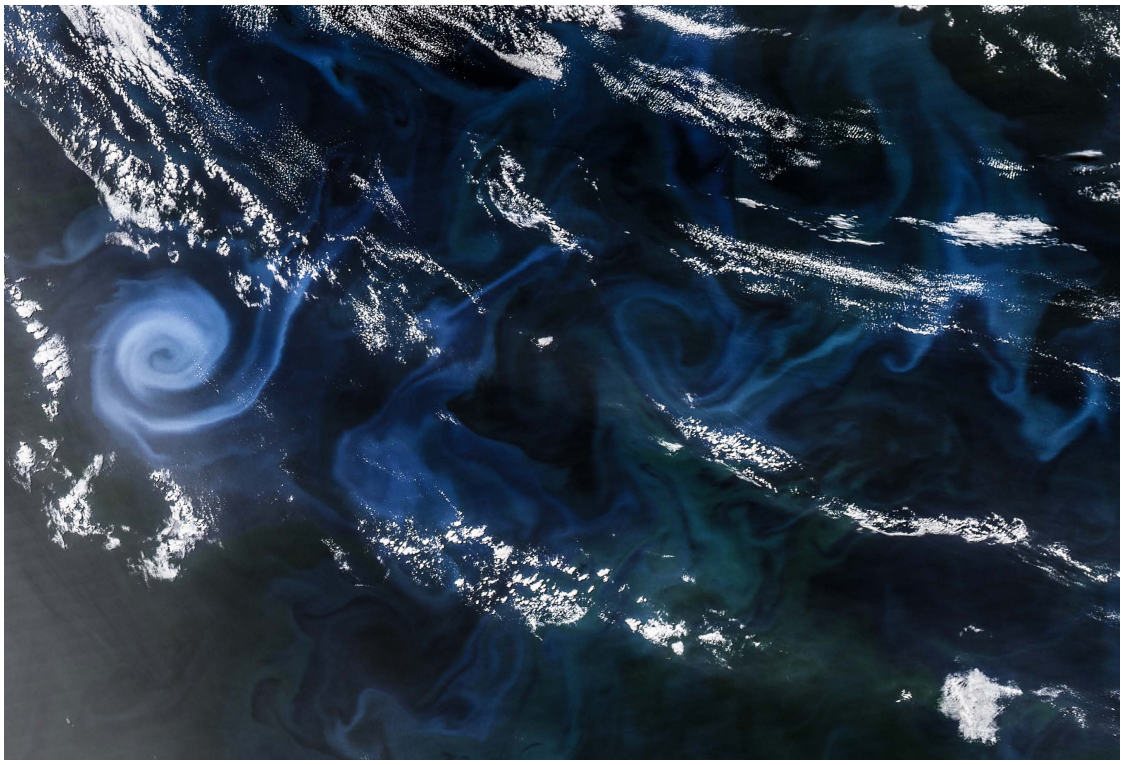

Figure 1.3: A mesoscale eddy 75-100 km in diameter and other mesoscale dynamics colored by a plankton bloom south of Australia. Granulated white patches are cloud cover. This true-color image was taken using the Aqua/Modis Satellite on December 30, 2013 (http://earthobservatory.nasa.gov/IOTD/).

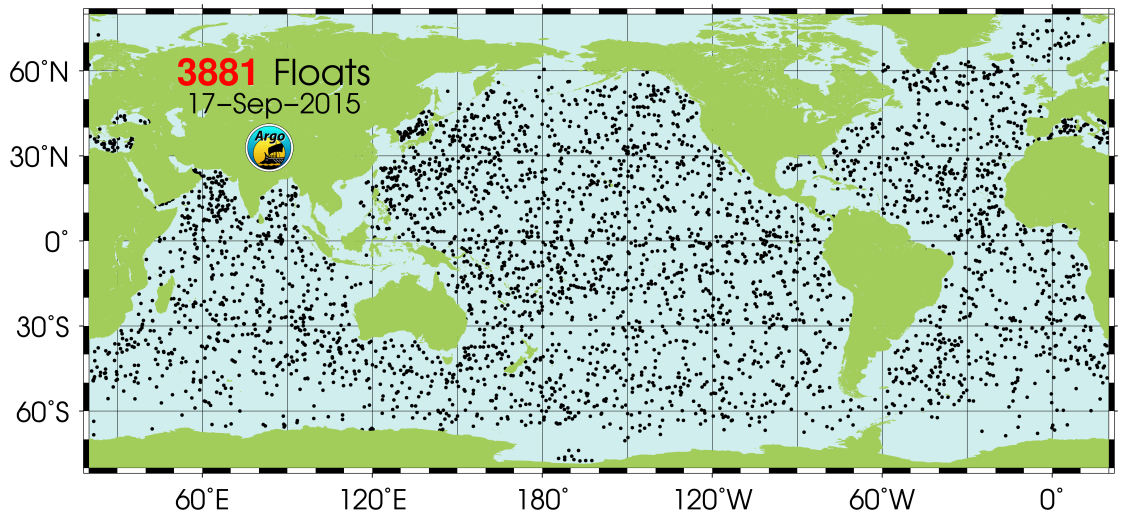

Figure 1.4: The locations of 3881 Argo profiling floats as of September 17, 2015. (http://www.argo.ucsd.edu/)

Chapter 2

Spatial and temporal variability of global ocean mixing inferred from Argo profiles

The influence of turbulent ocean mixing transcends its inherently small scales to affect large scale ocean processes including water-mass transformation, stratification maintenance, and the overturning circulation. However, the distribution of ocean mixing is not well described by sparse ship-based observations since this mixing is both spatially patchy and temporally intermittent. We use strain information from Argo float profiles in the upper 2,000 m of the ocean to generate over 400,000 estimates of the energy dissipation rate, indicative of ocean mixing. These estimates rely on numerous assumptions, and do not take the place of direct measurement methods. Temporally averaged estimates reveal clear spatial patterns in the parameterized dissipation rate and diffusivity distribution across all the oceans. They corroborate previous observations linking elevated dissipation rates to regions of rough topography. We also observe heightened estimated dissipation rates in areas of high eddy kinetic energy, as well as heightened diffusivity in high latitudes where stratification is weak. The seasonal dependence of mixing is observed in the Northwest Pacific, suggesting a wind-forced response in the upper ocean.

2.1 Introduction

Turbulent mixing closes the ocean's energy budget by dissipating the kinetic energy originating from the winds and tides. This mixing subsequently alters water composition, changing both horizontal and vertical gradients, and thereby drives the oceanic circulation on both regional and global scales. Heat, salt, and dissolved gases are distributed throughout the ocean by mixing, both by generating signature water mass properties close to the air-sea interface and altering them in the abyssal ocean. Climate models are sensitive to the spatial and temporal structure of mixing, which has implications for their treatment of the surface ocean's heat content and subsequent atmospheric feedbacks (*Harrison and Hallberg*, 2008). Ocean mixing can be measured by tracking a tracer (e.g. *Ledwell et al.* (2011)), or estimated from small fluctuations in temperature, conductivity, and shear measured by microstructure profilers (e.g. *Gregg et al.* (2003)). However, these observations have limited spatial and temporal scope due to the difficult nature of the methods employed, a substantial handicap since mixing is patchy in both space and time.

A growing number of observational studies indicate that internal waves are the major cause of turbulence in the ocean interior (*Alford and Gregg*, 2001; *Klymak et al.*, 2006). Measurements reveal that the energy dissipation rate is strongly correlated with the energy of the internal wave field via a relationship consistent with wave-wave interaction theory (*Polzin et al.*, 1995; *Gregg*, 1989). Finescale methods have been developed that either require vertical shear from velocity profiles or strain from density profiles as a measure of the internal wave energy level. Corrections are applied to account for the frequency content of the internal wave field by using the assumed constant or measured ratio between shear and strain (R_ω) along with the latitudinal dependence of the internal wave field, to form an estimate of the rate of turbulent kinetic energy dissipation ϵ (*Polzin et al.*, 1995), which can then be related to the diapycnal diffusivity κ. These finescale methods have been primarily applied to shear observations, including those from lowered acoustic Doppler current profiler (LADCP) velocity data collected on hydrographic cruises (*Kunze et al.*, 2006) with a measured R_ω correction. However, shear from

ship-based hydrography measurements has limited spatial resolution (along the ship-track), and temporal resolution (every few years at best, sparse in the winter). By applying the version of this method that utilizes strain information from density profiles (the 'strain method') with a constant R_ω to a global array of Argo float profiles, we dramatically expand the reach of this technique.

The few comparisons between strain-based dissipation rate estimates and those from microstructure data measured on turbulent dissipation scales (*Wijesekera et al.*, 1993) or Thorpe scale estimates derived from density overturns (*Thompson et al.*, 2007) agree within a factor of 2-3. Also, patterns in microstructure measurements of ϵ have been found to qualitatively match strain variance (*Mauritzen et al.*, 2002). Application of this method to global hydrographic data (*Kunze et al.*, 2006) and a selection of Argo float profiles in the Southern Ocean (*Wu et al.*, 2011) has revealed patterns consistent with ship-based observations of ocean mixing. However, the strain method relies on the underlying assumptions that all observed strain is due to internal waves, and that the wave breaking rate is governed by weakly nonlinear wave-wave interactions. Therefore agreement is not always expected everywhere. For example, this method may inaccurately estimate mixing if the observed strain is caused by intrusions, or close to breaking large-amplitude internal waves (*Klymak et al.*, 2008).

Here we calculate finescale strain variance from Argo float profiles, and use the strain method to estimate diapycnal mixing. Previous work has shown that these estimates are a good proxy for diapycnal mixing patterns (*Wijesekera et al.*, 1993; *Thompson et al.*, 2007; *Kunze et al.*, 2006; *Wu et al.*, 2011), although due to the limits of this parameterization ship-based measurements are necessary to determine accurate magnitudes at specific locations. Utilizing the strength of these estimates to show spatial and temporal patterns, we present maps of the average geographic and temporal variability, and focus on its relationship with bottom roughness, the mesoscale eddy field, and tidal energy.

2.2 Data and Methods

The Argo program is an international effort to maintain ∼3,000 freely drifting floats. Each float is equipped with conductivity, temperature, and depth (CTD) instruments that profile to 2,000 m every ten days (http://www.argo.ucsd.edu). We screened the profiles for quality, then removed the mixed layer and areas of low stratification (see Supplement).

The remaining profiles were divided into 200 m half-overlapping segments of 1-15 m resolution beginning at the bottom of each profile. The dissipation rate was estimated following *Kunze et al.* (2006), building from previous work (*Polzin et al.*, 1995; *Gregg*, 1989). Strain ξ_z was calculated from each segment,

$$\xi_z = \frac{N^2 - N^2_{fit}}{\overline{N^2}}, \tag{2.1}$$

where N^2 is the buoyancy frequency derived from the potential density profile, the over-bar denotes vertical averaging, and N^2_{fit} is a quadratic fit of the buoyancy frequency. Each strain segment was spatially Fourier transformed for the spectra S_{str}, and integrated to determine the strain variance,

$$\langle \xi_z^2 \rangle = \int_{\min(k_z)}^{\max(k_z)} S_{str}(k_z) dk_z. \tag{2.2}$$

The integration range was limited to wavenumbers corresponding to vertical wavelengths between 100 m and 40 m, while adjusting $\max(k_z)$ if necessary so that $\langle \xi_z^2 \rangle =< 0.2$ was satisfied to avoid underestimating the variance due to spectral saturation. The corresponding value for the Garrett-Munk strain variance $\langle \xi^2_{zGM} \rangle$ was determined over an identical wavenumber range. The Argo data do not specify whether a profile was derived from point measurements or depth averages; the latter underestimates strain variance. Following *Kunze et al.* (2006) ϵ estimates were calculated from single spectra, and were averaged together afterwards to avoid combining spectra of various vertical wavenumber resolution, but possibly overestimating the dissipation rate.

This strain variance was used in the finescale parameterization for the tur-

bulent kinetic energy dissipation rate (*Kunze et al.*, 2006),

$$\epsilon = \epsilon_0 \frac{\overline{N^2}}{N_0^2} \frac{\langle \xi_z^2 \rangle^2}{\langle \xi_{zGM}^2 \rangle^2} h(R_\omega) L(f, N), \tag{2.3}$$

where the constants are given by $N_0 = 5.24$ x 10^{-3} rad s^{-1}, $\epsilon_0 = 6.73$ x 10^{-10} m^2 s^{-2}. The function $L(f, N)$ provides a correction that incorporates the latitudinal dependence on the internal wave field and is defined as

$$L(f, N) = \frac{f \ \text{arccosh}(\frac{\overline{N}}{f})}{f_{30} \ \text{arccosh}(\frac{N_0}{f_{30}})}, \tag{2.4}$$

where f is the profile's Coriolis frequency, f_{30} is the Coriolis frequency at 30°, and $\overline{N}$ is the vertically averaged buoyancy frequency of the segment. The term $h(R_\omega)$ in Eq. 3.1 accounts for the frequency content of the internal wave field,

$$h(R_\omega) = \frac{1}{6\sqrt{2}} \frac{R_\omega (R_\omega + 1)}{\sqrt{R_\omega - 1}}. \tag{2.5}$$

Due to the lack of velocity and therefore shear data we assumed a constant value for the shear to strain ratio R_ω, choosing the Garrett-Munk value $R_\omega = 3$, a reasonable estimate for the upper 2,000 m (*Kunze et al.*, 2006). If this choice of R_ω is an underestimate then the term $h(R_\omega)$ is also underestimated, and the converse is also true. The dissipation rate ϵ was related to the diffusivity κ by the Osborn relation (*Osborn*, 1980)

$$\kappa = \gamma \frac{\epsilon}{\overline{N^2}}, \tag{2.6}$$

where a mixing efficiency of $\gamma = 0.2$ was used.

Smith and Sandwell ship-sounding bathymetry version 14.1 (http://topex.ucsd.edu/marine_topo/) (*Smith and Sandwell*, 1997) was used to determine bottom roughness, defined here as the variance calculated in 30 km square regions, a reasonable scale for internal tide generation (*St Laurent and Garrett*, 2002). The ship-sounding bathymetry was chosen over the version derived from satellite altimetry since it has higher spatial resolution. Integrated barotropic lunar semidiurnal (M_2) tidal energy was derived from the OSU Tidal Data Inversion (http://volkov.oce.orst.edu/tides/) following *Egbert and Ray* (2003). A climatology of near-inertial mixed layer energy

(http://ctoh.legos.obs-mip.fr/), along with the associated uncertainties, is explained in *Chaigneau et al.* (2008). The eddy kinetic energy was derived from surface drifter velocity information from the Global Drifter Program (R. Lumpkin pers. comm.). The time-mean version of this dataset can be found at http://www.aoml.noaa.gov/phod/dac/dac_meanvel.php.

Measures of uncertainty including sample size and confidence intervals, along with justification for the depth ranges used in Figures 2.1-2.11 are discussed in the Supplement.

2.3 Results

Maps showing the five year mean inferred dissipation rate and diapycnal diffusivity for segments centered between 250-500 m, 500-1,000 m and 1,000-2,000 m depths are presented in Figures 2.1 and 2.2. The dissipation rate and diffusivity maps differ since they are related by the spatially varying buoyancy frequency (Eq. 2.6). In strongly stratified regions the buoyancy frequency is large, causing lower diffusivity than at locations with a similar dissipation rate but weaker stratification. For example the Weddell Sea and Argentine Basin have similar dissipation rates, but the weaker stratification of the Weddell Sea leads to remarkably higher diffusivity. We find that our estimates of diffusivity and dissipation rate are related to: (1) bottom roughness, (2) tidal energy, (3) mixed layer near-inertial energy, (4) mesoscale eddy kinetic energy (EKE), and (5) proximity to the equator. Each of these are described in the following paragraphs.

Both the diffusivity and dissipation rate (Fig. 2.1 and 2.2) are in locally intensified over regions of rough topography (Supplementary Fig. 1). This is true even far above the actual features, consistent with the full-depth hydrography-derived estimates of *Kunze et al.* (2006), unless the background levels are high enough to mask the mixing from rough topography. The heightened mixing may be due to local interactions between geostrophic or tidal flow and topography, such as the breaking of locally produced internal tides (*Polzin et al.*, 1997), in combination with the reflection, scattering, and breaking of remotely generated internal

waves (*Johnston et al.*, 2003; *Decloedt and Luther*, 2010). Elevated dissipation rates in Figure 2.1 over rough features are consistent with previous observations above the Mid-Atlantic Ridge (*Mauritzen et al.*, 2002; *Polzin et al.*, 1997), the Mendocino fracture zone in the Northeast Pacific (*Alford*, 2010), and the Southwest Indian Ridge (*Kunze et al.*, 2006). Examples of relatively understudied areas of rough topography that have elevated mixing include the Central Indian Ridge, the Ninety East Ridge, the Chagos-Laccadive Ridge, the Sala y Gomez Fracture Zone, and the Walvis Ridge. Also notable are specific examples of reduced ϵ over smooth topographic features, including west of the Drake Passage where notably low rates of approximately 10^{-10} W kg^{-1} have been measured using tracer and microstructure methods (*Ledwell et al.*, 2011).

The averaged dissipation rate is generally (but not always) higher over rougher topography than above smoother features in a latitudinal band (Fig. 2.10a). Here we define roughness as the variance of seafloor height over 30 km scales (Supplementary Fig. 1), and 'rough topography' as locations where this parameter exceeds the global mean. Between 5° and 30° latitude (north and south), this difference may approach an order of magnitude, while both averages also increase with latitude as previously observed (*Gregg et al.*, 2003). Poleward of 30° the difference between ϵ over smooth and rough topography is often weaker, or not significant, indicating that at these latitudes other factors such as the magnitude of near-inertial energy input from wind may be more important in governing dissipation rate than bottom roughness.

Tides are one of the energy sources for the oceanic internal wave field. The barotropic tide generates internal waves, which dissipate a portion of their energy within a few hundred kilometers of their generation site (*St Laurent and Garrett*, 2002). We find a correlation between elevated M_2 tidal energy, and the median dissipation rate for a given roughness level (Fig. 2.10b). Previous observations of heightened mixing close to topographic features with strong tides are numerous, including dissipation rates exceeding 10^{-8} W kg^{-1} over the Hawaiian Ridge (*Klymak et al.*, 2006), dissipation rates reaching 2 x 10^{-6} W kg^{-1} in the Luzon Strait (*Alford et al.*, 2011), and diffusivity exceeding 5 x 10^{-4} m^2 s^{-1} in the Brazil

Basin (*Polzin et al.*, 1997). Other notable examples of elevated dissipation rates in Figure 2.1 that also exhibit high tidal kinetic energy (*Egbert and Ray*, 2003) include the North Madagascar Ridge, the Southeast Bay of Bengal, the Aleutian Ridge, the Izu-Ogasawara-Mariana Ridge, South Georgia Ridge, the ridges north and south of New Zealand, and near Tahiti. Most previous in situ observations and model-derived global maps of the tidal energy dissipation rate (*St Laurent et al.*, 2002), have highlighted mixing near rough topography in the abyssal ocean, the correlation presented here in the upper ocean is particularly striking.

Wind energy contributing to the internal wave field can originate from storms and wind bursts, adding energy to the mixed layer near the inertial frequency, and triggering internal waves that dissipate energy as they propagate downward (*Alford et al.*, 2012). Comparison of the median dissipation rate with the mixed layer near-inertial energy from *Chaigneau et al.* (2008) suggests a relationship consistent with this process. The higher the near-inertial mixed layer energy, the higher the median ϵ for a given topographic roughness (Fig. 2.10c).

The Northwest Pacific is one example of a region with both excellent Argo coverage, and notably elevated winter near-inertial mixed layer energy (*Chaigneau et al.*, 2008). Here we find a dissipation rate that is consistently higher north of 20° during the winter (January-March) compared to the summer (July-September) (Fig. 2.11a, b). The difference is especially pronounced near the Kuroshio Extension. This is consistent with the seasonal cycle of storm activity in the Pacific, resulting in internal waves and an elevated dissipation rate. Averaging our Argo-derived dissipation rate over 5° latitudinal bands between 350-450 m, 150° E and 170° W reveals a clear seasonal cycle in each band (Fig. 2.11c). This depth range is the deepest available in this region, chosen to avoid seasonal surface stratification changes missed in the screening process. The magnitude of the average dissipation rate varies, with highest values in the band closest to the equator between 25°-30°. The seasonal cycle in mixed-layer near-inertial energy is compared with the seasonal cycle in the dissipation rate between 350-450 m and 150° E-170° W shifted 50 days later (Fig. 2.11d). The average seasonal mixed layer near-inertial energy demonstrates a clear correlation with the delayed cycle in ϵ. Previous studies of

storm-generated high mode near inertial waves (*D'Asaro et al.*, 1995) indicate that this is a reasonable time lag for these waves to propagate 400 m below the ocean surface.

Areas of very high eddy kinetic energy also demonstrate a heightened dissipation rate in Figure 2.1 that is not directly attributable to mixing over rough topography, nor to wind or tidal energy. Comparing dissipation levels between 250-1,000 m and eddy kinetic energy values derived from surface drifter velocities (Lumpkin, pers. comm.) indicates a global relationship between the two (Fig. 2.10d). Specific examples include, the energetic current extensions of the Gulf Stream, the Kuroshio, East Australian Current, and Agulhas. The heightened mixing in these localized areas may be due to internal waves interacting with the high concentration of eddies (*Padman et al.*, 1990; *Kunze*, 1995), internal waves generated from topography-eddy interactions (*Nikurashin and Ferrari*, 2010; *Liang and Thurnherr*, 2012), or due to incorrectly identifying the strain associated with the eddies as internal waves. Model generated global maps of geostrophic energy input into lee waves (*Nikurashin and Ferrari*, 2011) support the eddy-topography interaction possibility for diapycnal mixing near the ocean floor, especially inthe Agulhas, the eastern equatorial Pacific, andnumerous locations along the Antarctic Circumpolar Current. The enhanced estimated dissipation rate in regions of high EKE between 250-1000 m suggests additional globally-relevant turbulence generation mechanisms.

The equatorial band also exhibits heightened dissipation rates (Fig. 2.1). As seen in the Figure 2.10a detail, the finer horizontal resolution reveals a dissipation rate maximum not at the equator, but 1-2 degrees away. This behavior is expected from the applied method's incorporation of internal waves' latitudinal dependence. However, since not all strain close to the equator is internal wave driven, these estimates maybe higher or lower than the actual equatorial dissipation rate. For example, stacked equatorial jets can create density 'steps,' within the vertical length scales that are used to estimate the dissipation rate.

2.4 Final Remarks

The diffusivity and dissipation rate estimates shown here are unprecedented in their global coverage. We see clear spatial and temporal patterns spanning a significant portion of the ocean. The method used allows us to explore global correlations between diapycnal mixing estimates and environmental variables including the tidal, wind and eddy kinetic energy fields along with topographic roughness. This broad spatial scale treatment of diapycnal mixing can assist in the development of spatially dependent mixing parameterizations in climate models, working towards a better representation of processes such as water mass transformation, and the overturning circulation. Additionally, the estimates can be used to help guide future ship-based microstructure or tracer observations, and refine climate modeling efforts to improve our understanding of the distributions and effects of ocean mixing. As the Argo program continues to deploy floats reporting at high vertical resolution (2 m), our temporal and spatial resolution of these mixing estimates will continue to improve.

2.5 Acknowledgments

Funding for this research was provided by NSF Ocean Sciences Grant No. OCE-0927650. We would like to acknowledge the International Argo Program. Thanks to Alexis Chaigneau for providing the near-inertial mixed layer energy product, Rick Lumpkin for the eddy kinetic energy product, Dean Roemmich and David Sandwell for helpful discussions, and two reviewers who improved this manuscript by offering thoughtful comments. Chapters 2, and 3 of the dissertation have been published in peer reviewed journals. This chapter is published in its entirety in Whalen, C.B., L. D. Talley and J. A. MacKinnon, 2012. Spatial and temporal variability of global ocean mixing inferred from Argo profiles. *Geophys. Res. Lett.*, 39, L18.

2.6 Appendix

2.6.1 Data and Methods

All Argo float profiles with an 'A' quality rating (all real-time quality control tests passed) between June 2006 and December 2011 were selected. The mixed layer was removed before implementing the parameterization since the mixed layer registers as a region with high strain variance. As explained in the main text the parameterization treats all strain variance as internal waves, leading to an inaccurate estimate of the diapycnal mixing. The same problem exists for other areas of low stratification near the surface (for example, mode water). The variable temperature criterion (*de Boyer Montegut et al.*, 2004) was therefore applied twice, once to remove the mixed layer, and a second time by treating the bottom of the mixed layer as the surface. Profiles with large spikes from any of the sensors were taken out of the dataset, and small salinity spikes needed to be removed from a subset of the profiles.

Each profile containing 15 m resolution or better was divided into 200 m half-overlapping segments. Segments were discarded if $\overline{N^2} < 10^{-9}$ s^{-2} or if N^2 varied by more than 6 x 10^{-4} s^{-2}, to remove sharp strain gradients not associated with internal waves. We consider the vertical resolution of the segments since this could have an affect on the calculated dissipation rates. The majority of the segments had either 2 m or 10 m resolution, with similar mean ϵ (the mean 10 m resolution estimate above 500 m was only 10% larger), while the standard deviation of dissipation rate for 2 m data was 40% larger.

The sensitivity of the dissipation rate parameterization to our choice of parameters is considered in Figure 2.6. Two parameter choices are considered: the choice of the length of the profile segments used for each dissipation estimate, and the limits of spectral integration. The comparisons show only a slight dependence on the parameter choices; the mean logarithm of the dissipation differing by less than 0.1 W kg^{-1} for each of the pairs. The largest discrepancy occurs when comparing segment lengths of 200 m and 240 m for segments centered between

250-500 m (Fig. 2.6a). This is because changing the segment length changes the mean depth of the segments being used for the average. As Figure 2.6a shows, averages that become deeper when segment length is increased from 200 m to 240 m generally have a lower dissipation rate, and shallower averages have higher dissipation rates. The deeper averages between 500-1000 m in Figure 2.6c exhibit very little dependence on the segment length.

2.6.2 Figures 1 and 2 Uncertainty

Figures 1 and 2 in the main text show the average dissipation rate or diapycnal diffusivity for all segments within the specified depth range and 1.5° bin where at least three estimates exist. The uncertainty of these estimates is affected by the number of samples contributing to each average as shown in Figure 2.7. Since the sample size of some averages is very small (three samples), we can't present a meaningful bootstrapped confidence interval for each average. Instead, Figure 2.8 shows ninety percent bootstrapped confidence intervals for all averages in Figure 1 that contain at least ten estimates. Figure 2 has confidence intervals that are qualitatively similar.

The depth ranges in Figures 1 and 2 were chosen carefully since the maximum depth of the high vertical resolution data of a profile varies dramatically depending on the satellite communication system limitations and the choices of the group deploying the particular float. Due to the fact that floats in one area are more likely to be deployed by the same group, this translates into a spatial dependence on the maximum usable profile depth. Since the dissipation rate depends on depth in the thermocline (Fig. 2.9b), and because diffusivity has a slight dependence on depth between 250-2,000 m (Fig. 2.9a), this bias has the potential to lead to a spatial bias in Figures 1 and 2. For example, as seen in Figure 2.9c, in the western equatorial Indian Ocean and the Kuroshio region the average depth of the dissipation rate estimates between 250-500 m is shallower than 375 m, the center of this depth range. In this case the affect is mitigated by the narrow depth range chosen for averaging (250-500 m). Depth ranges of 250-500 m, 500-1,000 m, and 1,000-2,000 m were chosen to provide a small depth range of 250 m in

the thermocline (where both the dissipation rate varies strongly with depth, and the vertical resolution of the profiles spatially vary drastically), and larger depth ranges are chosen for deeper regions (where the dissipation rate and diffusivity is fairly constant and the average depth of an estimate is fairly consistent).

2.6.3 Figure 3 Uncertainty

Figure 3 (b-d) shows the median dissipation rate for each bin containing over 15 location estimates defined by a range of roughness and another environmental variable. The estimates from segments centered between 250-1,000 m were used rather than 250-2,000 m in order to limit the comparison range to where similar dynamics may be important. Slight alterations to the vertical range do not change the results dramatically. Here we show the number of estimates in each bin (Fig. 2.10a-c) and the ninety percent bootstrapped confidence intervals surrounding each estimate (Fig. 2.10d-f) derived using 1,000 samples. In Figures 3a the confidence intervals bars were calculated from 1,000 bootstrapped samples with a mean sample size of approximately 2,200.

2.6.4 Figure 4 Uncertainty

Figure 4 (a,b) shows the mean dissipation rates for July-September and January-March in the Northwestern Pacific. Unlike Figures 1 and 2 there is no minimum to the of number estimates contributing to each plotted average; however a pattern is still discernible since only select month ranges are shown, and much of the variability is seasonal. Figures 2.11a and 2.11b show the number of estimates contributing to each average. The depth range of 350-450 m was chosen to take advantage of the deepest available data in this region. As in the case of Figures 1 and 2, the sample size is sometimes too small to calculate confidence intervals. In Figure 4c the bootstrapped confidence intervals were derived from 1,000 samples with a mean sample size of approximately 70.

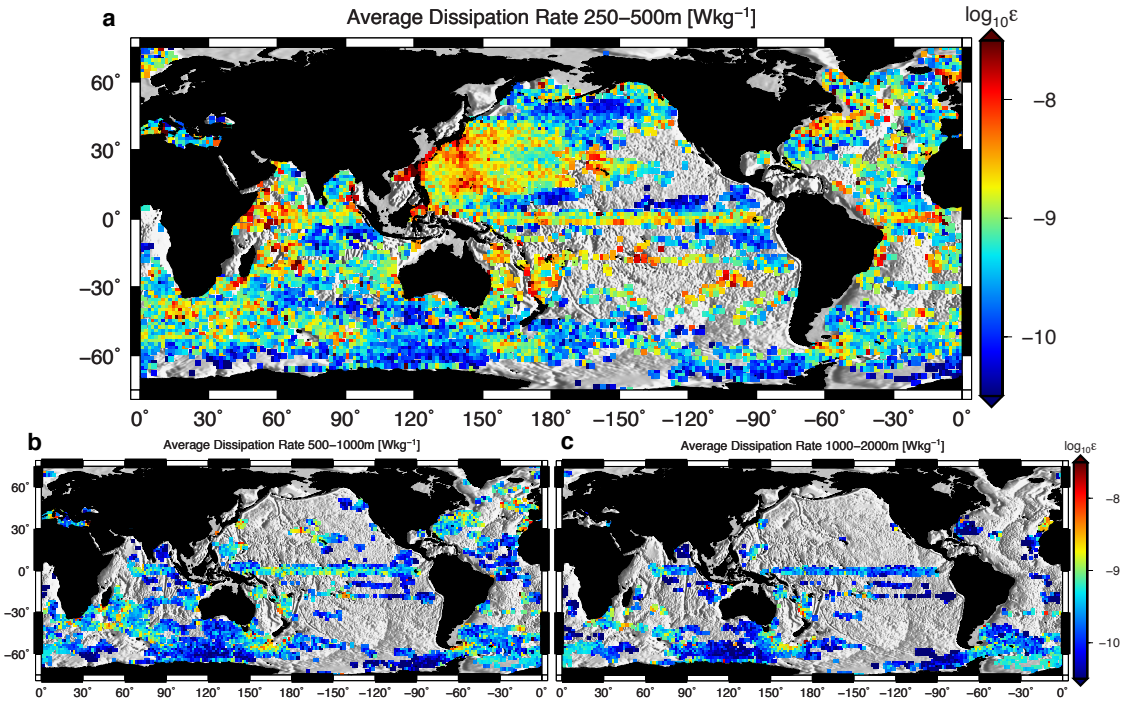

Figure 2.1: Dissipation rate ϵ (W kg^{-1}) estimated from over five years (2006-2011) of Argo data. Estimates from high vertical resolution data centered between (a) 250-500 m, (b) 500-1,000 m, and (c) 1,000-2,000 m are averaged over 1.5° square bins and plotted if they contain more than three dissipation rate estimates. The underlying bathymetry is from the Smith and Sandwell dataset (*Smith and Sandwell*, 1997) version 14.1.

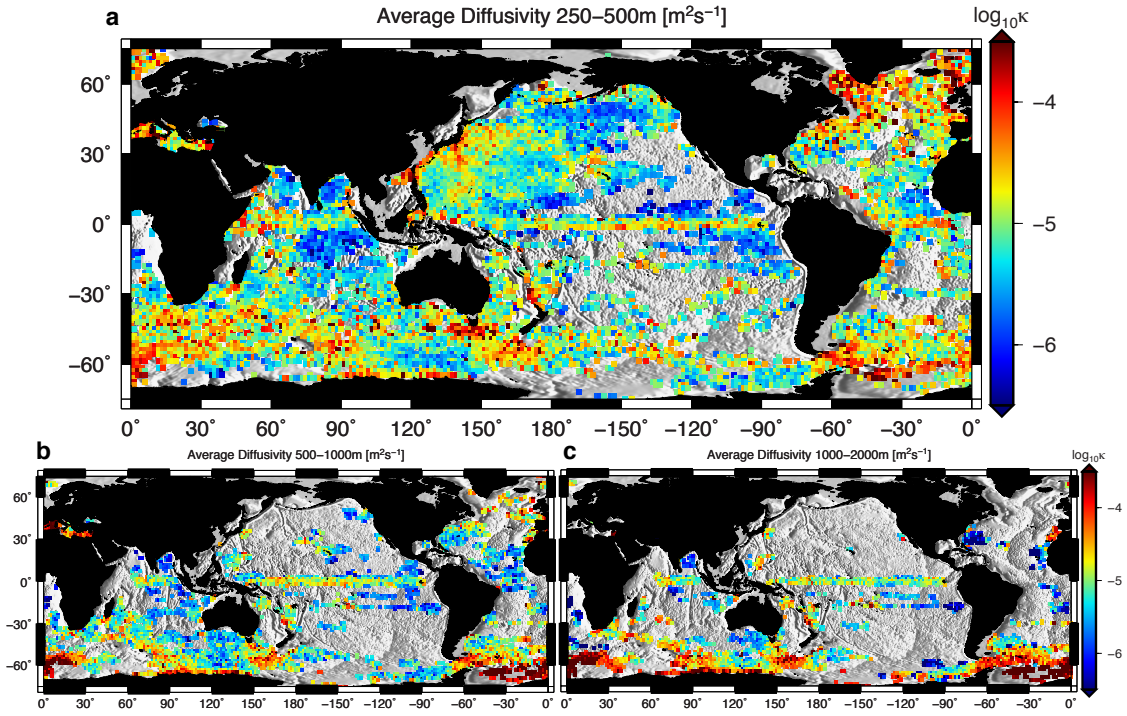

Figure 2.2: Averaged diffusivity κ ($\mathrm{m^2 s^{-1}}$). Otherwise identical to Fig. 1.

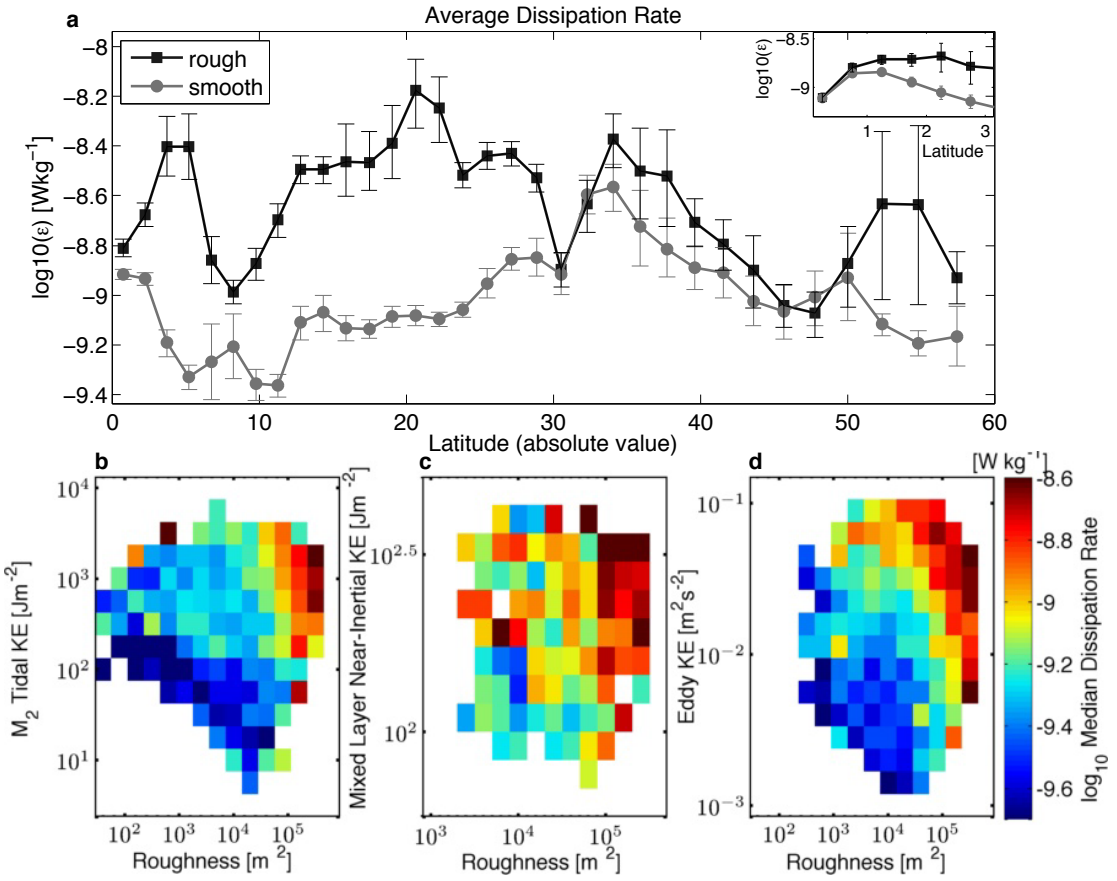

Figure 2.3: Dissipation related to roughness, barotropic lunar semidiurnal (M_2) tidal energy, mixed-layer near-inertial energy, and eddy kinetic energy. (a) Global mean dissipation rate for 3° half-overlapping latitudinal bands in the depth range 250-1,000 m over rough (variance greater than global mean) and smooth topography with 90% bootstrapped confidence intervals. Inset shows a finer resolution equatorial region for 1° half-overlapping bands. (b)-(d) Median dissipation rate as a function of roughness and (b) M_2 tidal kinetic energy (*Egbert and Ray*, 2003); (c) mixed layer near-inertial kinetic energy from *Chaigneau et al.* (2008); and (d) eddy kinetic energy from the Global Drifter Program (R. Lumpkin, pers. comm.). Plotted averages include estimates between 250-1,000 m in depth for bins containing >15 estimates.

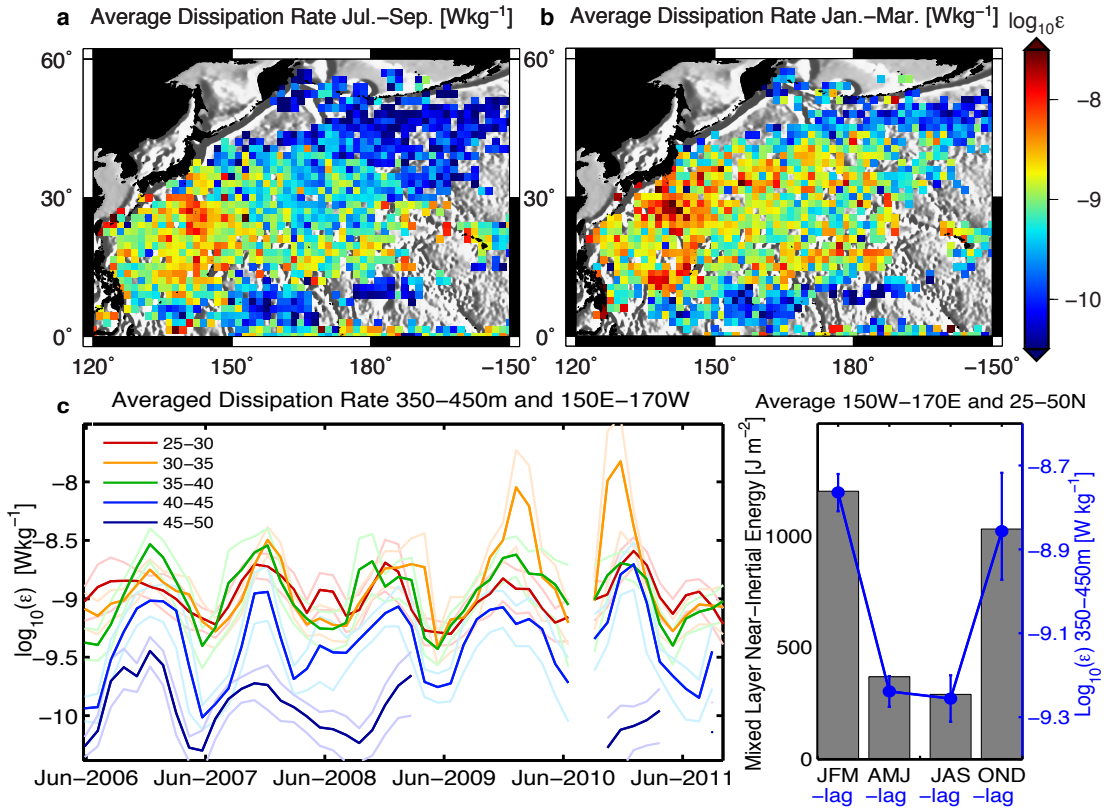

Figure 2.4: Seasonal cycle of the dissipation rate for the Northwest Pacific. (a, b) Spatial comparison of the winter and summer dissipation rate patterns between 350-450 m; (c) time series average of dissipation rate between 150° E and 170° W, over 5° bands of latitude, between depths of 350-450 m, with lightly colored confidence intervals; and (d) seasonally averaged mixed layer near-inertial energy in the region 150° E-170° W, 25°-50° N (gray bars) and the average dissipation rate in the same region between 350-450 m, seasonally averaged with a 50-day lag (blue line). The 90% bootstrapped confidence intervals are shown in (c) and (d).

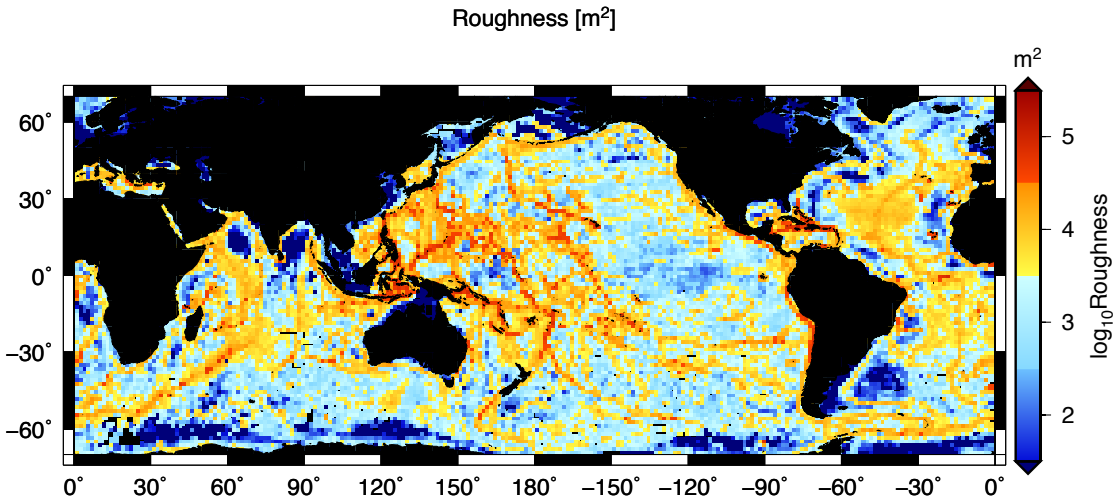

Figure 2.5: Global roughness. Ship soundings from the Smith and Sandwell bathymetric dataset (http://topex.ucsd.edu/marine_topo/) were used to estimate roughness by calculating the variance in elevation within 30 km x 30 km squares.

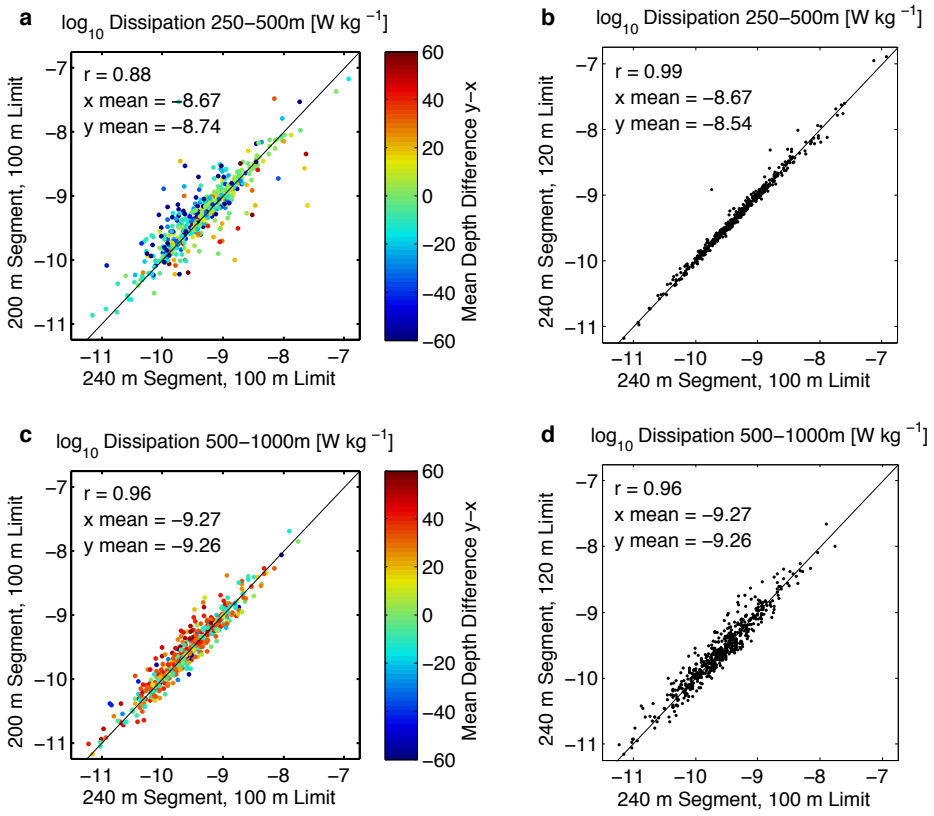

Figure 2.6: Parameter choice sensitivity. Compares the averages of segments centered between (a,b) 250-500 m or (c,d) 500-1000 m of estimates calculated from all the available data from the Atlantic in 2011 within 1.5 degree bins. Two parameters are tested: the length of the profile segment used to generate the spectrum necessary for this parameterization, and the wavelength limit of integrating of that spectrum. The x-axis always shows average dissipation values for a 240 m segment, with a 100 m limit. (a,c) This is compared with a 200 m segment and a 100 m limit, the parameters used in our analysis, or (b,d) a 240 m segment and a 120 m limit. The colors in (a) and (c) correspond to the change in the mean depth of the estimates between the 200 m segment analysis, and the 240 m segment analysis. This change is zero for (b) and (d).

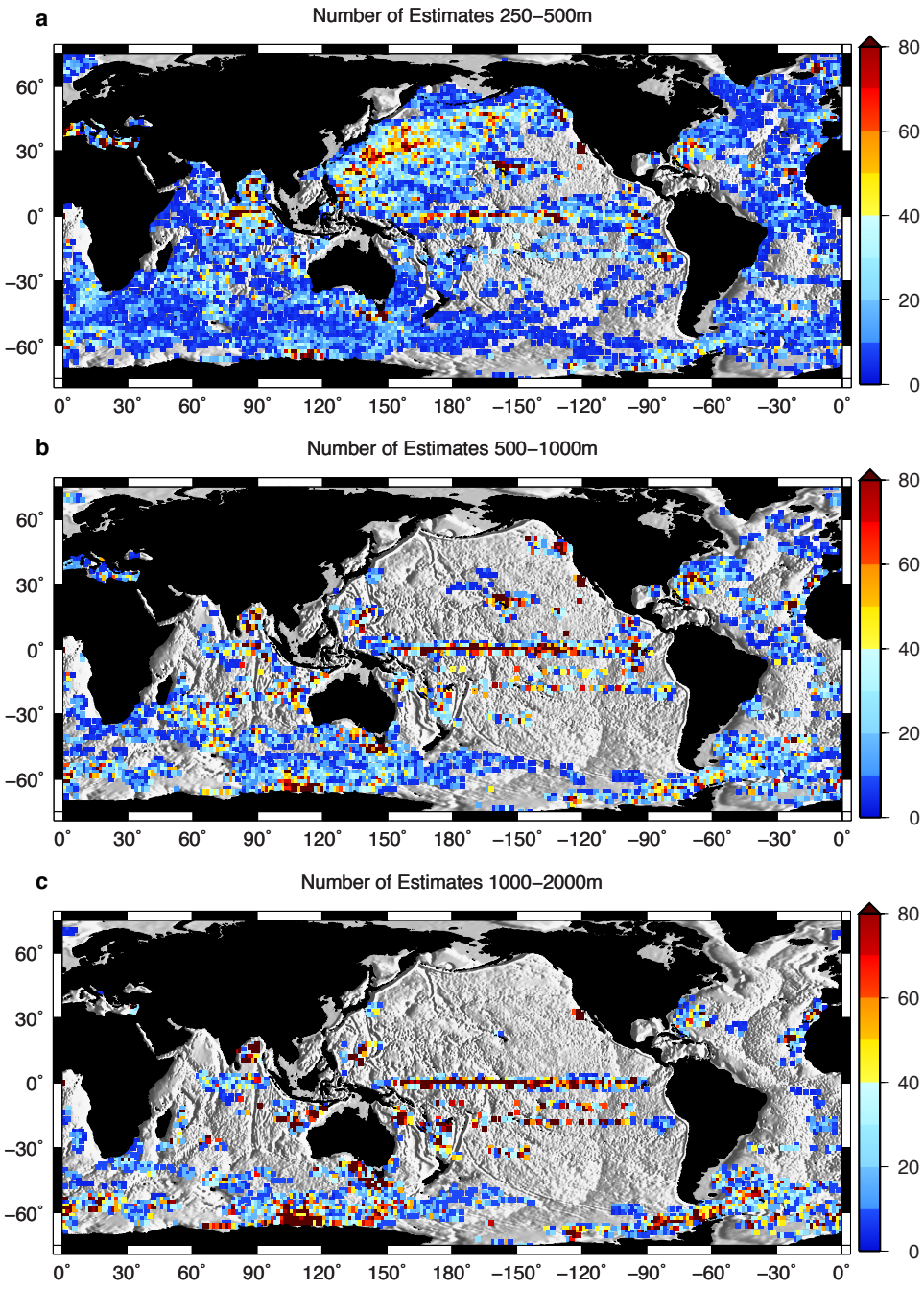

Figure 2.7: Number of dissipation rate or diffusivity estimates contributing to each datapoint in Figures 1 and 2 in the main text. Minimum number of estimates in each average is three.

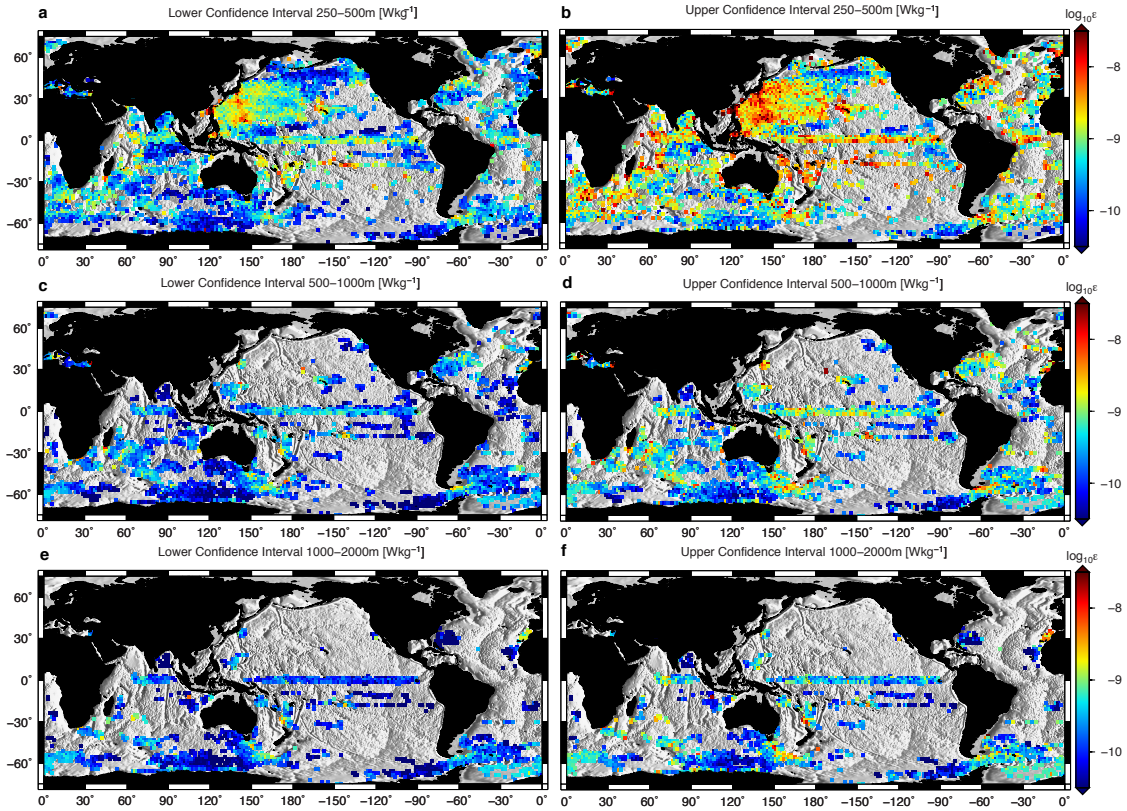

Figure 2.8: Ninety percent confidence intervals for Figure 1. Intervals were found for all averages containing at least 10 estimates using the bootstrap method for 1,000 samples. The left column are the lower confidence intervals and the right column shows the upper confidence intervals. The intervals correspond to the depth ranges of (a,b) 250-500 m, (c,d) 500-1000 m, and (e,f) 1,000-2,000 m.

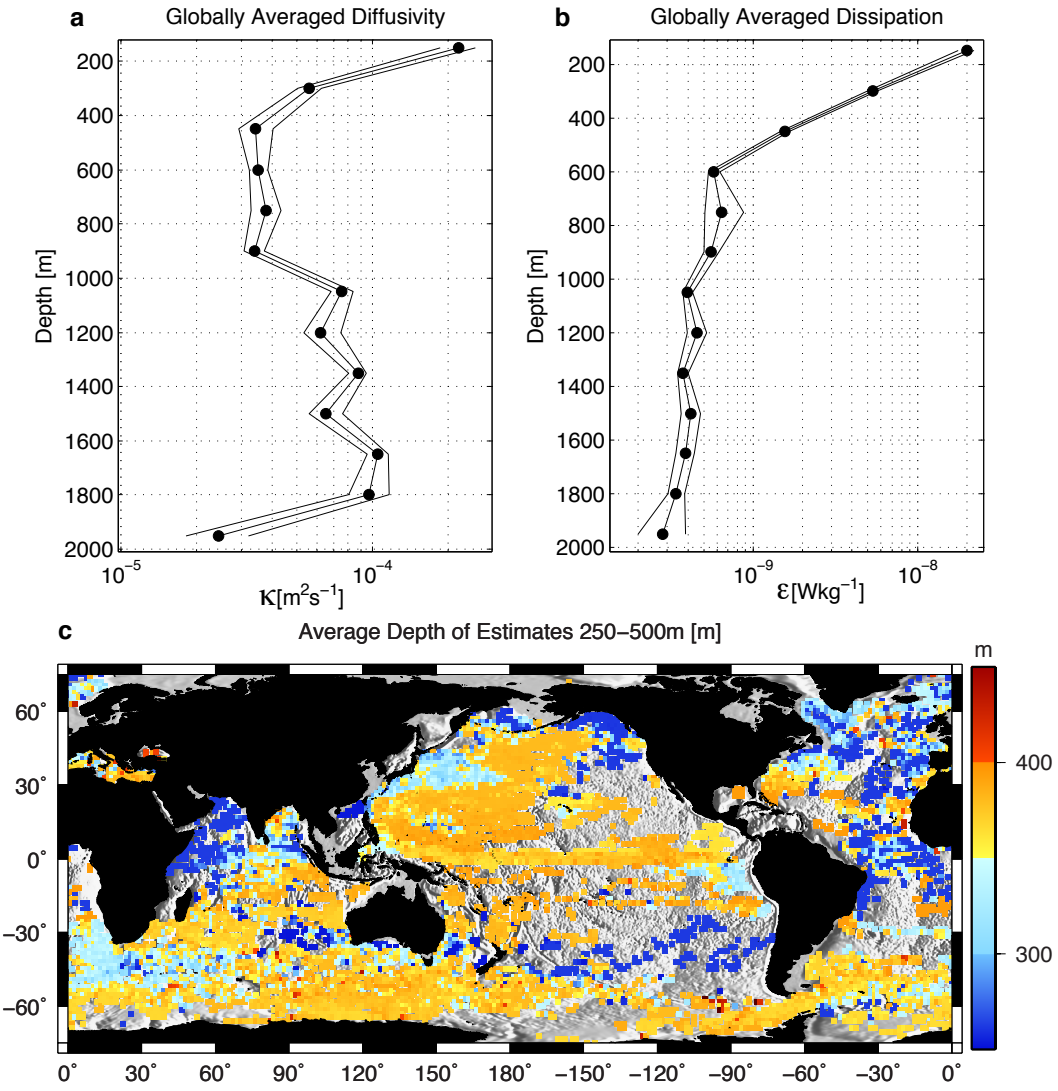

Figure 2.9: Depth dependence of estimates. (a,b) Globally averaged diffusivity and dissipation rate vs. depth averaged in 150 m bins containing at least 25 estimates with 90% bootstapped confidence intervals. (c) The average depth of the dissipation rate and diffusivity estimates in the 250-500 m plots in Figures 1 and 2.

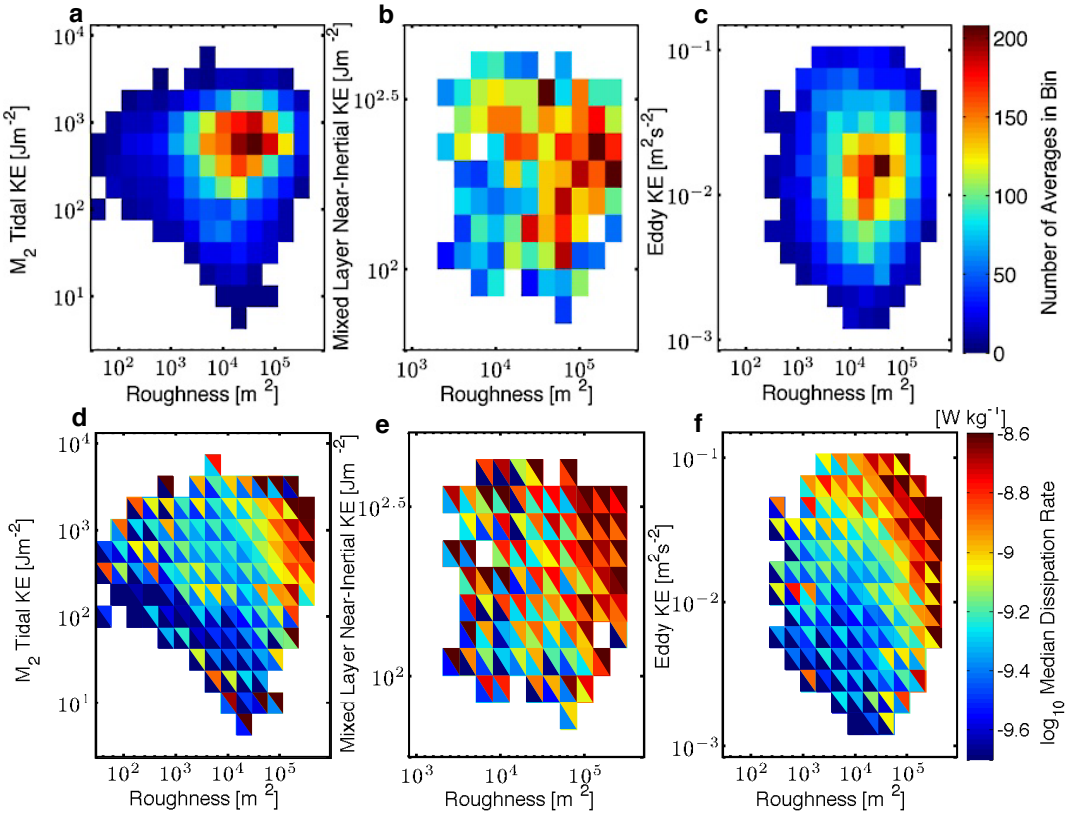

Figure 2.10: Number of estimates and confidence intervals. (a-c) Number of estimates going into each average for Figure 3a-c. (d-f) The 90 percent bootstrapped confidence intervals calculated for Figure 3a-c where the triangles in each square correspond to the upper and lower confidence intervals.

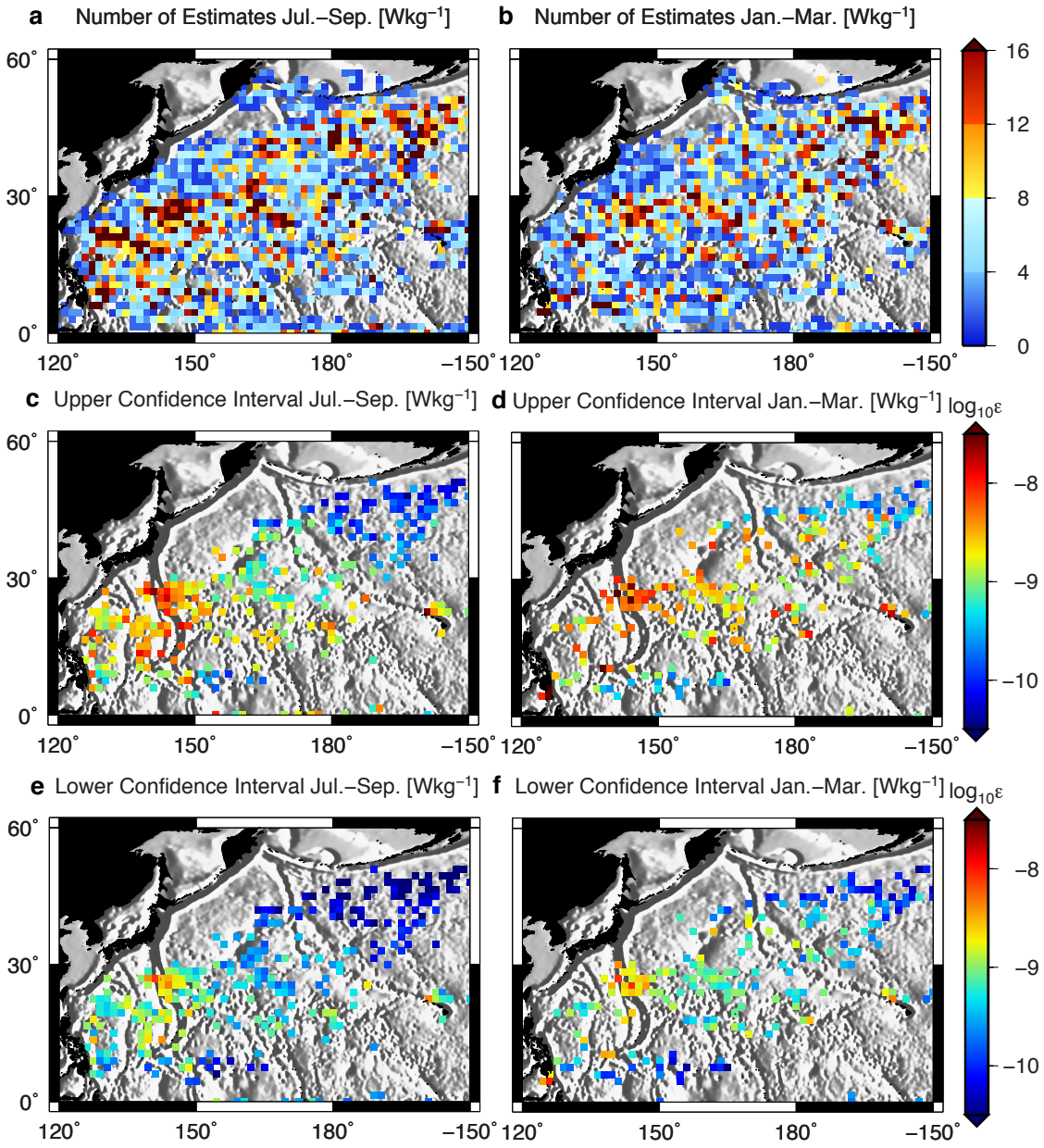

Figure 2.11: Number of location estimates and confidence intervals. (a,b) Number of location estimates going into each average for Figure 4a, and 4b. (c,d) Upper and (e,f) lower ninety percent bootstrapped confidence intervals for Figure 4a and 4b with 1,000 samples. Only averages with more than 15 location estimates were used to calculate the upper and lower confidence intervals.

Chapter 3

Estimating the Mean Diapycnal Mixing Using a Finescale Strain Parameterization

Finescale methods are currently being applied to estimate the mean turbulent dissipation rate and diffusivity on regional and global scales. We evaluate finescale estimates derived from isopycnal strain by comparing them with average microstructure profiles from six diverse environments including the equator, above ridges, near seamounts, and in strong currents. The finescale strain estimates are derived from at least ten nearby Argo profiles (generally <60 km distant) with no temporal restrictions including measurements separated by seasons or decades. The absence of temporal limits is reasonable in these cases since we find the dissipation rate is steady over seasonal timescales at the latitudes we are considering (0°-30° and 40°-50°). In contrast, a seasonal cycle of a factor of 2-5 in the upper 1000 m is found under storm tracks (30°-40°) in both hemispheres. Agreement between the mean dissipation rate calculated using Argo profiles and mean from microstructure profiles is within a factor of 2-3 for 96% of the comparisons. This both is congruous with the physical scaling underlying the finescale parameterization and indicates that the method is effective for estimating the regional mean dissipation rates in the open ocean.

3.1 Introduction

Turbulent mixing is integral to many regional and global-scale processes throughout the ocean, ranging from the ocean's overturning circulation to the distribution of passive tracers. However, measurements resolving turbulence have been difficult to achieve since they rely on specialized ship-based instruments, and thus long temporal and large spatial scale patterns are hard to discern. Instruments capable of very high resolution temperature measurements are starting to be deployed on long timescales (*Moum et al.*, 2009), but these devices are not yet in wide use.

To fill this gap, finescale parameterizations are being applied to estimate the turbulent kinetic energy dissipation rate and diapycnal diffusivity from a variety of more common instruments such as CTDs, ADCPs, and Argo profiles (e.g. *Gregg*, 1989; *Polzin et al.*, 1995; *Kunze et al.*, 2006; *Huussen et al.*, 2012; *Wu et al.*, 2011; *Whalen et al.*, 2012). Strain and shear based finescale parameterizations aim to infer the centimeter-scale turbulent energy dissipation rate from what can be measured with relative ease with 2-15 m resolution using the scale-bridging physics of internal waves. These parameterizations rely on two major assumptions:

(A) The observed variance in shear and/or strain on 10-100 m scales is caused mainly by internal waves.

(B) The energy dissipation rate is primarily due to nonlinear interactions between internal waves that transfer energy from the finescale towards smaller-scale waves that subsequently break into turbulence.

Internal waves are associated with shear and strain variance observed on vertical scales of 10-100 m. Realizing that much of the finescale variance is caused by internal waves (Assumption A), and that energy transfers between these waves in the open ocean can be described using nonlinear interaction theory (Assumption B), has led previous authors to use a wave action approach (*Henyey et al.*, 1986; *Muller et al.*, 1986; *Henyey and Pomphrey*, 1983). This allows for an expression of the down-spectrum energy cascade in terms of the shear and/or strain spectra

as explained in *Polzin et al.* (2014). Assuming that this internal wave energy cascade sets the energy dissipation rate (Assumption B) allows for calculation of the dissipation rate from the shear or strain spectra.

A key point is that finescale estimates of the dissipation rate are measuring distinctly different quantities than microstructure measurements. Both the length and time scales are larger for the finescale estimates than for the microstructure. It may be helpful to think of the microstructure profiles as a snapshot of the turbulence at an instant, while the finestructure profiles are estimates of the average dissipation rate expected over several wave periods. Therefore, comparing equivalent quantities requires averaging multiple microstructure profiles in time.

A set of parameterizations using finescale *shear* profiles has been tested in a variety of contexts, showing good agreement with microstructure in open-ocean conditions (*Gregg*, 1989; *Polzin et al.*, 1995; *Winkel et al.*, 2002; *Polzin et al.*, 2014). Implementation of shear parameterizations have revealed reasonable patterns of diapycnal mixing (*Polzin et al.*, 1997; *Kunze et al.*, 2006; *Huussen et al.*, 2012). The shear-based parameterization is known not to be effective in regions where the underlying assumptions behind the parameterization do not apply (*Polzin et al.*, 2014), such as on continental shelves (*MacKinnon and Gregg*, 2003), and in strong geostrophic flow over rough topography (*Waterman et al.*, 2014). Studies have also uncovered discrepancies in the presence of very large overturning internal waves (*Klymak et al.*, 2008), and in submarine canyons (*Kunze et al.*, 2002), however *Polzin et al.* (2014) suggests that in these cases the disparity may be due to parameterization implementation choices rather than a violation of the underlying assumptions.

In contrast, the finescale *strain*-based version of this parameterization has only been tested to a limited extent. Observational work has uncovered a correlation between the finescale strain variance and the dissipation rate (*Desaubies and Gregg*, 1981; *Gregg and Kunze*, 1991; *Wijesekera et al.*, 1993; *Padman et al.*, 1990; *Mauritzen et al.*, 2002), and it has been subsequently applied to yield reasonable large-scale patterns of diapycnal diffusivity (*Kunze et al.*, 2006; *Wu et al.*, 2011; *Whalen et al.*, 2012). Individual profiles over seamounts have been compared in

Hibiya et al. (2012). To the best of our knowledge, the only regional evaluations of the strain parameterization were conducted by *Frants et al.* (2013) and *Waterman et al.* (2014) using data from the Southern Ocean. The *Frants et al.* (2013) study found that applying the parameterization to CTD profiles characterizes the regional patterns better than using Thorpe-scale overturns (*Thorpe*, 1977) since the Thorpe-scale method only includes overturns large enough to be fully resolved by the CTD. These estimates usually agreed with the microstructure within a factor of 2-3. *Waterman et al.* (2014) found that individual microstructure profiles agreed with finestructure within a factor of 2 more than 1500 m from the bottom, but discrepancies in a subset of the profiles caused the average finestructure to overestimate the microstructure within 1500 m of the seafloor. Possible explanations for this discrepancy are described in *Waterman et al.* (2014).

One motivation for an accurate parameterization is to assist estimates of the long-term mean dissipation rate and diffusivity both regionally and globally. This has the potential to aid our understanding of global processes such as the meridional overturning circulation, along with the heat and energy balance in the ocean. These estimates are hard to make, but have been completed on a global scale using a catalog of microstructure measurements (*Waterhouse et al.*, 2014), and in the Indian Ocean using a finescale parameterization (*Huussen et al.*, 2012). The difficulty arises because in addition to the spatial variability of diapycnal mixing (e.g. *Polzin et al.*, 1997; *Kunze et al.*, 2006), there may also be temporal fluctuations on long enough scales to affect both microstructure and finescale estimates of the mean.

Origins of the temporal variability of diapycnal mixing on time scales longer than days include fluctuations of the two major internal wave energy sources, the winds and tides, as well as isolated events. Wind gusts in storms can perturb the mixed layer near the inertial frequency (*D'Asaro et al.*, 1995), leading to downward-propagating near-inertial waves (e.g. *Alford et al.*, 2012), and a seasonal cycle of these waves that tracks the seasonal cycle of storm activity (*Alford and Whitmont*, 2007; *Silverthorne and Toole*, 2009; *Whalen et al.*, 2012). The spring-neap tidal cycle modulates the strength of flow over topography and subsequent internal waves

that are generated, leading to a cycle in the dissipation rate (e.g. *Klymak et al.*, 2006). Geostrophic flow, interacting with topography and generating lee-waves (*Bell*, 1975), can also be a source of episodic increases in the dissipation rate (*Sheen et al.*, 2014). Sampling on scales much shorter than a month may misrepresent the mean close to generation sites of the internal tide with strong spring-neap cycles, and less than a year could be problematic for areas with strong seasonal cycles. This is particularly true due to the log-normal nature of the mixing distribution; missing the large rare mixing events matters significantly (*Gregg et al.*, 1993).

The following describes the first comparison between microstructure estimates and strain-based finescale estimates of the dissipation rate conducted for a wide variety of bathymetric features and forcing environments. This is accomplished by matching an updated global dataset of Argo float finestructure profiles previously discussed in *Whalen et al.* (2012) with nearby microstructure profiles. No temporal restrictions are utilized, implying that the profiles can be from different seasons or even decades. This is essentially assuming that both the microstructure (duration of <1 month) and the finestructure (year-round) are both estimates of the mean mixing at a particular location. The assumption is reasonable at the microstructure project locations since we find only a small (less than a factor of 2) or non-detectable seasonal cycle. When at least ten estimates are averaged together we find a good agreement between the two methods: 81% of the dissipation rate comparisons agree within a factor of 2, and 96% agree within a factor of 3.

3.2 Microstructure Data

Instruments that measure microstructure typically include fast-sampling shear, temperature and conductivity probes along with a CTD sampling at the standard rate. The microstructure measurements are used to calculate the dissipation rate (ϵ, W/kg) and diffusivity (K, m^2/s) via the relation $K = \Gamma\epsilon/\overline{N^2}$, where here $\overline{N^2}$ is the average adiabatically leveled buoyancy frequency (*Bray and Fofonoff*, 1981), and a constant $\Gamma = 0.2$ is assumed.

These microstructure projects are a subset of the open-ocean dataset used in

Waterhouse et al (2014). Here we additionally require that the profiles reach deeper than 300 m to enable a meaningful comparison with the finestructure estimates as explained in Section 3.5. Projects are also only selected if they are near at least ten Argo profiles and sample one particular area as opposed to a transect. The locations of every microstructure project are shown in Figure 3.1a.

The projects include two from the Atlantic Ocean: the North Atlantic Tracer Release Experiment (NATRE) above an abyssal plane (*Toole et al.*, 1994; *Polzin and Ferrari*, 2004), and a dataset from 1997 including the Mid-Atlantic Ridge called the Brazil Basin Tracer Release Experiment (BBTRE97) (*Ledwell et al.*, 2000; *Polzin et al.*, 1997; *St Laurent et al.*, 2001). The projects in the Pacific Ocean are the Hawaii Ocean Mixing Experiment (HOME) which examines the Hawaiian Ridge as a site for the generation of internal waves (*Lee et al.*, 2006; *Rudnick et al.*, 2003; *Klymak et al.*, 2006), LArval Dispersal on the Deep East pacific Rise (LADDER) (*Thurnherr and St Laurent*, 2011). A total of 25 equatorial microstructure profiles collected from April 25th through May 3rd, 2012 using a Rockland VMP-600 as part of the MIXing in the Equatorial Thermocline project were included (MIXET, unpublished, PI G. S. Carter). The final project is the Southern Ocean Finestructure (SOFine) program in the Indian Ocean which covers a section of the Antarctic Circumpolar Current (ACC) in the Kerguelen Plateau region (*Waterman et al.*, 2013, 2014).

Specific microstructure profiles from each project were selected according to the criteria described in Section 3.5. As shown in Figure 3.1a, these locations cover a variety of latitudes and bottom topographies, including rough and smooth topography as defined by bottom height variance calculated over 30 km squares derived from the *Smith and Sandwell* (1997) 14.1 ship-track bottom bathymetry dataset. *Waterhouse et al.* (2014) demonstrate that these projects span the global range of power input levels into internal waves from the winds and tides, the presumed sources of turbulence. Figure 3.1b shows the average power input into internal waves for each project from the winds and tides within half a degree of a microstructure profile alongside the global mean calculated from a slab model (*Alford et al.*, 2012; *Simmons and Alford*, 2012). The details of the model configu-

rations and key caveats are described in *Waterhouse et al.* (2014). In this selection of datasets there is a bias towards areas of low power input; only HOME, SOFine, and BBTRE97 exceed the global average tidal input, and only SOFine exceeds the average global wind input.

3.3 Argo Data

Every ten days, a typical Argo float collects temperature, salinity, and pressure data between 2000 m and the surface before uploading the data via satellite for free access (http://www.argo.net/). Currently the float array consists of over 3500 floats scattered across every ocean. Their profiles have a variety of vertical resolutions due to communication constraints. For example, some profiles change from high resolution (5 m) to low resolution (40 m) with increasing depth. There are a growing number of Argo floats with Iridium communication which permit high vertical resolution (typically 2 m) throughout their 2000 m profile.

All Argo profiles with the program-designated quality rating of 'A' (passed all real-time quality control tests) between January 2006 and March 2014 are selected for this analysis. They are additionally despiked and quality controlled to remove incomplete data and unrealistic values. After removal of the mixed layer and mode water (Section 3.4), the profiles are cut into 200 m half-overlapping segments with constant resolution starting at the bottom of each profile. A length of 200 m was chosen to maximize the total number of usable segments in profiles that have variable resolution. Changing the segment length slightly (for example to 240 m) on average has a negligible effect on the resulting estimates (*Whalen et al.*, 2012).

The vertical gradient of both salinity and temperature is sometimes very small (for example in the Weddell Sea). In this case the actual finescale variance in salinity cannot be resolved, and the salinity profile appears to have steps as it shifts from one resolved value to another. These artifacts were removed by only selecting segments where both the maximum temperature range was greater than 0.2° C and the maximum salinity range was greater than 0.02 psu.

In the upper 250 m the assumptions underlying the finescale parameterizations do not always apply (*Kunze et al.*, 2006; *Polzin et al.*, 2014). This is because near the surface of the ocean non-internal wave-driven variations in the buoyancy frequency, including mode water and surface processes, are particularly prevalent. The strain-like features that they produce are not internal waves, and therefore not subject to the energy cascade that we assume in the finescale parameterization. We will only consider estimates centered below 250 m to mitigate this issue.

3.4 Finestructure Methods

The strain-based finescale estimates from Argo floats were calculated following *Kunze et al.* (2006), stemming from *Polzin et al.* (1995) and *Gregg and Kunze* (1991), in a nearly identical approach to *Whalen et al.* (2012). The dissipation rate is expressed in the strain version of the finescale parameterization in practical form as

$$\epsilon = \epsilon_0 \frac{\overline{N^2}}{N_0^2} \frac{\langle \xi_z^2 \rangle^2}{\langle \xi_{zGM}^2 \rangle^2} h(R_\omega) L(f, N), \tag{3.1}$$

where $\langle \xi_z^2 \rangle$ and $\langle \xi_{zGM}^2 \rangle$ are the observed and Garrett-Munk (GM; *Cairns and Williams*, 1976) strain variances respectively, $\overline{N^2}$ is the segment-averaged buoyancy frequency, $h(R_\omega)$ describes the dependence on the the ratio between shear and strain R_ω which we set to 3, and $L(f, N)$ is a latitudinal correction (*Polzin et al.*, 1995; *Gregg et al.*, 2003). The constants are N_0 = 5.24 x 10^{-3} rad s^{-1}, and ϵ_0 = 6.73 x 10^{-10} m^2 s^{-2}. This produces a single estimate of the dissipation rate for each 200-m segment. All the variable terms in Equation 3.1, including $\overline{N^2}$, $L(f, N)$, and $\frac{\langle \xi_z^2 \rangle^2}{\langle \xi_{zGM}^2 \rangle^2}$ are important in the parameterization. Each of these terms varies two to five orders of magnitude between 250-2000 m in the finescale estimates considered here.

The backbone of Equation 3.1 is the buoyancy frequency, appearing in multiple terms including the strain,

$$\xi_z = \frac{N^2 - N_{fit}^2}{\overline{N^2}}, \tag{3.2}$$

where N^2 is the buoyancy frequency, and N_{fit}^2 is a quadratic fit (*Polzin et al.*,

1995; *Huussen et al.*, 2012). The $\overline{N^2}$ in the denominator is equivalent to a mean of N^2_{fit}. If the segment-scale and smaller variations in the buoyancy frequency are dominated by processes other than internal waves in violation of Assumption A (see Section 4.1), the dissipation rate will be incorrectly estimated (*Polzin et al.*, 2014).

Segments partially spanning the mixed layer or mode water often have a high strain variance due to large gradients between high and low stratification water, which are not predominantly caused to the presence of internal waves. Here we remove the mixed layer using the variable temperature criterion (*de Boyer Montegut et al.*, 2004) where the bottom of the mixed layer is defined as the depth where the increase in density from 10 m is equivalent to a decrease in temperature of 0.2° using local conditions. The mode water is removed by applying the criterion a second time, using the bottom of the mixed layer analogously to the surface of the ocean. This method only removes the most prominent mode-water and non-internal wave buoyancy frequency structure. Inclusion of these subtle mode water profiles may lead to over-estimation of diapycnal mixing in these areas.

Another violation of Assumption A, when the observed strain is not due to internal waves, occurs when large variations in the buoyancy frequency produce a strongly non-quadratic profile over a 200 m segment. This is occasionally noticeable immediately below the mixed layer. The quadratic fit in Equation 3.2 does a poor job in these areas, so it noticeably increases the strain variance. We therefore choose to remove segments that vary in the squared buoyancy frequency by more than 5 x $10^{-4}s^{-2}$ (slightly more conservative than in *Whalen et al.* (2012)). Segments were also discarded if $\langle N^2 \rangle < 10^{-9}s^{-2}$ since the strain signal at such low buoyancy frequencies is dominated by noise.

A finestructure feature that we are not correcting for is double diffusive staircases generated by salt fingering or diffusive layering (*Schmitt*, 1994). These processes have a narrowband finescale structure that falls within the scales we are considering here. While this is generally not observed to result in diapycnal mixing (for an exception see *Polzin et al.*, 2014), the resulting transport is of the opposite sign than what we expect from internal wave mixing and only results in a

small amount of energy dissipation (*Schmitt*, 2003). In these cases the magnitude of the dissipation rate would be incorrectly assigned since the assumed physics (Assumption B) are not present.

To calculate the strain variance $\langle \xi_z^2 \rangle$, each segment was detrended, windowed using a $\sin^2$ 10% taper, and spatially Fourier transformed to generate the spectrum S_{str} for each segment. The spectrum is corrected for first-differencing by dividing by the transfer function $\mathrm{sinc}^2(\kappa_z \Delta z/2\pi)$, where Δz is the vertical resolution of the segment. Argo data are either point measurements or averages over a depth interval, which is currently not identified in the metadata. Here we correct for this whenever we know the sampling scheme of the profile by dividing by the same transfer function a second time (a correction not included in *Whalen et al.* (2012)). This slightly raises the variances in the bin-averaged cases. The average increase in the dissipation rate for the Atlantic Ocean is a factor of 1.02, with a range of 1 to 2.6.

The average strain spectra for segments centered between 250 and 500 m are shown in Figure 3.2b for each experiment. The average spectra vary considerably in shape between each of the projects, ranging from LADDER where the average spectrum closely follows the reference Garrett-Munk spectrum, to MIXET where the spectrum is notably higher than the Garrett-Munk spectrum. The shape of the MIXET spectrum, and its contrast with a relatively whiter spectrum further from the equator, is consistent with previous observations of equatorial finescale strain in *Johnson et al.* (2002).

Each individual spectrum is integrated to obtain the strain variance,

$$\langle \xi_z^2 \rangle = \int_{\min(k_z)}^{\max(k_z)} S_{str}(k_z) dk_z. \tag{3.3}$$

The integration range is delineated in Figure 3.2, and begins at 100-m wavelength. This limit is chosen because we are constrained by the size of our segments (200 m), while it simultaneously avoids longer wavelength contamination by the background stratification (*Kunze et al.*, 2006). The upper limit was set to the highest wavenumber possible between the wavelengths of 10 and 40 m while satisfying $\langle \xi_z^2 \rangle \leq 0.2$ to avoid over-saturation of the spectrum which would thereby underestimate the variance (*Gargett*, 1990).

Changing the integration limits slightly, for example integrating to 120 m rather than 100 m, using a 240-m long segment, does not bias the average dissipation rate estimates (*Whalen et al.*, 2012). However, in specific locations where the spectrum considerably deviates from the GM spectrum, the integration limits can impact the result. For example, the MIXET spectra are more red than GM, indicating that changing the integration range to include smaller wavelengths would decrease the resulting strain variance. In SOFine, *Waterman et al.* (2014) also found that changing the integration limits affected the finestructure estimates. The variance estimates were only averaged together after integration following *Kunze et al.* (2006), to avoid averaging spectra of different resolutions.

The energy cascade to smaller scales via wave-wave interaction is a function of the frequency limits of the local internal wave field, and therefore dependent on latitude. This is included by the term $L(f, N)$ (*Gregg et al.*, 2003; *Polzin et al.*, 1995; *Henyey*, 1991), with dependence on the local Coriolis frequency f, the Coriolis frequency at 30° f_{30}, and segment averaged buoyancy frequency $\overline{N}$, given by

$$L(f, N) = \frac{f \ \text{arccosh}(\frac{\overline{N}}{f})}{f_{30} \ \text{arccosh}(\frac{N_0}{f_{30}})}. \tag{3.4}$$

The function $h(R_\omega)$ is given by

$$h(R_\omega) = \frac{1}{6\sqrt{2}} \frac{R_\omega(R_\omega + 1)}{\sqrt{R_\omega - 1}}, \tag{3.5}$$

where R_ω is the ratio between shear and strain, or aspect ratio of horizontal kinetic and potential energy of the internal wave field (*Polzin et al.*, 1995; *Kunze et al.*, 2006), which is variable with space and time throughout the ocean. Since we only have strain and no shear information, we are forced to assign a value for the Garrett-Munk wave field, $R_\omega = 3$ (*Cairns and Williams*, 1976; *Gregg*, 1989), reducing $h(R_\omega)$ to 1. This is also a reasonable choice for the upper 2000 m given previous global observations (Figure 20: *Kunze et al.*, 2006). Comparisons between microstructure and finestructure presented later (Section 6) show no scalar positive or negative bias that would be generated by choosing an incorrect constant for R_ω. However, using a constant R_ω rather than a variable one will cause some error (a factor of 2 if on average $R_\omega = 6$) in the individual mean dissipation rate estimates.

Maps of the average dissipation rate estimates achieved from applying this method to Argo float profiles are shown in Figure 3.3.

3.5 Comparisons

3.5.1 Finestructure and microstructure comparisons

Here we compare dissipation rates from microstructure measurements with nearby Argo-derived strain-based finestructure estimates. The locations of the chosen microstructure profiles and the corresponding finestructure profiles are shown in Figure 3.2a. All comparisons use the criterion that each Argo float finestructure estimate must be within 60 km of a microstructure profile. There also must be at least 10 Argo estimates at a given depth level to constitute a comparison. This criterion was chosen to maximize the number of projects used for the comparison and minimize the distance between microstructure and finestructure profiles. For example, increasing the minimum distance to 100 km decreases the agreement between the microstructure and finestructure estimates, while decreasing it to 50 km excludes the LADDER project. If the majority of the Argo floats are grouped around a subset of the microstructure profiles, then data from that area are used exclusively.

The one exception to this criterion is the equatorial project MIXET where Argo profiles are selected up to 30 km north or south of the microstructure measurements or 180 km east or west of the microstructure measurements. We consider these limits to be roughly equivalent to the 60 km limits imposed elsewhere because of the potentially strong zonal nature of mixing at the equator (*Gregg et al.*, 2003).

3.5.2 Determining the number of samples

For the shear version of the finescale method, *Gregg et al.* (1993) determined for their particular dataset that at least 40 independent samples are required for an estimate of the mean possessing 95% confidence limits within a factor of 2. Here

we are using a different parameterization, applied to strain rather than shear, and in this case the underlying variable of strain is not normally distributed (*Pinkel et al.*, 1991; *Pinkel and Anderson*, 1992, 1997; *Polzin*, 1996) as is true with the shear (*Gregg et al.*, 1993). Instead we take an empirical approach to approximate the number of samples required to estimate the mean dissipation rate within reasonable bounds.

To empirically gauge the quantity of samples necessary to calculate a mean with reasonable confidence limits, means are calculated from subsamples of the dissipation rate estimates within a depth range. This is replicated 5000 times for each sample size ranging between 2 and 80, allowing for repetition. Using the distribution of the means obtained for each sample size, the ratio between the 5th and 95th percentile is calculated. Figure 3.4 shows this ratio of dissipation rates between 400-600 m for the NATRE dataset using Argo-derived finestructure estimates, profile-averaged microstructure estimates, and finescale estimates derived from the CTD on the microstructure profiler.

Figure 3.4 demonstrates that, as expected, there are larger variations in the mean for smaller sample sizes than for larger sample sizes. The Argo-derived finestructure and simultaneous-CTD finestructure means are both determined within a factor of about 4 and the microstructure within a factor of 2 using 10 samples. We choose to average a minimum of 10 samples to get an estimate of the mean dissipation rate at a particular depth to allow for the inclusion of MIXET and LADDER. Ideally 50 samples or more would be chosen to reduce the uncertainty to a factor of 2 for the estimated mean.

Only NATRE is shown because it is the only project with >50 dissipation rate values for both finestructure and microstructure. Also, the majority of the projects do not possess high enough quality temperature and salinity measurements from the CTD on the microstructure profiler to use the finescale parameterization (such as due to an unpumped CTD). We therefore take the NATRE dataset as an example, and expect that data from different locations would converge to a mean at slightly different rates. For example, the finestructure from BBTRE97 and HOME converge to a factor of 5 for 10 samples. SOFine includes two very

different mixing environments, both deep and shallow, and consequently converges slower, to a factor of 8 for 10 samples. In every case averaging fewer than 5 finestructure samples is off by a factor of 10 or more, highlighting the importance of averaging to get an accurate estimate of the mean.

3.6 Results

3.6.1 Argo-derived finestructure and microstructure means

Profiles of both the microstructure and finestructure dissipation rates are presented in Figure 3.5. Each profile is composed of 200 m half-overlapping bin averages between 250-2000 m. Since the vertical resolution of the Argo profiles frequently becomes too coarse at depth for the finescale parameterization to be applied, many comparisons do not reach 2000 m. Gaps in the finestructure estimates are due to a change in the resolution of Argo float profiles at that depth. The microstructure and Argo-derived finescale profiles agree very well; the majority of the points agree within the range of the 90% bootstrapped confidence intervals. The profiles of averaged finestructure estimates also tend to exhibit a trend similar to the microstructure profiles, for example NATRE, BBRTRE97, HOME, SOFine, and MIXET all have higher dissipation rates near the top of the profile than closer to the bottom.

Figure 3.6 consolidates the comparisons between the microstructure and finestructure shown in Figure 3.5 for the dissipation rate (a) and equivalent comparisons for the diffusivity (b). The dissipation rates calculated using these two methods span three orders of magnitude, agreeing within a factor of 2 for 81% and a factor of 3 for 96% of the comparisons. Overall there is no noticeable positive or negative bias; the ratio between microstructure and finestructure dissipation rate is 1.03. However individual projects sometimes exhibit a slight bias towards over or under estimation. For example, 12 of 17 of the SOFine dissipation rate averages using microstructure are significantly larger than the finestructure esti-

mates according to the 90% bootstrapped confidence intervals. The diffusivity agrees similarly well, within a factor 2 for 83% and a factor of 3 for 96% of the comparisons.

The agreement between the finestructure and microstructure in the equatorial MIXET project is particularly intriguing. The finescale strain parameterization has not been previously tested in the unique equatorial environment. Here we find that 5 of 6 of the MIXET comparisons match within a factor of 3. This agreement adds confidence to the pattern of an elevated dissipation rate along the equator (Figure 3.3) and the effectiveness of the form of latitudinal dependance in Equation 3.4 (*Gregg et al.*, 2003; *Polzin et al.*, 1995; *Henyey*, 1991). Adding further credence, *Hennon et al.* (2014) find evidence for a band of high internal wave activity along the equator at 1000 m. In their observations the authors use Argo float time series data collected while the float was parked at depth between sampling vertically to generate the profiles used in our analysis. These internal waves may be dissipating through wave-wave interactions as described by the finescale parameterizations. However, caution should be used when interpreting this agreement since the assumptions underlying the finescale parameterization may be violated near the equator. Specifically, the red MIXET spectra (Figure 3.2b) may be due to contamination from non-internal wave equatorial processes or a significant deviation from the Garrett-Munk reference internal wave field near the equator. Either possibility could cause spurious dissipation rate estimates in equatorial regions, despite the agreement we see at the MIXET location.

The dissipation rate distributions calculated from both the Argo-derived finestructure estimates and microstructure between 250-500 m are shown in Figure 3.7 in the form of probability density functions (PDFs). Superimposed on each PDF are dots representing the mean in this depth range. The microstructure and finestructure have similar distributions at high values, while differing substantially at low values. Due to the non-Gaussian nature of the distributions, the large values are the most important for the averages, which is where the PDFs are in better agreement.

There are no low dissipation values in the microstructure estimates since

these calculations typically include a minimum dissipation value, for example 10^{-11} W kg^{-1} in NATRE (*Toole et al.*, 1994) or 3x10^{-9} W kg^{-1} to 3x10^{-8} W kg^{-1} in HOME (*Lee et al.*, 2006), depending on the noise floor of the measurements. As seen in Figure 3.7, including this cutoff does not have a large effect on the averages. The steeper gradient in the lower values of the microstructure PDFs may also be due to the steepening of the PDFs at low values with added noise. *Gregg et al.* (1993) shows that adding random noise to finestructure data shifts the lower tail to the center of the distribution, thus facilitating better agreement. This is also true for the PDFs presented.

3.6.2 Seasonal variability of dissipation rates

These comparisons implicitly assume that both the microstructure and finestructure Argo estimates, sometimes months or even decades apart, are both measuring the mean dissipation rate at a particular location. If the dissipation rate varies intermittently, seasonally or decadally, this may cause either measurement to be an inaccurate representation of the mean state. Here we evaluate this assumption by investigating whether seasonal variability is significant at both the specific microstructure project locations and globally.

The seasonal cycle in the dissipation rate is presented in Figure 3.8 using the Argo finestructure for NATRE, BBTRE97, HOME, and SOFine. Projects included have at least 10 estimates in each season for at least one depth range. The profiles of 200 m half-overlapping dissipation rate means in each season are depicted in Figure 3.8a. The corresponding spectra between 250-1000 m are plotted in Figure 3.8b. Both the profiles and spectra for NATRE (northern hemisphere) and BBTRE97 (southern hemisphere) show larger values in winter and spring than the summer and fall. The seasonal differences between the dissipation rate profiles are at most a factor of 2. The timing is consistent with the winter peak in near-inertial energy (*Alford and Whitmont*, 2007; *Silverthorne and Toole*, 2009; *Whalen et al.*, 2012). We do not find a clear seasonal cycle in the dissipation rate for the HOME and SOFine datasets, which is either indicative of no seasonal cycle or an insufficient number of estimates to consider the seasonal cycle (see Section 3.5b).

The shape of the spectra in Figure 3.8b are consistent across all seasons for a particular project. For example, a winter BBTRE97 spectrum is more similar to BBTRE97 spectra of any season than any of the spectra at other locations. One exception to this is the high wavenumber portion of the SOFine spectrum, where the winter and fall spectra are more blue than during the remainder of the year.

In other regions the seasonal cycle is larger than observed in the NATRE, BBTRE97, HOME, and SOFine projects. Figure 3.9 shows the dissipation rate seasonal cycle from finestructure for 10° latitudinal bands between 50°S to 50°N and 250-1000 m, averaged over all longitudes. Each profile is constructed from half-overlapping means of at least 200 estimates, and a majority of the averages include over 1000 estimates. The largest variation is a factor of 2-5, occurring between March/April and September/October along the latitude band rich in storm tracks, 30°-40° in both hemispheres. The longitudinally averaged buoyancy frequency does not have an equivalent cycle (not shown). In contrast to the stormy 30°-40° latitudes, there is no significant seasonal cycle in the dissipation rate along 10°S-10°N, and only a slight seasonal cycle in the other latitudinal ranges. All the microstructure projects considered here are at latitudes with low seasonal variability, outside of the 30°-40° range.

3.7 Discussion

We have presented comparisons between finescale estimates of the dissipation rate and diffusivity from Argo float profiles and microstructure measurements to 2000 m depth from six projects. The measurements were taken at different locations (separated up to 60 km) and various times (up to decades apart). The comparisons were made in diverse environments, from the equator to the ACC, and from above abyssal plains to above ocean ridges. These locations represent a range of wind and tidal power input and topographic roughnesses. Of these Argo-derived strain finestructure estimates of the dissipation rate, 81% agreed within a factor of 2, and 96% agreed within a factor of 3. This good agreement over a wide range of open ocean conditions strongly suggests that the underlying theory

behind the finescale parameterization provides an accurate scaling, however this finding is not definitive since the data presented here do not directly measure the nonlinear interactions on which this theory is based. Additionally, these results suggest that these methods can yield reasonable estimates of the mean dissipation rate.

Previous regional studies comparing strain finestructure to microstructure measurements have yielded consistent results. In the Southern Ocean near Drake Passage, finestructure from the ship CTD and microstructure dissipation rate estimates from nearly identical times typically agreed within a factor of 2-3, or at most a factor of 4 below 250 m (*Frants et al.*, 2013), similar to what we find.

A second regional study, SOFine near the Kerguelen Plateau (*Waterman et al.*, 2014), observed that the microstructure and finestructure agree within a factor of 2 far above the seafloor (>1500 m), but finestructure tended to overestimate the dissipation rate closer to the bottom. *Waterman et al.* (2014) attribute this near bottom bias to non-GM conditions caused by lee-waves generated in this region from geostrophic flow over rough topography, indicating that the finescale parameterization assumptions are not applicable close to the bottom in this environment. The majority of the Argo float profiles are not within this regime since they are >1500 m above the seafloor. Therefore, we find similar (within a factor of 3) agreement between the microstructure and Argo-finestructure dissipation rates as *Waterman et al.* (2014) do far above the seafloor. In our case the Argo finestructure slightly underestimates the dissipation rate.

In the SOFine region, temporal variability of internal waves may be the source of the uniformly smaller Argo finestructure dissipation rates via a mechanism similar to what is observed near Drake Passage (*Sheen et al.*, 2014). Since lee wave generation is a function of current speed over the topography (*Bell*, 1975; *Nikurashin and Ferrari*, 2010), and the fronts in Kerguelen Plateau region are particularly variable for the ACC (*Sokolov and Rintoul*, 2009), we expect the internal wave generation and dissipation rate to vary as well. A mooring record at Kerguelen does show unusually high velocities during the time when the microstructure measurements were taken (S. Waterman, personal communication

2014). Therefore temporal variability may be the source of the consistent underestimation (factor of 2-3) of the Argo finestructure compared to the microstructure for this project.

Considering six different projects in a variety of environments expands the previous Southern-Ocean focus of regional comparisons between microstructure and strain-based finestructure estimates. Of the projects considered here, only BBTRE97, SOFine, and HOME have above-average tidal power input and only SOFine has above-average wind power input. Environments that are still missing from this comparison include under storm tracks (30°-40°) and high latitudes (>50°). Expanding on the single-station data from the MIXET project with more stations near the equator would also be useful. Evaluation of the strain-finescale parameterization as a means to detect a seasonal cycle would also be worthwhile. This is because the wind-induced near-inertial waves that are likely to contribute to the seasonal cycle have a high shear-to-strain ratio, which we are assuming to be constant. This would result in an under-estimation of the seasonal cycle since the shear-to-strain ratio, and thus Equation 3.5, would be biased low. A comparison between winter and summer microstructure and finestructure at a site with significant near-inertial wind forcing would be one way to discern if the strain parameterization is accurately representing the seasonal cycle.

Possible sources of the factor of 2-3 difference between the microstructure and finestructure averages include small violations of the parameterization's assumptions, undersampling the temporal variability, and averaging too few samples to calculate the mean. We choose to use at least 10 samples to construct each average, which according the the NATRE dataset implies that 90% of the time the finestructure mean estimates will be within a factor of 4 of each other, and microstructure will estimate the mean within a factor of 2. This is similar to the spread of the comparisons presented here, and may be the source of a significant portion of the factor of 2-3 difference we observe. This also suggests that it is necessary to average a number of estimates to achieve a reliable measure of the mean dissipation rate at a location.

The energy in the internal wave field fluctuates on seasonal and tidal

timescales, yet in these comparisons we are assuming that the microstructure is measuring the mean dissipation rate in an area despite sampling over only a period of weeks. At a subset of locations (NATRE, BBTRE97, HOME, and SOFine) used in this study this assumption is reasonable since the seasonal variability is small (at most factor of 2) or undetectable (Figure 3.8). The remaining locations, LADDER and MIXET, are at low latitudes, which in the global averages do not show any seasonal cycle (Figure 3.9). Tidal variability should not be significant in these comparisons since the microstructure projects considered here span either a full spring-neap cycle, are a great distance from internal tide generation sites, or are far above the topography. At these locations, seasonal and tidal variability will likely have a negligible effect on microstructure and finestructure estimates of the mean dissipation rate.

The mean dissipation rate and diffusivity are of wider interest for applications such as understanding the oceanic energy budget and overturning circulation. Estimating the mean dissipation rate is difficult due to the high levels of variability approximately log-normally distributed over multiple spatial and temporal scales. Here we find evidence from finestructure estimates that seasonal variability is not very important for determining the global mean dissipation rate in the upper ocean over most latitudes, assuming we are adequately resolving the seasonal cycle. This gives us confidence that measurements at these latitudes, such as microstructure projects, can on average accurately measure the mean dissipation rate as assumed in *Waterhouse et al.* (2014). However, at latitudinal ranges with strong winter storms (30°-40°) there is a significant cycle of a factor of 2-5 in the dissipation rate estimates from finestructure. At these latitudes using data from only one season could lead to noticeable inaccuracies in the calculated mean. This is consistent with previous results that also find that spectra are typically invariable over time on the scales we consider here except for some locations where seasonal cycle is observed (*Polzin and Lvov*, 2011). The relative steadiness of the dissipation rate on monthly to seasonal timescales over the majority of the ocean suggests that measurements of the dissipation rate in a region over these timescales are sufficient to produce reasonable average estimates of ocean mixing.

3.8 Conclusions

There are three main conclusions that arise from this study. First, the assumed fundamental physics behind the finescale parameterizations is consistent with our observations over a wide range of internal wave environments. Specifically, our findings are compatible with the notion that the majority of the turbulent energy dissipation in the open ocean is caused by internal waves transferring their energy to smaller scales through nonlinear interactions. Second, the mean dissipation rate is generally steady in the upper ocean over monthly to seasonal timescales. One notable exception to this is a significant seasonal cycle beneath storm tracks. Finally, the finescale strain parameterization is an effective tool for estimating the mean dissipation rate and diffusivity in the open ocean, provided that appropriate averaging is done over the internal wave field environment of interest.

3.9 Acknowledgments

Many thanks to Glenn Carter, Eric Kunze, Craig Lee, Jonathan Nash, Alberto Naveira Garabato, Kurt Polzin, Andreas Thurnherr, Tom Sanford, Louis St. Laurent, and Stephanie Waterman, for contributing and assisting with the microstructure data. Additionally, the manuscript was improved by helpful comments by Eric Kunze and Kurt Polzin, along with awesome comments from two anonymous reviewers. We are also grateful to the Argo PIs who provided information about whether Argo data were bin averaged or were point measurements. This work was funded by NSF OCE-0927650 and OCE-1259573. This chapter has been published in its entirety in: Whalen, C. B., J. A. MacKinnon, L. D. Talley and A. F. Waterhouse, 2015. Estimating the mean diapycnal mixing using a finescale strain parameterization. *J. Phys. Oceanogr.*, 45, 1174-1188

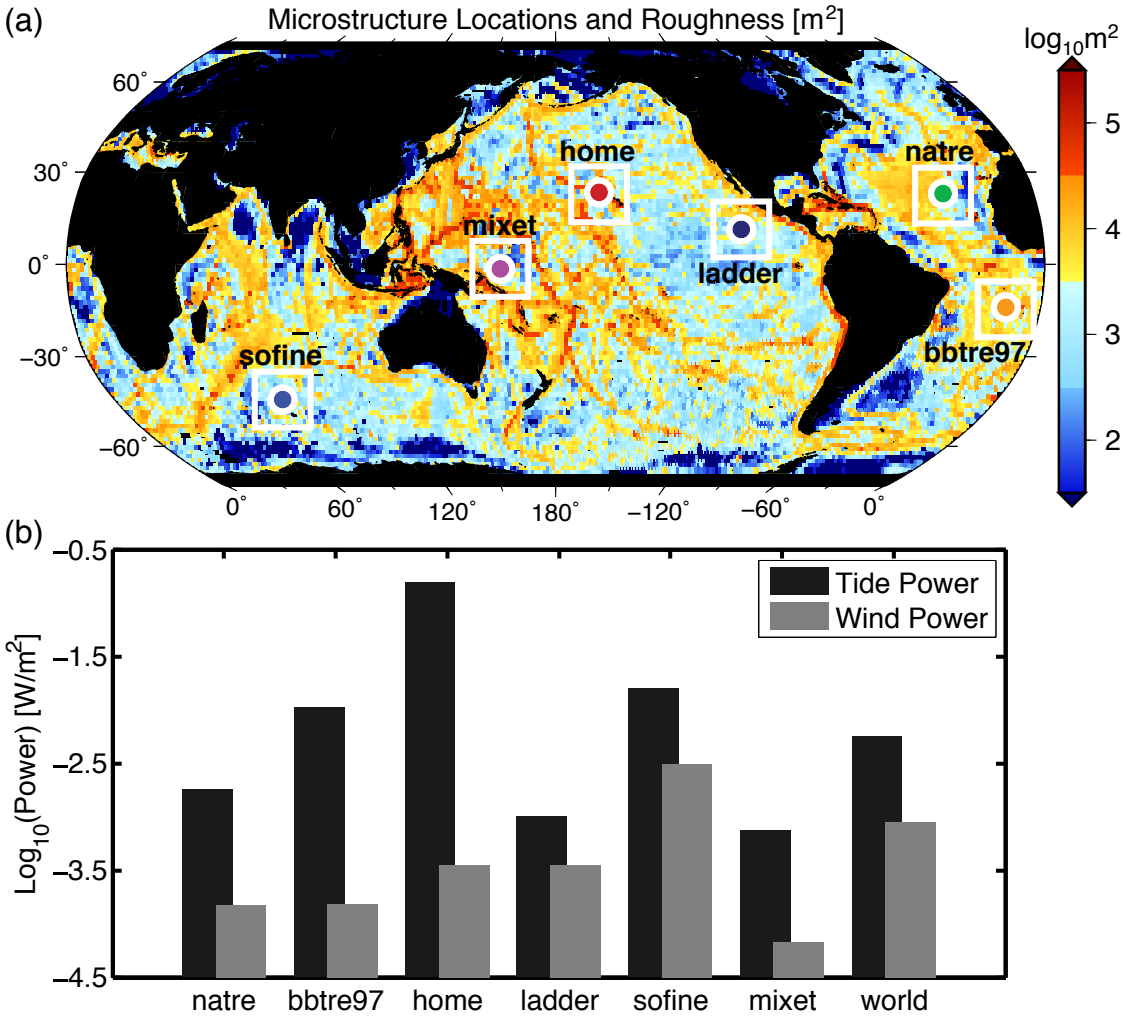

Figure 3.1: (a) Locations of the microstructure projects plotted over regions with a variety of sea-floor roughnesses as calculated from the *Smith and Sandwell* (1997) 14.1 ship-track dataset. (b) Power input into internal waves from the wind and tides as described in *Waterhouse et al.* (2014) for the microstructure locations. The global averages are shown on the right.

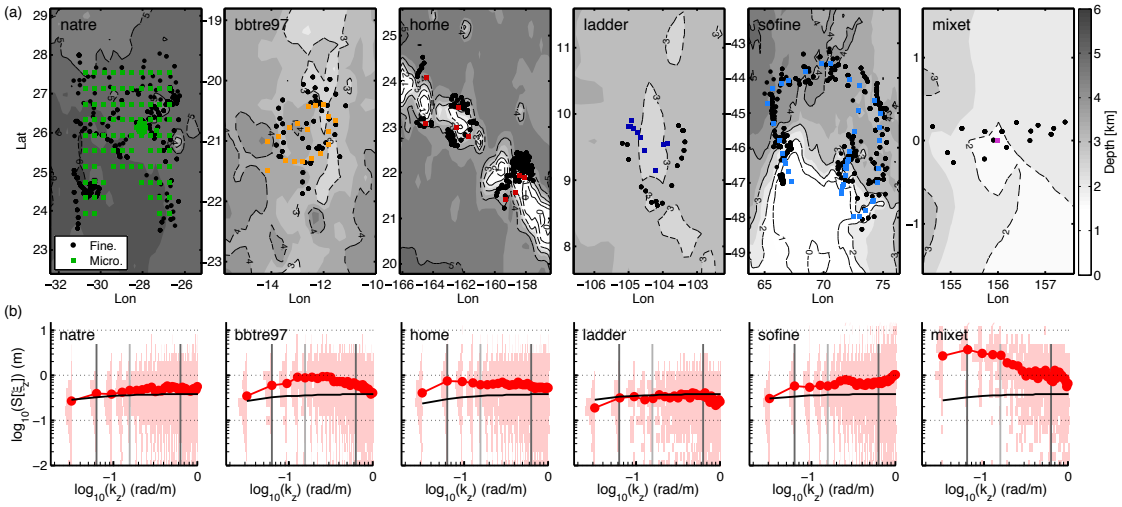

Figure 3.2: (a) Locations of the microstructure profiles (colored) that are in close proximity to the Argo profiles (black) used to calculate finestructure for each project. (b) Averaged strain spectra (red) between 250 and 500 m along with the Garrett-Munk spectrum (black). Horizontal histograms of each average are in pink. Vertical dark grey lines are positioned at wavenumbers corresponding to the absolute integration limits of 100 m and 10 m wavelengths. The light grey line corresponds to the 40 m wavelength, the smallest wavelength required for integration.

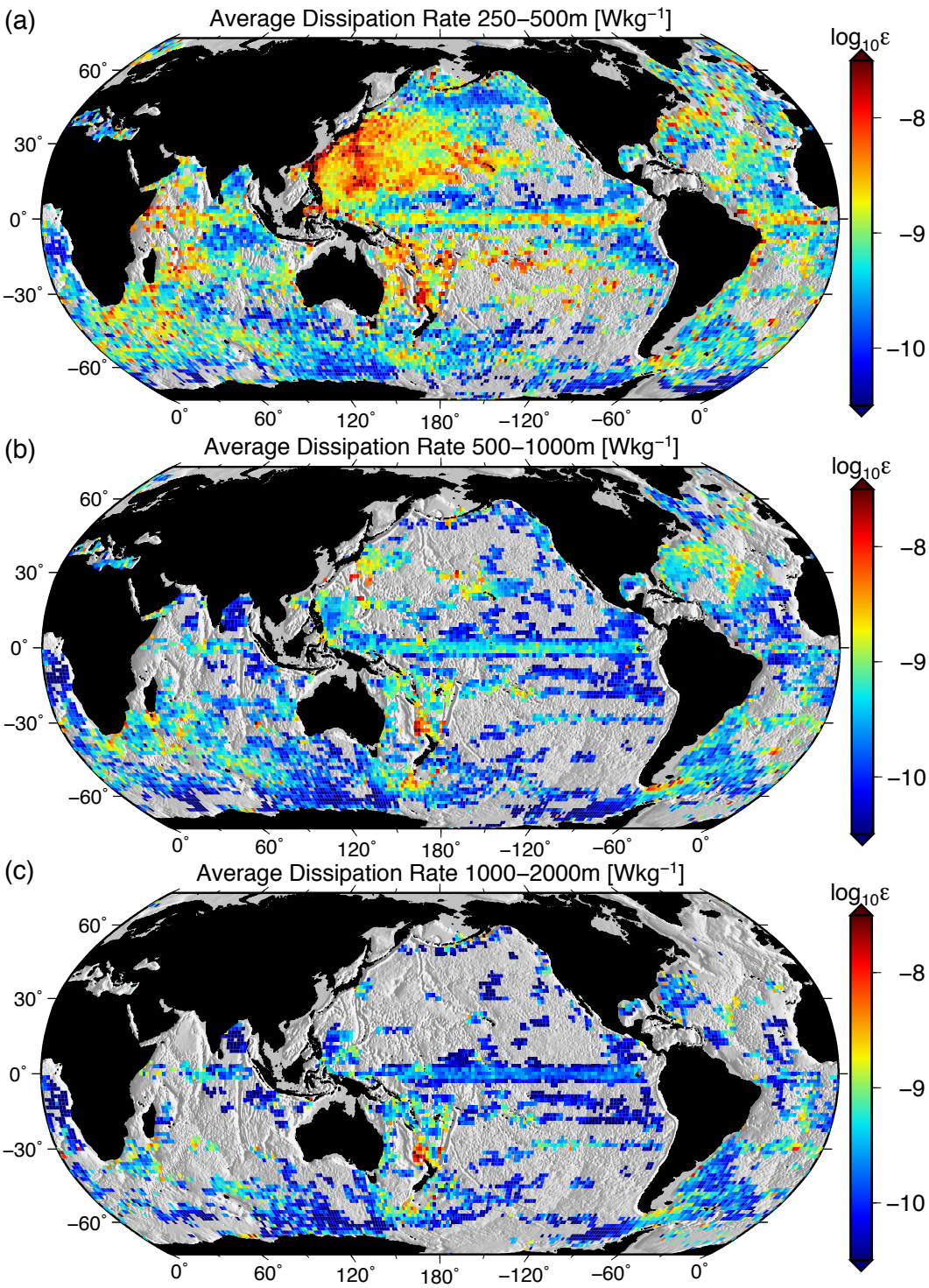

Figure 3.3: Average dissipation rate ϵ estimates derived by applying strain finestructure methods using Argo profiles between (a) 250-500, (b) 500-1000, and (c) 1000-2000 m. At least three estimates are required to show an average within a 1.5 degree square bin. These figures are updated from *Whalen et al.* (2012) and include data from 2006-2014.

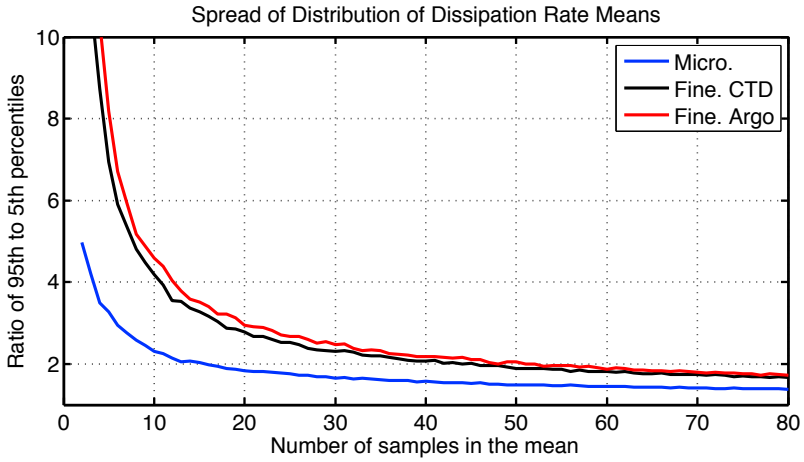

Figure 3.4: The distribution of dissipation rate means between 400-600 m was calculated using 5000 means of 2-80 subsamples of estimates from the NATRE dataset. Shown here is the ratio between the 95th and 5th percentile of these distributions as a function of number of samples contributing to the means for microstructure (blue) and finestructure using concurrent profiles from the CTD on the microstructure instrument (black), and Argo-derived finestructure (red).

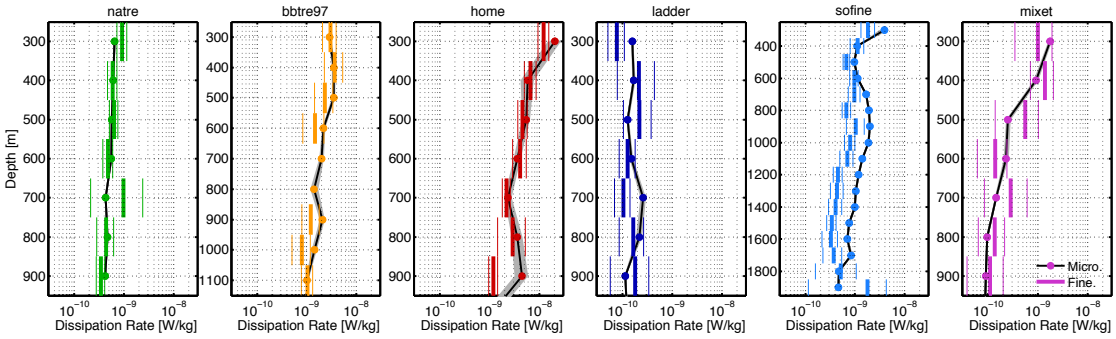

Figure 3.5: Mean dissipation rate (W/kg) profiles from 200-m half-overlapping depth bins from microstructure (dots), and the Argo finestructure (bars) generally at most 60 km away from a microstructure profile. The 90% bootstrapped confidence intervals are represented by either bars or gray shading.

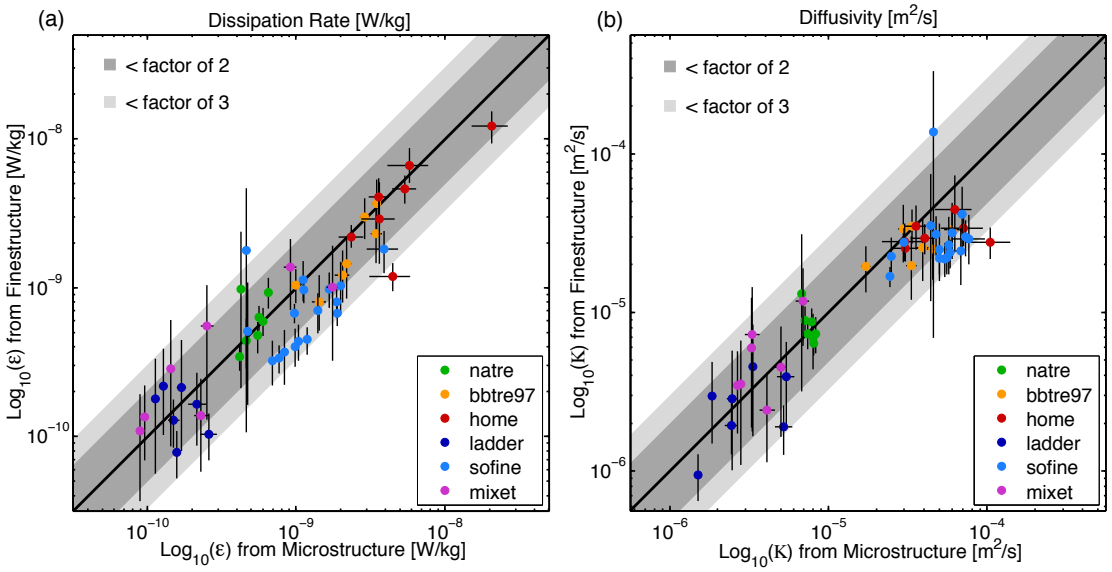

Figure 3.6: Comparisons between Argo-derived finestucture estimates and microstructure measurements for (a) the dissipation rate ϵ and (b) the diffusivity K between 250 and 2000 m with bootstrapped 90% confidence intervals. The means are identical to the profiles shown in Figure 3.5. Agreement within a factor of 2 or 3 is designated by the gray bands.

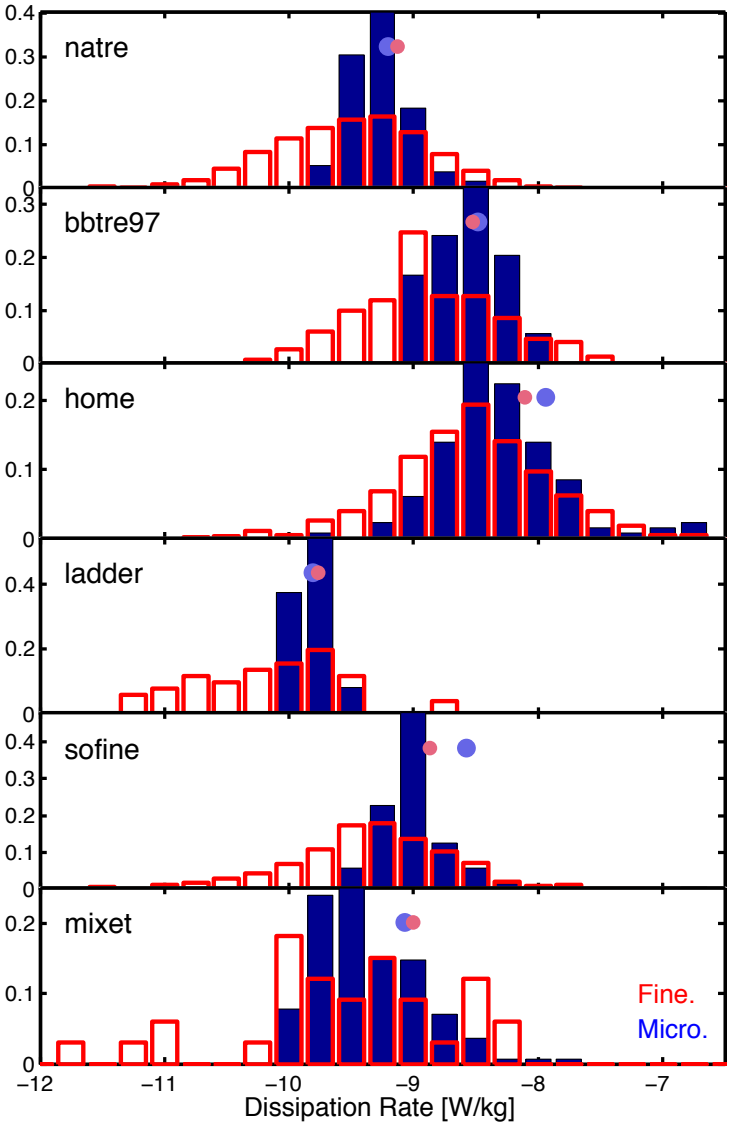

Figure 3.7: PDFs of the dissipation rate (W/kg) derived from microstructure (blue) and Argo-derived finestructure (red) between 250 and 500 m, with means of each distribution (colored dots).

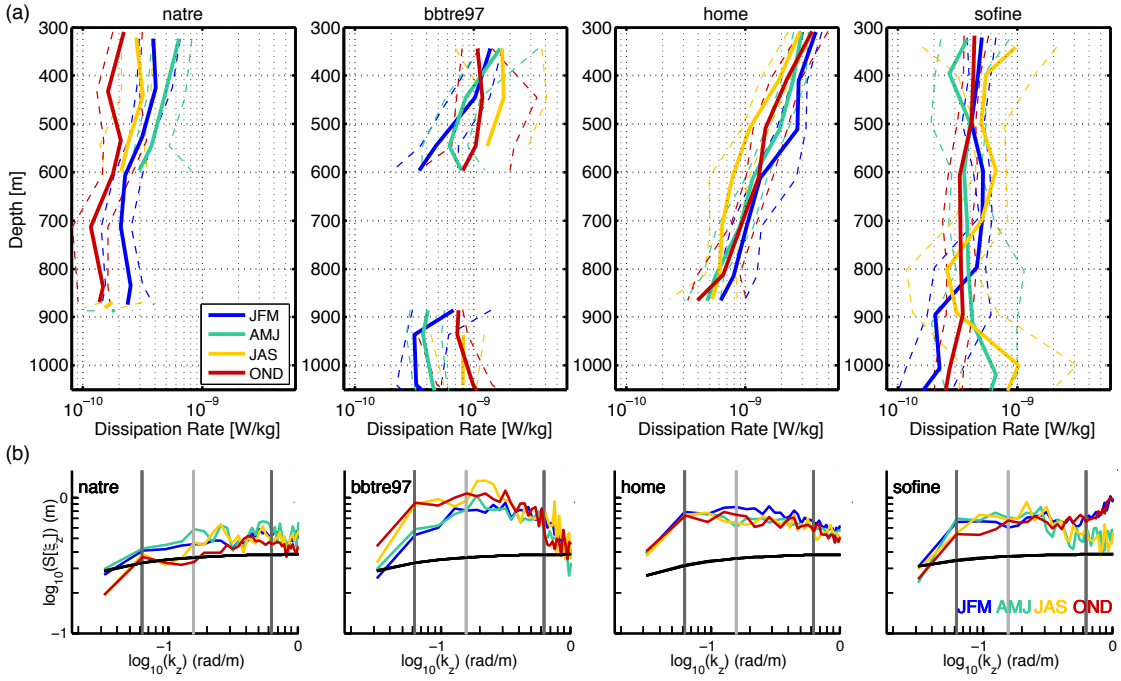

Figure 3.8: (a) Profiles of the half-overlapping mean dissipation rates from Argo-derived finestructure estimates colored according to each season with 90% bootstrapped confidence intervals. Only averages with at least 10 estimates are shown, and only projects are shown that fit this requirement for every season. (b) The averaged spectra between 250-1000 m for each season. The Garrett-Munk spectrum is shown in black and the vertical lines designate the wavenumbers corresponding to the upper wavelength integration limit (100 m) and the range for the lower limit (10-40 m).

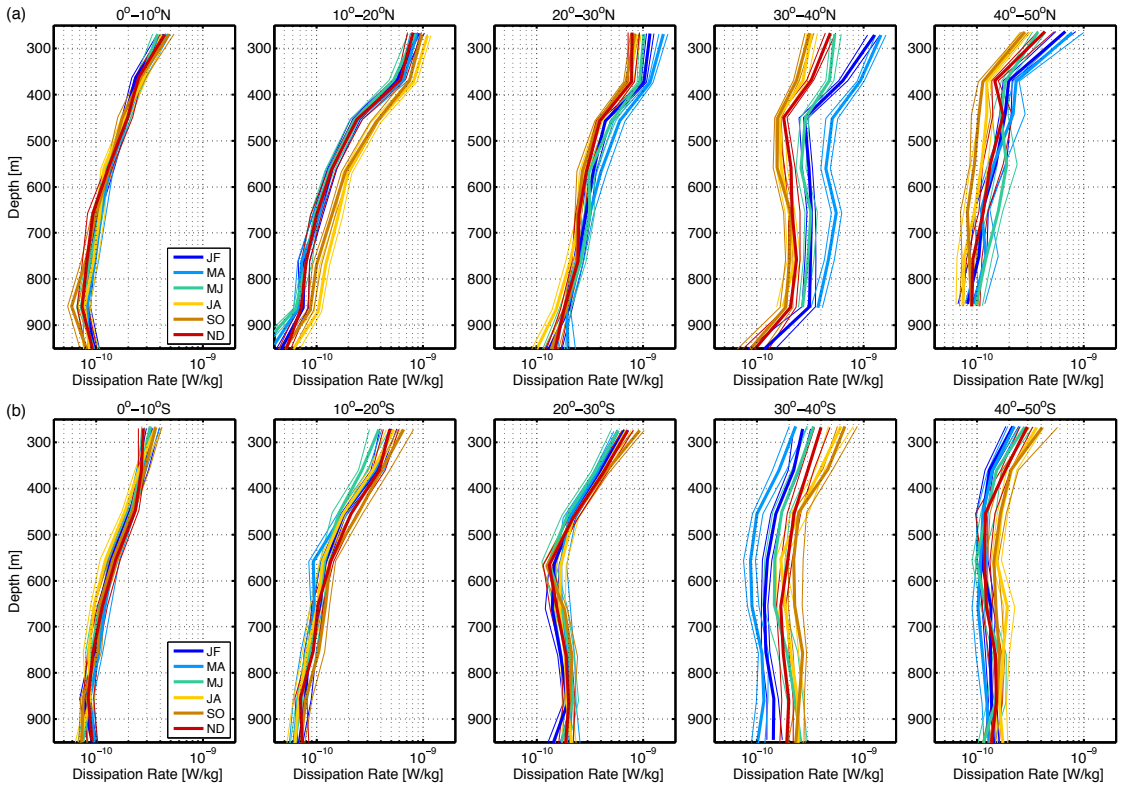

Figure 3.9: The seasonal cycle in the Argo-derived finestructure dissipation rate for 10 degree latitudinal bands across the entirety of the northern hemisphere (top) and the southern hemisphere (bottom). Each profile is constructed from half-overlapping means as in Figure 3.8. The thin lines are 90% bootstrapped confidence intervals. At least 200 estimates are required for an average and over half of the averages include over 1000 estimates.

Chapter 4

Linking eddy kinetic energy and near-inertial internal waves to patterns of diapycnal mixing at midlatitudes

Internal waves generated from the tides and winds are fated to eventually dissipate their energy through a diverse array of mechanisms. Energy dissipation rate estimates calculated from density profiles using finescale methods can be used to detangle the processes leading to the internal waves' demise on regional and global scales. Here we apply these finescale methods to the Argo float array to produce over 800,000 dissipation rate estimates throughout the ocean. Previous observations show that the strength of the eddy kinetic energy is correlated with the median dissipation rate calculated in this way. We explore possible mechanisms driving this correlation by co-locating each dissipation rate estimate with the nearest eddy and and the history of the wind-driven near-inertial energy flux at that location. We find evidence that the mesoscale is modulating the near-inertial energy input from the winds; in areas of high eddy kinetic energy the dissipation rate is larger with an increase in the near-inertial energy flux and the amplitude of the seasonal cycle in the dissipation rate is larger. Additionally, there is an

elevated dissipation rate in areas of high eddy kinetic energy or when the velocity of the closest eddy is large that is independent of the wind forcing, suggestive that non-near-inertial wave dynamics may also be critical for setting this pattern.

4.1 Introduction

Energy near the Coriolis frequency is a prominent feature in the internal wave field throughout the ocean, but the complete story from generation to destruction remains elusive. One known source of these waves is the winds, which force the ocean and contain a spectrum of frequencies over a range of scales. The components of the wind field that are crucial for the generation of internal waves rotate at the inertial frequency, the oceanic mixed layer subsequently mirrors this motion, also ringing at the inertial frequency. These inertial oscillations in the mixed layer can then initiate near-inertial waves with large horizontal scales and often large shear components.

A clear understanding of the genesis and fate of these near-inertial waves is complicated by the fact they are thought to be mostly forced near midlatitude storm tracks since these storms possess a significant amount of wind at the correct frequency to generate the waves. Near the ocean's surface, and especially in western-boundary current regions underneath storm tracks, there also lies an energetic mesoscale. What makes this problem especially compelling is that there is a host of potential mechanisms that the mesoscale is thought to interact with, and even generate, near-inertial waves due to the similarity in time scales between these waves and the geostrophic flow. This provides an opportunity for complicated physics and subsequent patterns in the energy dissipation rate.

Observations suggest that there is a correlation between the turbulent kinetic energy dissipation rate and the eddy kinetic energy on a global scale (*Whalen et al.*, 2012), however the reasons for this correlation remain unclear due to the complex nature of the mesoscale and the large number of possible mechanisms responsible. Process-specific observations provide evidence that in particular cases mesoscale features interact with, and possibly generate, internal waves. Eddies,

for example, are associated with elevated internal-wave activity (e.g. *Kunze*, 1995; *Lee and Niiler*, 1998; *Joyce et al.*, 2013), and dissipation rate (*Padman et al.*, 1990; *Kunze*, 1995; *Sheen et al.*, 2015). Fronts are also associated with elevated internal wave energy (*Fu*, 1981; *Kunze and Sanford*, 1984; *Rainville and Pinkel*, 2004; *Alford et al.*, 2013). An array of processes have been proposed that may explain these observations, but it is not yet apparent which mechanism or selection of mechanisms may be significant enough on a global scale to explain the observed link between the dissipation rate and the strength of the eddy field.

A category of mechanisms, the generation of internal waves from mesoscale features, has been explored through theoretical and modeling studies. There is typically a time scale separation between the slowly varying mesoscale and the relatively fast internal waves, and one might expect that this would preclude internal wave generation from the mesoscale. However, in a constantly changing real ocean there are quickly varying components of the motion of the mesoscale, which can cause resonance and generate internal waves in the surrounding ocean (*Vanneste*, 2013; *Danioux et al.*, 2012). This can occur when the Rossby number is large, for example during frontogenesis (*Griffiths and Reeder*, 1996; *Reeder and Griffiths*, 1996). Another way to bridge the timescale gap is by the generation of typically large horizontal scale internal waves in small Froude number conditions as modeled in *Ford* (1994). In contrast to a previously balanced flow spontaneously generating internal waves, there also can be classical Rossby-adjustment in which an initially unbalanced flow radiates waves as it undergoes geostrophic adjustment and shifts to a balanced state (*Rossby*, 1937).

These processes have the potential to transfer energy from the mesoscale to the internal wave field. This implies that they may be important in the energy cascade of internal waves to dissipative scales, and also indicates that they may play a role in the dissipation of the mesoscale. How the mesoscale dissipates its energy is currently a significant gap in our understanding in the global energy budget (*Ferrari and Wunsch*, 2008, 2010), which is especially critical since the mesoscale contains a large portion of the oceanic kinetic energy (*Ferrari and Wunsch*, 2010). Modeling results indicate that inertial waves may be important for dissipating

energy from the mesoscale (*Molemaker et al.*, 2005).

A second category of mechanisms linking internal waves to the mesoscale involve the vorticity of the mesoscale altering the internal waves' scales, speeds, and dissipation patterns. Mesoscale eddy fields are composed of a complex assortment of features including eddies in various stages of formation and destruction, along with filaments, all associated with their own vorticity signature. Theory (*Young and Jelloul*, 1997) and simulations (*Klein et al.*, 2004; *Danioux et al.*, 2008) suggest that the vorticity anomalies in these fields can break up large horizontal scale near-inertial waves, and cause the internal waves to disperse, with the lowest modes propagating downwards faster, possibly dissipating their energy more quickly. The sign of the vorticity is also thought to be important; modeling results have shown stronger and deeper signatures of near-inertial energy in anticyclonic vorticity anomalies in contrast with cyclonic vorticity (*Danioux et al.*, 2008).

One specific example of this type of mechanism involves a near-inertial wave interacting with the vorticity field of an anticyclonic eddy. The sign of the eddy vorticity lowers the effective Coriolis frequency, allowing the eddy to function as a waveguide, and thus allows internal waves to exist inside the eddy that cannot exist outside, trapping the wave within the eddy (*Kunze*, 1995; *Joyce et al.*, 2013) or front (*Shcherbina et al.*, 2003). Theory and ray-tracing simulations suggest that the internal waves may then reach a critical layer beneath the eddy core causing the vertical scales to rapidly shrink, triggering diapycnal mixing (*Kunze*, 1985, 1995). Observations supporting dissipation in the critical layer include those showing elevated dissipation rates beneath eddy cores (*Padman et al.*, 1990; *Kunze*, 1995; *Sheen et al.*, 2015).

Another possible process involves the capture of internal waves through the horizontal strain in the mesoscale field (*Bühler and McIntyre*, 2005; *Polzin*, 2008). If an internal wave encounters an eddy, the horizontal strain field of the eddy can cause the horizontal wavenumber of an internal wave to increase exponentially. Since the horizontal wavenumber is linked to vertical wavenumber this will exponentially change the vertical wavenumber via the dispersion relation, and capture the inertial wave within the eddy. The captured wave is thought to eventually

break, dissipating energy. Observations consistent with this scenario have been described in *Polzin* (2010).

An additional process involves near-inertial waves dissipating their energy via critical layers in strongly sloping isopycnals of a front or an eddy. Ray tracing simulation suggest that for strongly sloping isopycnals near-inertial rays reach critical layers that track these isopycnals (*Whitt and Thomas*, 2012), which would lead to dissipation. This has been observed along fronts, for example in the Gulf Stream the survey described in *Inoue et al.* (2010) there are lines of ageostrophic shear of alternating sign running parallel to the sloping isopycnals along the front (*Whitt and Thomas*, 2012).

This paper considers the correlation between eddy kinetic energy and the dissipation rate derived from a finestructure parameterization applied to Argo profiles, specifically focusing on mid-latitudes. We investigate why the correlation between eddy kinetic energy and finestructure estimates of the dissipation rate that was demonstrated in *Whalen et al.* (2012) may exist by associating each dissipation rate estimate with the closest mesoscale eddy, and the history of the near-inertial energy flux from a slab model at that point in space and time. These two tools are used to evaluate mechanisms described above to suggest possible reasons for the correlation between eddy kinetic energy and dissipation rate at mid-latitudes.

4.2 Data

4.2.1 Argo

The global Argo float array is a freely-available dataset of pressure, temperature, and salinity profiles from 2000 m depth to the ocean's surface (www.argo.net/). Each float typically profiles every 10 days and then remotely sends the data collected via satellite. Here we use high vertical resolution profiles (typically 2-10 m) from 2006-2015 to estimate the dissipation rate using a finestructure parameterization.

4.2.2 Eddy Kinetic Energy

A map of the mean eddy kinetic energy product used here is presented in Figure 4.1a (Lumpkin, pers. comm.). The time-mean version of this dataset can be found at http://www.aoml.noaa.gov/phod/dac/ (*Lumpkin and Garraffo*, 2005). The mean eddy kinetic energy product was calculated using the global surface drifter dataset as $\langle u'^2 \rangle$, which is found by applying a five day low-pass filter to each six-hour drogued drifter observation, removing the tides and inertial oscillations, and separating the mean velocity from the deviation $u = \bar{u} + u'$.

4.2.3 Eddy Product

Eddy locations are found using the Chelton eddy product (v5) available at http://cioss.coas.oregonstate.edu/eddies/. The product uses AVISO satellite sea level anomaly data to identify eddies between 1992 and 2012. The product also includes eddy diameter, amplitude, and calculated rotational velocity. The details surrounding the method used to locate these eddies and their associated characteristics can be found in *Chelton et al.* (2011).

The median eddy velocity of eddies in this product is shown in Figure 4.1b, where western boundary current extension regions typically have large median eddy velocities. The majority of the ocean has a distribution of both strong and weak eddies. However, by comparing maps of the number of detected eddies possessing velocities smaller than the median (Figure 4.1c) and larger than the median (Figure 4.1d), some regions (e.g. the Kuroshio extension) only contain strong eddies, while others (e.g. the northeastern Pacific) only contain weak eddies.

4.2.4 MERRA Wind Stress

The Goddard Earth Observing System Data Assimilation System Version 5 is used to generate the MERRA wind stress product that can be found at lhttp://gmao.gsfc.nasa.gov/merra/. MERRA provides hourly wind stress reanalysis data on grid of 0.5° latitude by 2/3° longitude grid.

4.3 Methods

4.3.1 Argo Dissipation Rate Estimates

Over 800,000 dissipation rate estimates were calculated from Argo float density profiles using a finescale strain parameterization that was developed by numerous authors (*Henyey et al.*, 1986; *Gregg and Kunze*, 1991; *Polzin et al.*, 1995; *Kunze et al.*, 2006; *Polzin et al.*, 2014), updating the analysis of *Whalen et al.* (2015) using more Argo profiles. The approach uses the vertical wavenumber spectra of 200 m segments of each density profile as a proxy for the energy of the internal wave field at that location. Using what we know about a typical oceanic internal wave environment the method can provide and estimate the turbulent dissipation rate for that location. Please see *Whalen et al.* (2015) for details concerning the application of this finescale method to Argo density profiles. The finescale estimation method has been shown to agree quite well with microstructure measurements; average Argo-derived estimated dissipation rate profiles agree within a factor of 2-3 of average microstructure profiles (*Whalen et al.*, 2015). A map of the updated dissipation rate estimates from between 250-500 m is shown in Figure 4.2b.

4.3.2 Eddy and Dissipation Rate Estimate Matching

Each Argo-derived dissipation rate estimate was matched with the closest detected eddy from the Chelton eddy product. Eddy locations and statistics in this product are provided every 7 days. Here we first interpolate the locations to produce a daily dataset. For each one day time step all Argo-dissipation rate estimates are found that are within 800 km of a detected eddy, and subsequently matched to the closest eddy. This process is repeated for all time steps, matching every dissipation rate estimate with an eddy, provided that there is a eddy detected within 800 km of the dissipation rate estimate. Due to the temporal ranges of Argo and the Chelton eddy product, matches are only made for the 2006-2012 year range.

4.3.3 Slab Model Near-Inertial Flux

A slab model following a number of authors (*Pollard and Millard*, 1970; *D'Asaro*, 1985; *Alford and Gregg*, 2001; *Plueddemann and Farrar*, 2006) was used to generate estimates of the near-inertial flux from the winds into the thermocline. We briefly explain the model as it is used here; please see the previous authors for more details.

The velocity of the mixed layer (u and v) can be described by the equations,

$$\frac{du}{dt} - fv = \frac{\tau_x}{H} - ru, \text{and} \tag{4.1}$$

$$\frac{dv}{dt} - fu = \frac{\tau_y}{H} - rv, \tag{4.2}$$

where f is the Coriolis frequency, H is the mixed layer depth, τ is the wind stress, and r is a chosen damping constant. The inverse of this damping constant $1/r$ ranges between 1-5 days in observations (*Plueddemann and Farrar*, 2006) or 1-10 days (**?**). Here we choose $1/r = 5$ days.

For clarity we define the following complex variables,

$$T = \frac{\tau_x + i\tau_y}{\rho}, \;\; Z = u + iv, \;\; \text{and} \;\; \omega = r + if,$$

allowing equations 4.1 and 4.2 to be rewritten as

$$\frac{dZ}{dt} + \omega Z = \frac{T}{H},$$

which has solutions in the form

$$Z = Z_0 e^{-ift - rt}.$$

These solutions can be divided into a sum $Z = Z_E + Z_I$ of steady (Ekman, Z_E) and oscillating (near-inertial, Z_I) components, where the Ekman part is given by

$$Z_E = \frac{T}{\omega H}.$$

Assuming the mixed layer depth does not change with time, the equation for the time dependent part Z_I is

$$\frac{dZ_I}{dt} + \omega Z_I = -\frac{dZ_E}{dt} = -\frac{dT}{dt}\frac{1}{\omega H}$$

Multiplying by Z_I^*, the complex conjugate of Z_I, produces the energy equation:

$$\frac{d|\frac{1}{2}Z_I|^2}{dt} = -r|Z_I|^2 - Re\left[\frac{Z_I}{\omega^* H}\frac{dT^*}{dt}\right],$$

which implies that the rate of change of the near-inertial energy (first term), is balanced by the dissipation of that energy in the mixed layer (second term), and the flux of near-inertial energy $\Pi(H)$ to the ocean below the mixed layer (third term). If we assume that only wind at the inertial frequency is important, the near-inertial flux term reduces to

$$\Pi(H) = \mathbf{u} \cdot \boldsymbol{\tau}.$$

The near-inertial energy flux calculated prior to each dissipation rate at the location of that estimate is calculated using MERRA winds and the mixed-layer depth H from the corresponding Argo profile. For all subsequent analysis we select the mean near-inertial flux 50-60 days prior to each dissipation rate estimate as our measure of the near-inertial flux. The mean near-inertial flux is shown in Figure 4.2a.

4.4 Results

4.4.1 Estimated Dissipation Rate and Environmental Variables

Median dissipation rate finestructure estimates between 30-60°N are correlated with both the mean eddy kinetic energy as shown in Figure 4.1a and the near-inertial flux 50-60 days prior to the dissipation rate estimate (Figure 4.3a). The largest dissipation rates occur when both the eddy kinetic energy and the near-inertial flux is high, therefore processes involving both the mesoscale and the wind forcing are likely to be important for setting the dissipation rate on these large scales. The energetic western boundary current extensions roughly spatially coincide with mid-latitude storm tracks, however in this data eddy kinetic energy

and the near-inertial flux are not strongly correlated with one another as demonstrated by their joint probability density function (Figure 4.3c).

The eddy kinetic energy is correlated with the velocity of the nearest detected eddy (Figure 4.3d), indicating that patterns observed in one variable may be present in the other. Both large values of the eddy kinetic energy and the velocity of the nearest eddy are correlated with the dissipation rate (Figure 4.3b). For a given eddy velocity, increasing the eddy kinetic energy leads to an increase in the median dissipation rate, however the reverse is not obviously true for all values of the eddy kinetic energy.

4.4.2 Eddies and the Estimated Dissipation Rate

Profiles of the zonally-averaged median dissipation rate inferred from Argo profiles are shown in Figure 4.4 between 20-40° and 40-60° in both hemispheres. They are sorted according to proximity to a detected eddy and the velocity of that eddy. In this section, a designation of weak eddy velocity indicates velocities less than one standard deviation below the global median velocity, and strong eddy velocity is one standard deviation greater than the median. The median dissipation rate estimates are elevated when the closest eddy has a high velocity. For the majority of the profiles there is no significant difference between those that are close to or inside an eddy (within two radii from the eddy edge), and profiles that are composed of dissipation rate estimates between two radii from the eddy edge and 800 km away. This implies that processes present in the vicinity of a strong eddy may be important for elevating the dissipation rate on a global scale as opposed to only processes that occur inside or very close to a strong eddy.

The zonally-averaged median dissipation rates in the vicinity of strong eddies are typically a factor of 2-3 larger than in the vicinity of weaker eddies (Figure 4.5a). In the Northern Hemisphere this factor peaks around 400 m depth. Between 20-40°S there is also a local maximum around 400 m. In contrast, the ratio between strong/weak velocity eddies is fairly consistent for the 40-60°S profiles until the 2000 m limit of our measurements. The dissipation rate estimates are also elevated in the vicinity of eddies with strong vorticity, calculated by the eddy velocity over

the eddy diameter (Figure 4.5b). These results are consistent with the possibility that processes found in the vicinity of mesoscale features with strong velocity or strong vorticity are important for dictating the observed global correlation between eddy kinetic energy and the dissipation rate.

There is no detectable effect of the sign of the vorticity on the zonally-averaged dissipation rate estimates. Figure 4.5c shows profiles of the ratio between the median dissipation rate estimates inside anticyclonic vs cyclonic eddies, which all are approximately unity. This is an indication that the effects of the sign of the vorticity may not be important in the globally-average Argo-derived dissipation rate estimates. However, this does not preclude local importance of the sign of the vorticity on the dissipation rate in a regional area as models and theory suggest (e.g. *Young and Jelloul*, 1997; *Klein et al.*, 2004), or in particular mesoscale features (e.g. *Kunze*, 1995).

The positive correlation between the velocity of the closest eddy and the dissipation rate is apparent in both hemispheres between 300-500 m and 5° zonally-averaged bands between 20-60°, as shown in Figure 4.6. The relationship is stronger, leading to steeper slopes, in the Northern Hemisphere (Figure 4.6b), compared to the Southern Hemisphere (Figure 4.6a). This confirms that correlation between the estimated dissipation rate and the velocity of the nearest eddy is consistent throughout the mid-latitudes, and not is due to only one latitudinal band.

4.4.3 Seasonal Cycle in the Estimated Dissipation Rate

A seasonal cycle in the dissipation rate estimated from Argo profiles is shown in Figure 4.7 (a-d) for 30-60°N, and (e-h) for 30-60°S. In each hemisphere the seasonal cycle is apparent for areas less (a,b,e,f) and greater (c,d,g,h) than the local median eddy kinetic energy. Both hemispheres exhibit a seasonal cycle that reaches from the surface to at least 2000 m, the depth limit of the Argo profiles. The seasonal cycle in the dissipation rate between 300-500 m is correlated with the seasonal cycle in the near-inertial flux calculated from the slab model (Figures 4.7 (c,d,g,h)).

In low eddy kinetic regions the two hemispheres have distinctly different patterns in the seasonal cycle. In the Northern Hemisphere the maximum wintertime dissipation rate peak is close to the surface of the ocean, while in the Southern Hemisphere there is both a surface peak, and one deeper, at approximately 1000 m. The peak occurs at the same depth as the buoyancy frequency maximum (not shown). This is similar to one location west of Drake Passage in the Southern Ocean where elevated near-inertial waves were observed between 500-1000 m depth, corresponding to the bottom of the geostrophic shear (*Kilbourne and Girton*, 2015).

Figure 4.8 shows the seasonal cycle of the dissipation rate and the near-inertial flux in the Northern Hemisphere between 30-60°N over a nearly 10 year time period divided into areas of low, medium, and high eddy kinetic energy. The magnitude of seasonal cycle in the near-inertial flux for each of these eddy kinetic energy designations is very similar over the time series. This corroborates the lack of correlation between the near-inertial wind flux and the eddy kinetic energy seen in Figure 4.3c, suggesting that the different regions of eddy kinetic energy have similar mean near-inertial wind forcing. This is an indication that the elevation of the dissipation in areas of high eddy kinetic energy (Figure 4.8b) is due to different processes in the energetic mesoscale rather than the differences in wind forcing between the two areas. The amplitude of the oscillations in the seasonal cycle in areas of high average eddy kinetic energy is often larger than the amplitude of the seasonal cycle in areas of low average eddy kinetic energy. This difference in amplitude suggests that regions with a strong mesoscale may be modulating the seasonally variable near-inertial waves.

4.4.4 Eddies and Near-Inertial Flux

At midlatitudes there is both strong eddy activity and elevated storm activity, and thus larger near-inertial fluxes from the mixed layer into the ocean. Next we further detangle our thinking about the wind forcing and the mesoscale field by considering the median dissipation rate between 300-500 m and 30-60°N as a function of the near-inertial wind flux, eddy kinetic energy, and time from a

variety of different perspectives (Figure 4.9).

A seasonal cycle in the dissipation rate estimates is apparent for a range of eddy kinetic energy (Figure 4.9a), and near-inertial flux values (Figure 4.9c). The amplitude of the seasonal cycle is larger in areas of elevated eddy kinetic energy (Figure 4.9a), consistent with a larger amplitude seasonal cycle for regions of higher average eddy kinetic energy shown in Figure 4.8b. Similarly, the amplitude of the seasonal cycle is larger at locations with a larger near-inertial flux (Figure 4.9c). These two observations imply at least two possible explanations: (1) the strong mesoscale field is effecting the near-inertial waves, creating an elevated seasonal cycle, and (2) points with high near-inertial fluxes also have strong wind forcing nearby, thus the larger seasonal cycle is due to the horizontal propagation of near-inertial waves adding to the local input.

An indication that possibility (1) is correct, that an energetic eddy field may be important for dissipation near-inertial waves, is shown in Figure 4.9b. For high eddy kinetic energy, increasing the local near-inertial flux leads to an increase in the dissipation rate. However, for low eddy kinetic energy there is very little correlation between the two, suggesting that increasing the local near-inertial energy in a extremely quiescent ocean will have very little effect on the dissipation rate immediately below the event. This is shown in an alternative way in Figure 4.9d: there is no effect of wind forcing for low values of eddy kinetic energy, however for higher eddy kinetic energy increasing the wind forcing increases the dissipation rate.

4.5 Discussion

Dissipation rate estimates calculated by applying finestructure methods to Argo profiles are elevated in areas that typically have high eddy kinetic energy, and in regions of locally strong eddies. At some latitudes we observe that the ratio of dissipation rate estimates between 300-500 m near strong eddies as opposed to weak eddies can approach an order of magnitude, however it is typically elevated by a factor of 2-3. This is suggestive that something in addition to wind-triggered

internal waves is contributing to the elevated dissipation rate estimates that are associated with regions of stronger eddies and higher eddy kinetic energy.

Although not the entire story, wind forcing is also important for setting the dissipation rate. There is a seasonal cycle in the Argo-profile-derived dissipation rate estimates in the mid-latitudes in both hemispheres that extends down to at least 2000 m below the surface. This seasonal cycle is correlated with the local near-inertial flux of energy down from the mixed layer as calculated from a slab model. The magnitude of this seasonal cycle is elevated in regions that on average have high eddy-kinetic energy. Also, in places with high eddy kinetic energy increasing the near-inertial flux from the winds increases the dissipation, a relationship not found in areas close to weak eddies. This is consistent with the the idea that the mesoscale field facilitates dissipation of near-inertial energy from the winds.

4.5.1 Possible mechanisms responsible for EKE/dissipation rate correlation

These results can be placed into the context of the various processes that may be at play as presented in Section 4.1, and whether these processes are likely to have a large enough influence on the patterns in our dissipation rate estimates to generate the global correlation between eddy kinetic energy and the dissipation rate. As the other processes may still be important in specific contexts, or locally, we only make statements about whether they appear to dictate the global patterns of our measure of the dissipation rate.

One possibility is the spontaneous generation of internal waves from mesoscale features through a range of mechanisms (eg. *Vanneste*, 2013; *Griffiths and Reeder*, 1996; *Ford*, 1994). Generation is thought to be more likely for larger Rossby number features, corresponding to eddies of larger velocities. Once the internal waves are generated they might propagate away, creating an elevated wave field in the vicinity of the eddy, and possibly an elevated dissipation rate. Therefore we would expect a generally elevated internal wave field surrounding mesoscale features, and thus a subsequently elevated dissipation rate. This story is consistent with our observations that the dissipation rate is elevated near (as opposed to in-

side) eddies with stronger velocities and is generally elevated in areas of high eddy kinetic energy. Therefore the generation of near-inertial waves by the mesoscale is a viable explanation for the global correlation between eddy kinetic energy and the dissipation rate estimates that we observe.

The vorticity anomalies in the mesoscale may act to break up the large horizontal-scale near-inertial waves and cause them to disperse, causing the low modes to have faster propagation speeds (*Young and Jelloul*, 1997; *Klein et al.*, 2004; *Danioux et al.*, 2008). If we consider the velocity of the nearest eddy as a crude approximation for the strength of the local mesoscale vorticity field, then our results are consistent with this idea. Figure 4.5b explicitly shows that the estimated dissipation rate is elevated close to eddies of large vorticity, and the trends in the velocity results in Figures 4.4 and 4.6 also hold for the vorticity. This is also consistent with the idea that the largest near-inertial kinetic energy is related to the Laplacian of the vorticity field (*Klein et al.*, 2004) since we would expect a larger curvature of the vorticity field closer to large eddies.

These theories and modeling studies involving internal waves interacting with the vorticity of the mesoscale field typically involve near-inertial waves. If these mechanisms are globally important for dictating the dissipation rate we would expect the seasonal cycle in a stronger mesoscale field to be larger in amplitude, and the response to increasing the near inertial flux from the winds also to be larger. The observations presented do support this.

Previous work has suggested that near-inertial waves become trapped in anticyclonic structures and expelled from cyclonic ones (*Kunze*, 1995; *Klein et al.*, 2004; *Danioux et al.*, 2008). However we do not find this in our observations. The ratio between the dissipation rate profiles in cyclonic and anticyclonic eddies is close to 1 (Figure 4.5c), suggesting that this particular mechanism does not significantly influence the global correlation between eddy kinetic energy and the dissipation rate that we observe. Similarly, our observations do not reveal elevated dissipation at the eddy periphery, and therefore does not give evidence that critical layer processes on the sloping isopycnals at the edge of eddies is important for dictating the global correlation between eddy kinetic energy and the dissipation rate.

4.5.2 Caveats and Considerations

There are a number considerations involving the applicability of this finescale parameterization in the context of high eddy kinetic energy. Comparisons between finestructure estimates of the dissipation rate and microstructure measurement generally do find good agreement, within a factor of 2-3, when comparing average profiles (*Whalen et al.*, 2015). This comparison did include two areas with higher than average eddy kinetic energy, near the Hawaiian Ridge and over the Kerguelen Plateau, suggesting that this method is applicable in regions with an energetic mesoscale.

While the parameterization generally agrees with microstructure, there are possible problems specifically applying it to areas of high eddy kinetic energy or to near-inertial waves. The first is the potential for overestimating the dissipation rate due to interleaving. While this may contribute to the elevated dissipation rate estimates in energetic mesoscale regions it is unlikely it is responsible of the entire pattern because do to so (1) the interleaving would need to have a significant effect down to 2000 m, and (2) it would need to have a density signature, i.e. it could not be density compensated. Another possibility problem for the parameterization for these applications is that many of the theories involve near-inertial waves, which have large shear to strain ratios. Since we impose a constant shear-to-strain ratio we may be underestimating the dissipation rate due to the high shear content of the near-inertial waves.

Another curiosity is the lack of elevated dissipation rate estimates associated with anticyclonic eddies as opposed to cyclonic eddies. Microstructure measurements of the dissipation rate (*Padman et al.*, 1990; *Kunze*, 1995; *Sheen et al.*, 2015) show elevated dissipation below anticyclonic eddies. Also, an application of the finescale strain parameterization to one particular location near Hawaii shows an elevated dissipation rate below anticyclonic but not cyclonic eddies (*Jing and Wu*, 2013). However, *Jing and Wu* (2013) found an elevated dissipation rate of a factor of approximately only 1.5 beneath anticyclonic eddies, and this only occurred in their 300-600 m bin; they essentially found no difference in the 600-900 m range. This suggests that one possible explanation is that the effect of the sign of the

vorticity is relatively small, and it's placement in the vertical is a function of eddy depth, thus averaging over large areas may render this undetectable with the current dataset. Alternatively, there is observational evidence that the dissipation rate may be also enhanced near cyclonic eddies (*Meyer et al.*, 2015), suggesting that possibly additional processes cause dissipation in cyclonic eddies and ration between the two eddy signs may not show up in global averages.

4.6 Conclusions

Possible mechanisms were explored that could be underlying the previously observed correlation between the average eddy kinetic energy and the estimated dissipation rate from finestructure methods, leading to a series of results. First, zonally-averaged dissipation rate profiles from inside eddies are nearly identical to those taken outside of eddies, and we do not observe cyclonical to determine those profiles. This is an indication that mechanisms present only inside eddies, or those that are highly dependent on the local eddy's vorticity, do not significantly dictate the global correlation between eddy kinetic energy and the dissipation rate. Second, we find a seasonal cycle in the dissipation rate that extends as deep as our 2000 m measurements between 30-60° in both hemispheres. This seasonal cycle is clear for areas of both high and low eddy kinetic energy but exhibits different amplitudes in both hemispheres, and different spatial patterns in the Southern Hemisphere, suggesting that the mesoscale may influence the dissipation of near-inertial waves. Finally, we observe that in areas of high eddy kinetic energy there is a clear correlation between the near-inertial flux and the dissipation rate, which is not the case for areas of low eddy kinetic energy. This is also an indication that the mesoscale may be modulating the dissipation from wind-driven near-inertial waves.

4.7 Acknowledgments

This work was funded by NSF OCE-0927650 and OCE-1259573.

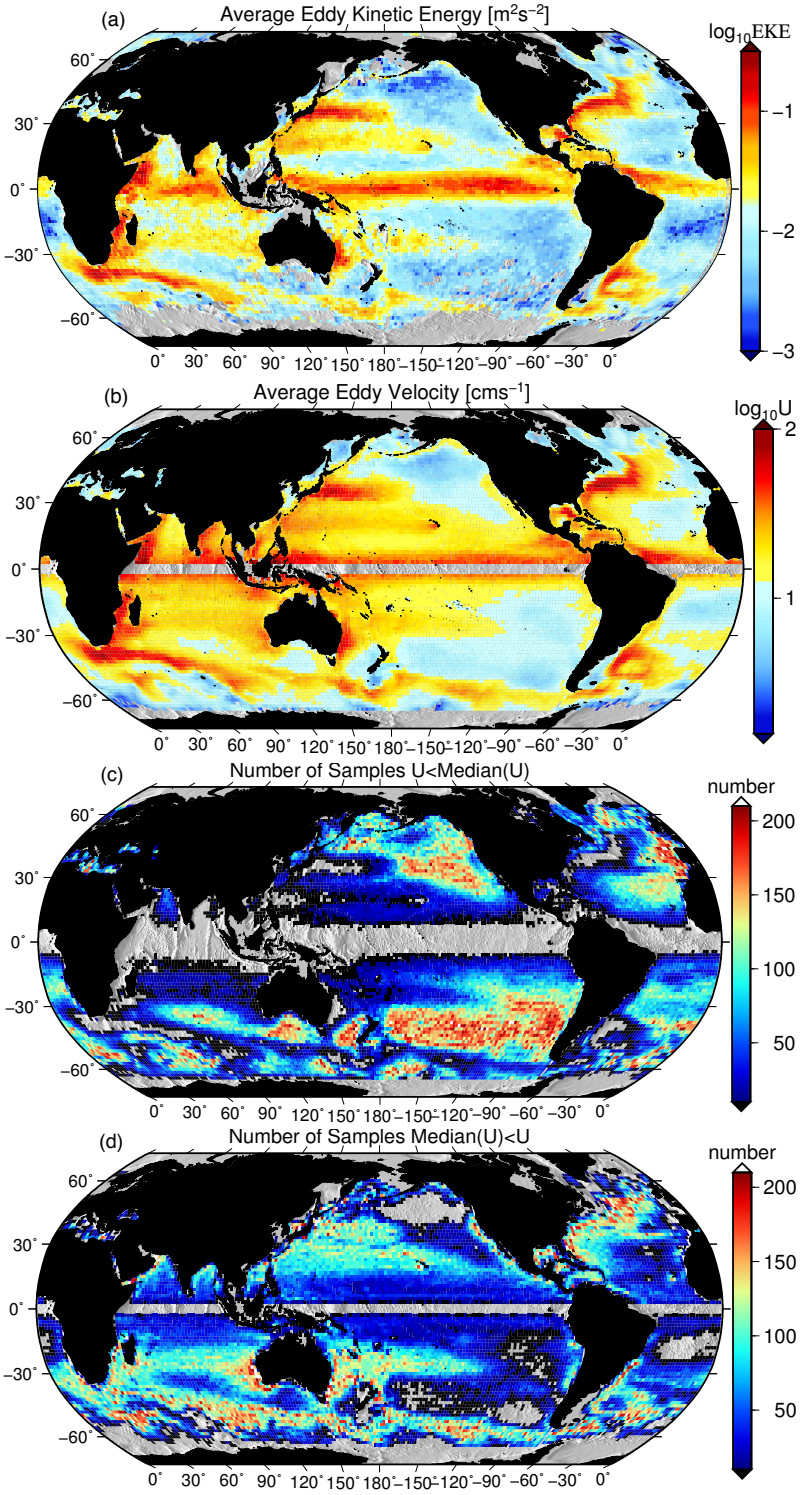

Figure 4.1: (a) The averaged eddy kinetic energy from surface drifters (Lumpkin, pers. comm.). (b) The median velocity of the eddies from a satellite-derived eddy product *Chelton et al.* (2011). The number of eddies detected that are (c) below and (d) above the median eddy velocity.

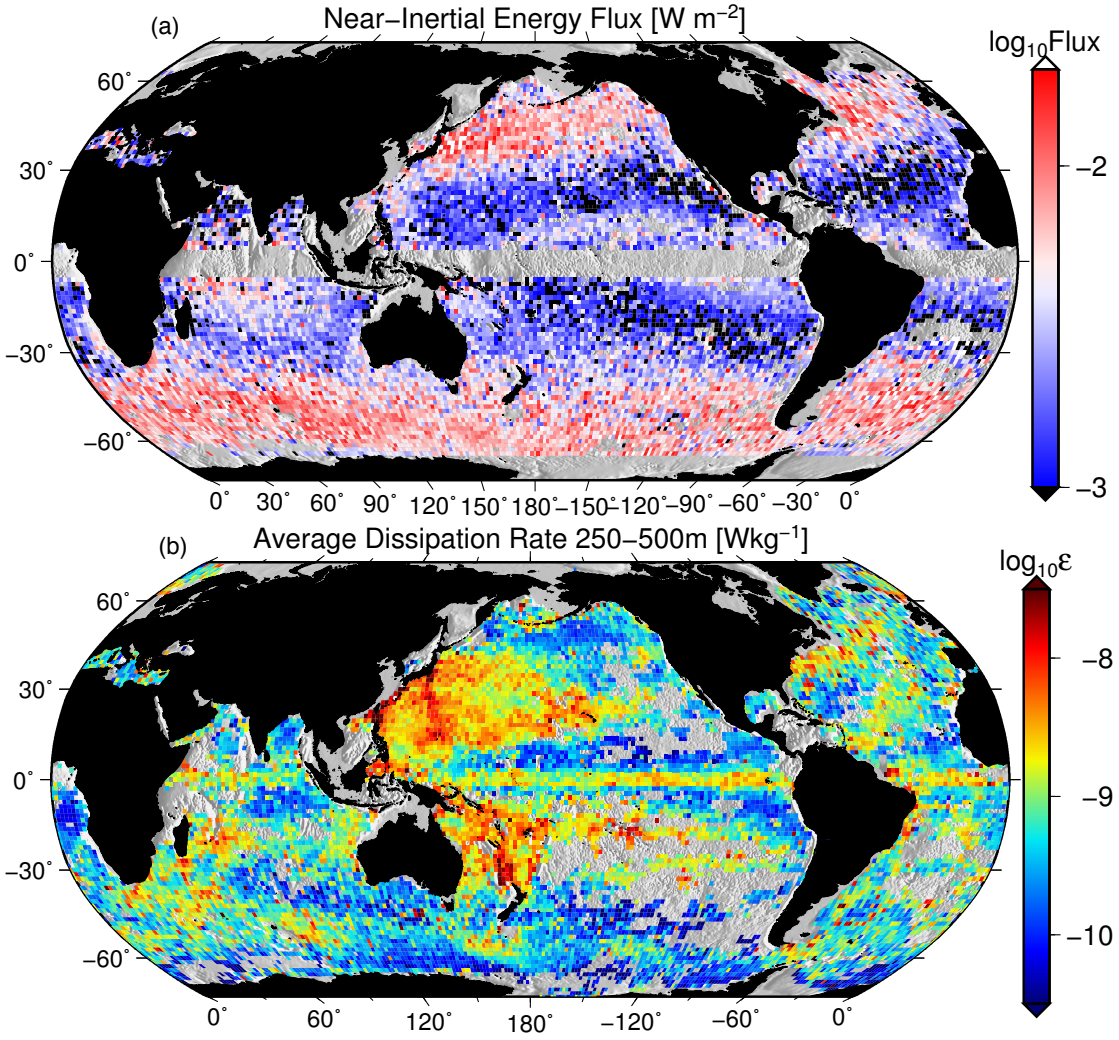

Figure 4.2: (a) The mean near-inertial flux derived from a slab model at the Argo dissipation rate estimate locations 50-60 days prior to the estimate. (b) The mean dissipation rate estimate calculated from Argo profiles using a finescale strain method. At least 3 estimates are required to plot a point.

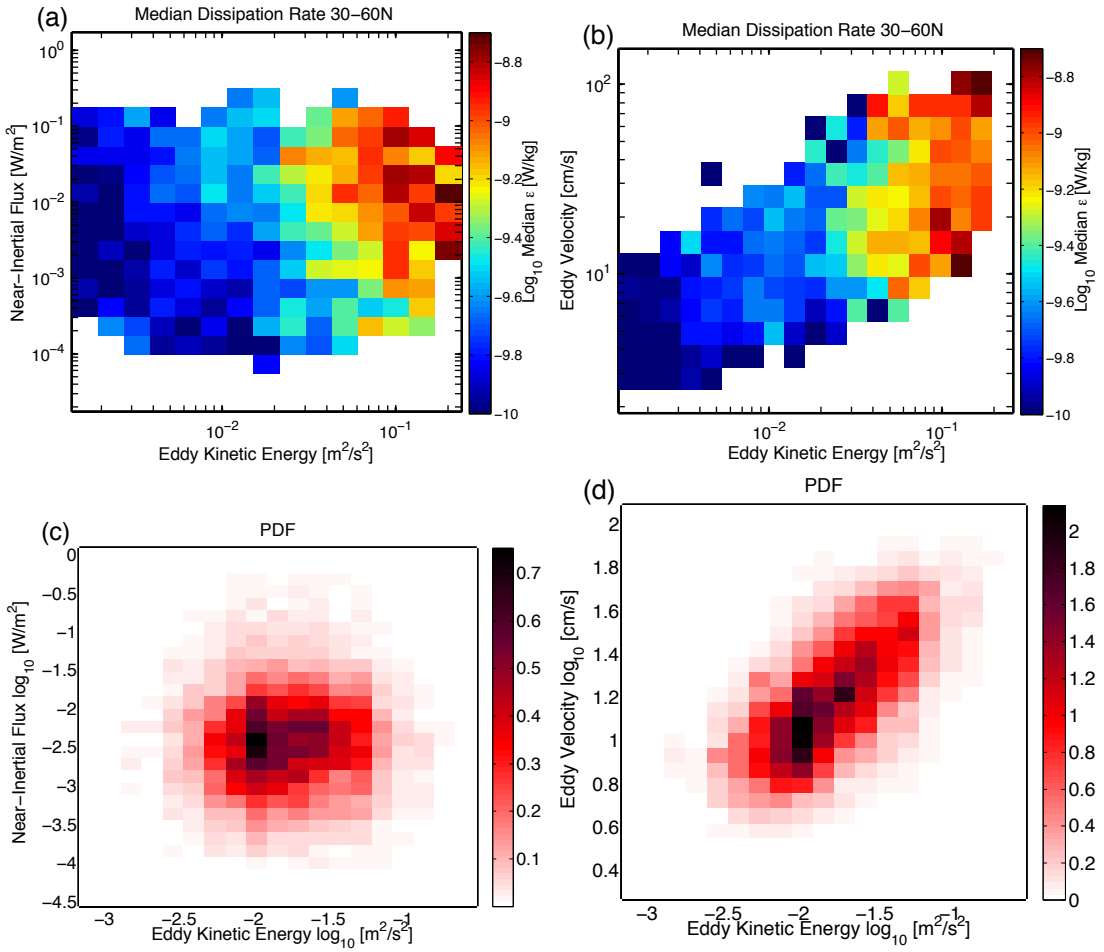

Figure 4.3: The median dissipation rate between 300-500 m and 30-60°N as calculated from Argo-profiles as a function of (a) eddy kinetic energy and the near-inertial flux, and (b) the eddy kinetic energy and the velocity of the closest eddy. Only medians with at least 10 dissipation estimates are included. Joint PDFs as a function of (c) the eddy velocity and near-inertial flux, and (d) the eddy kinetic energy and the velocity of the closest eddy between 30-60°N.

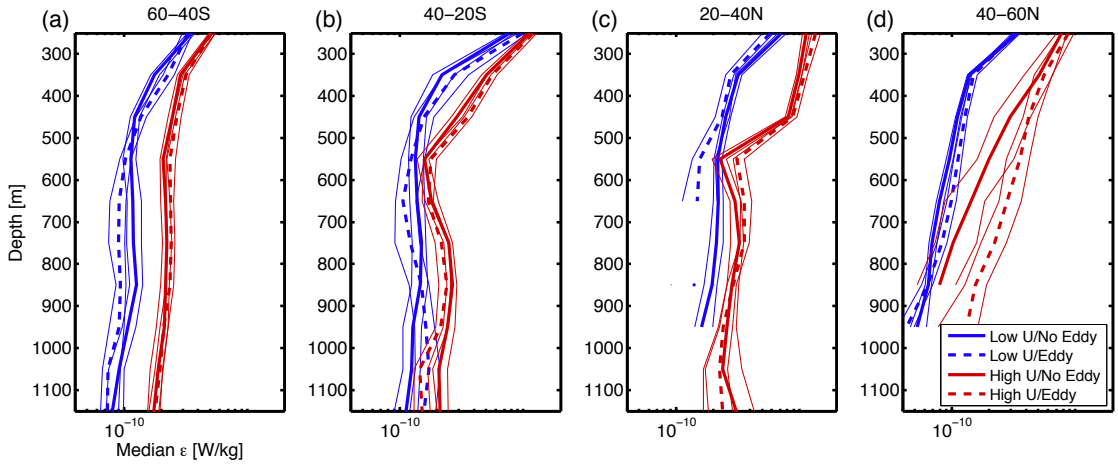

Figure 4.4: Zonally averaged median dissipation rate profiles closer than two radii from eddy (dashed), or further away (straight). Profiles are further divided between the closest eddy possessing a velocity one standard deviation greater than the global median (red), or less than the median (blue). The small lines are 90% bootstrapped confidence intervals and averages are only plotted if they contain at least 100 dissipation rate estimates.

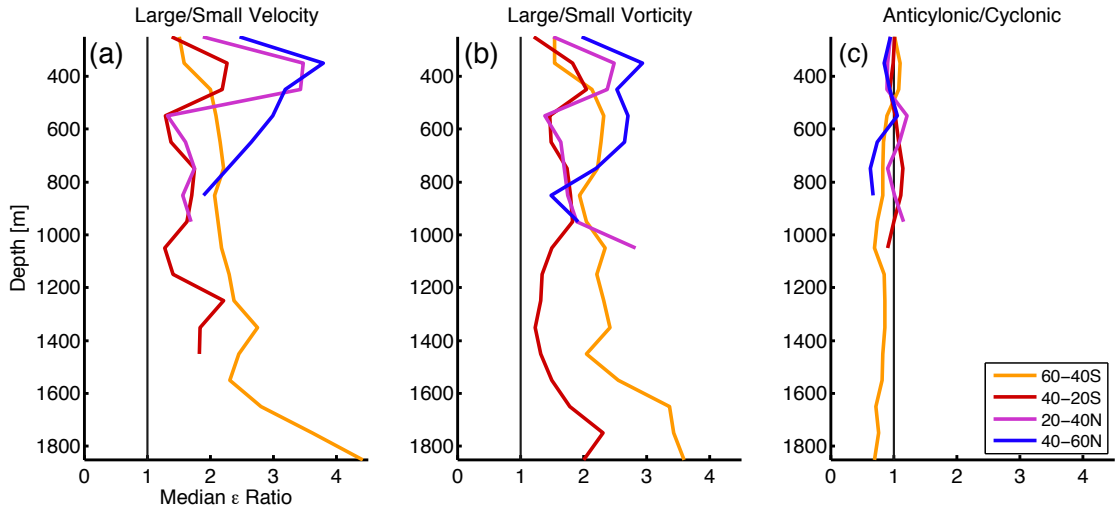

Figure 4.5: Zonally-averaged ratios between median dissipation rate profiles inferred from Argo for greater and less than one standard deviation from the median of (a) eddy velocity, and (b) eddy vorticity calculated by the eddy velocity defined by the eddy diameter. (c) The ratio between anticyclonic and cyclonic median dissipation rate profiles using data from within an eddy. At least 200 dissipation rate estimates are required to plot the ratio.

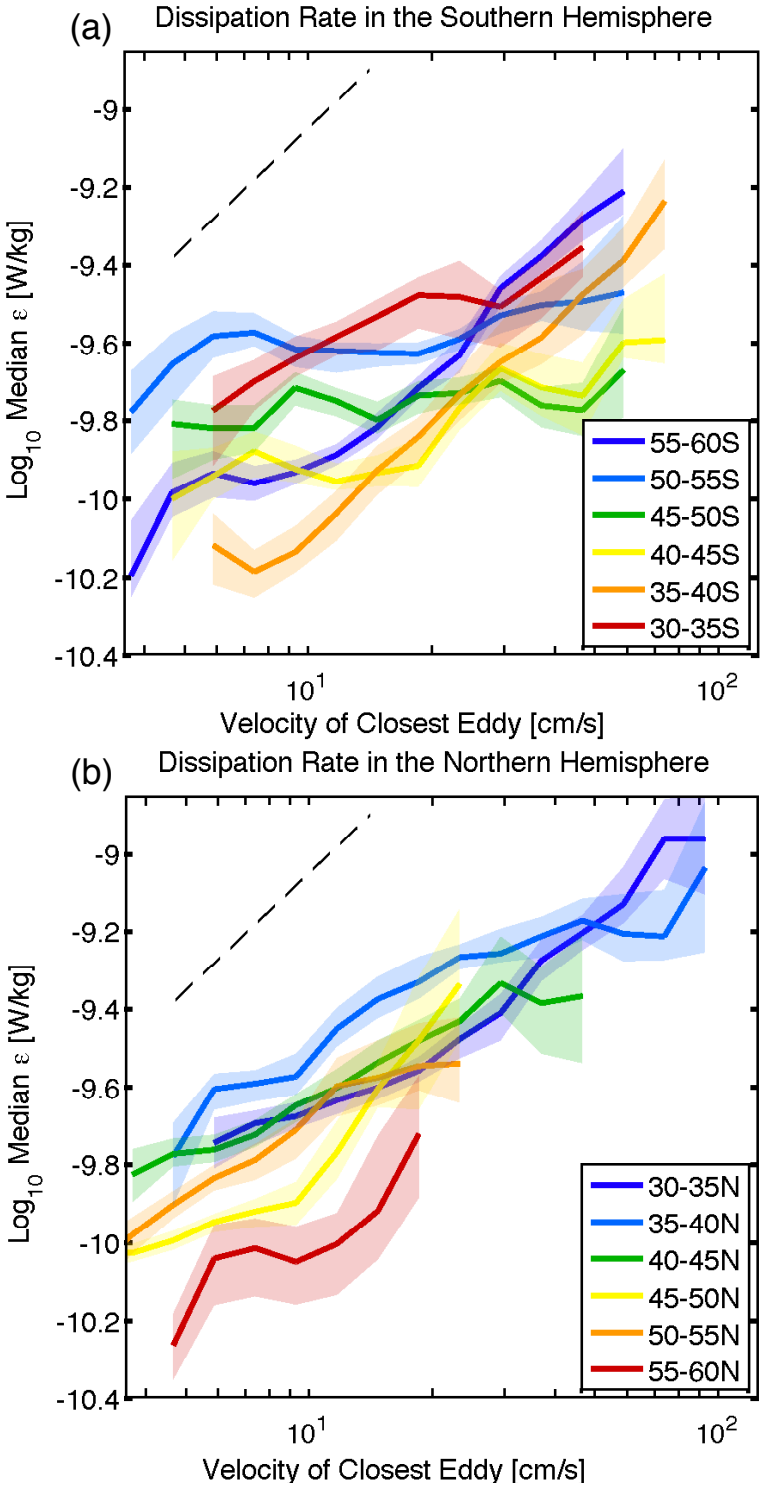

Figure 4.6: The median dissipation rate between 300-500 m as a function of the velocity of the closest eddy for latitudinal bands between (a) 30-60°S and (b) 30-60°N. A dashed line is placed for reference and indicates a slope of one in log-log space. At least 100 dissipation rate estimates are required to plot each median.

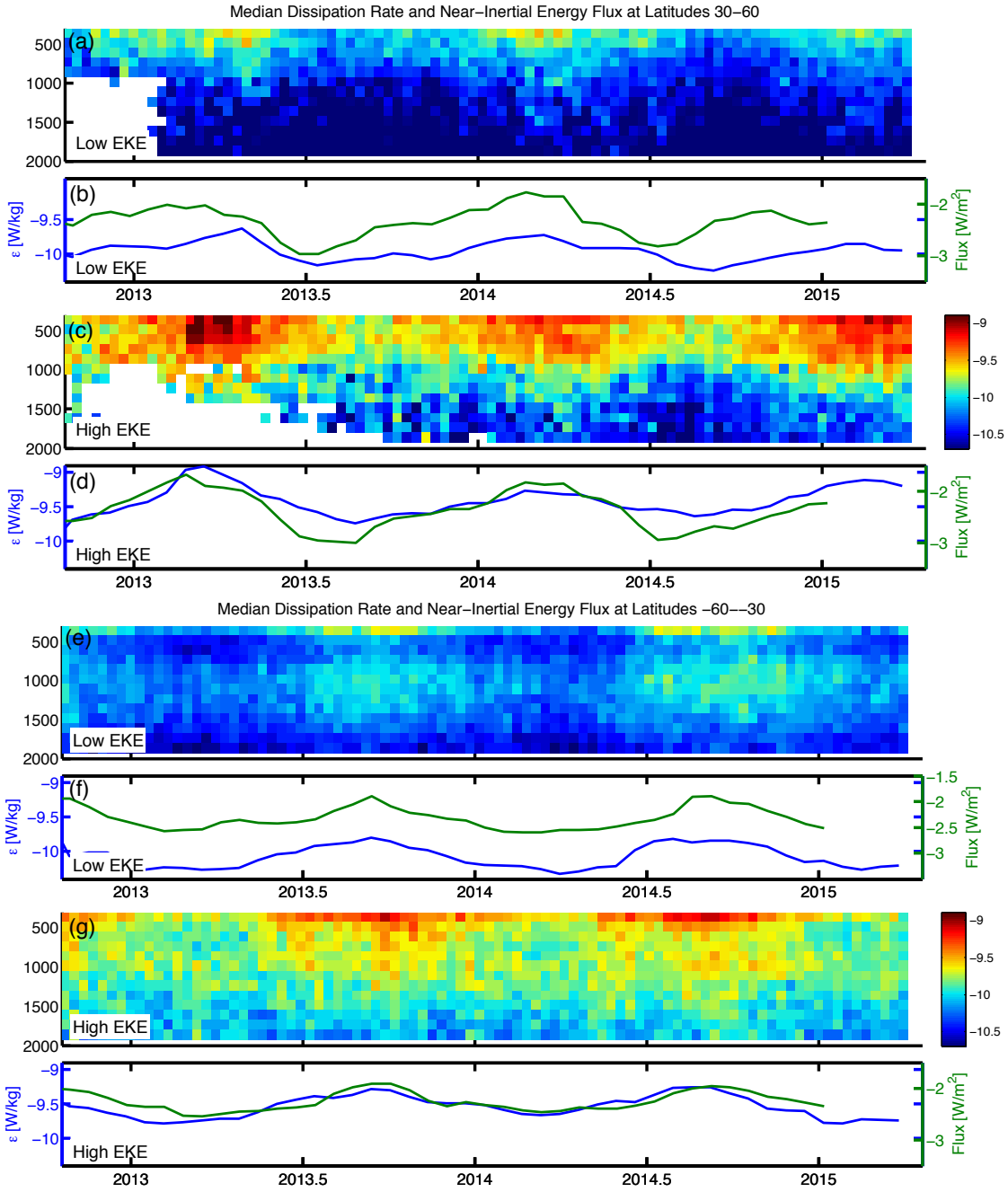

Figure 4.7: The seasonal cycle in the median dissipation rate between 30-60°N shown for a (a,b) high and (c,d) low eddy kinetic energy environment. The seasonal cycle is shown as a function of depth (a,c) and the average between 300-500 m is plotted along side the near-inertial energy flux derived from a slab model 50-60 days before the dissipation rate estimates (b,d). At least 10 dissipation rate estimates are required for averaging. (e-h) are identical to (a-d) except using data from Southern Hemisphere between 30-60°S.

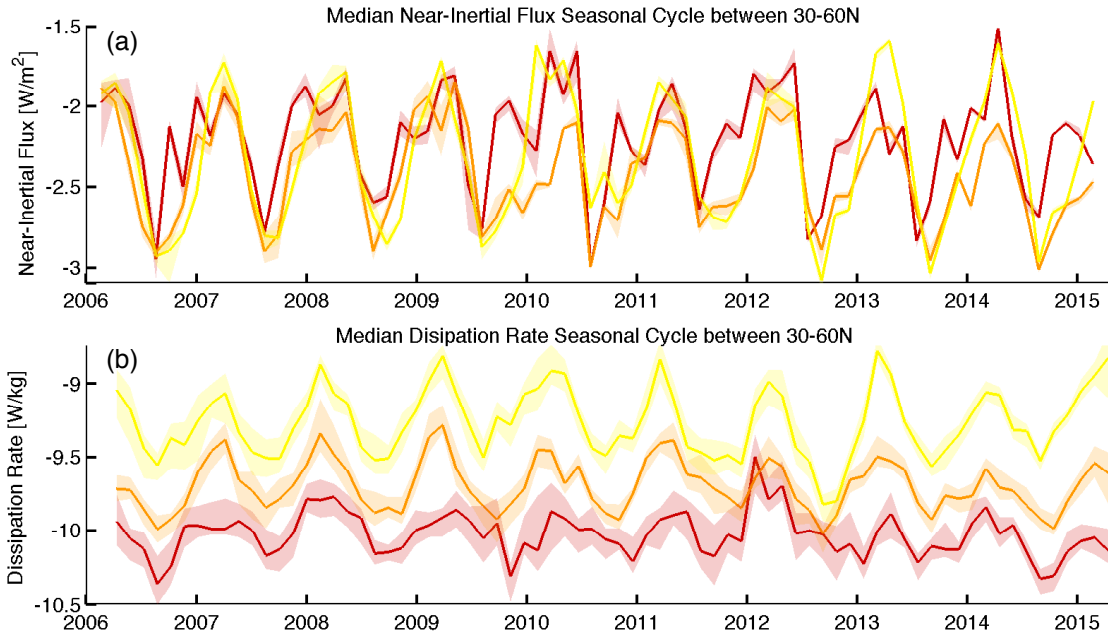

Figure 4.8: The seasonal cycle in (a) the dissipation rate and (b) the near-inertial flux from a slab model 50-60 days prior and at the corresponding locations. Colors denote regions of high (yellow), medium (orange), or low (red) eddy kinetic energy. Shaded areas represent 90% bootstrapped confidence intervals.

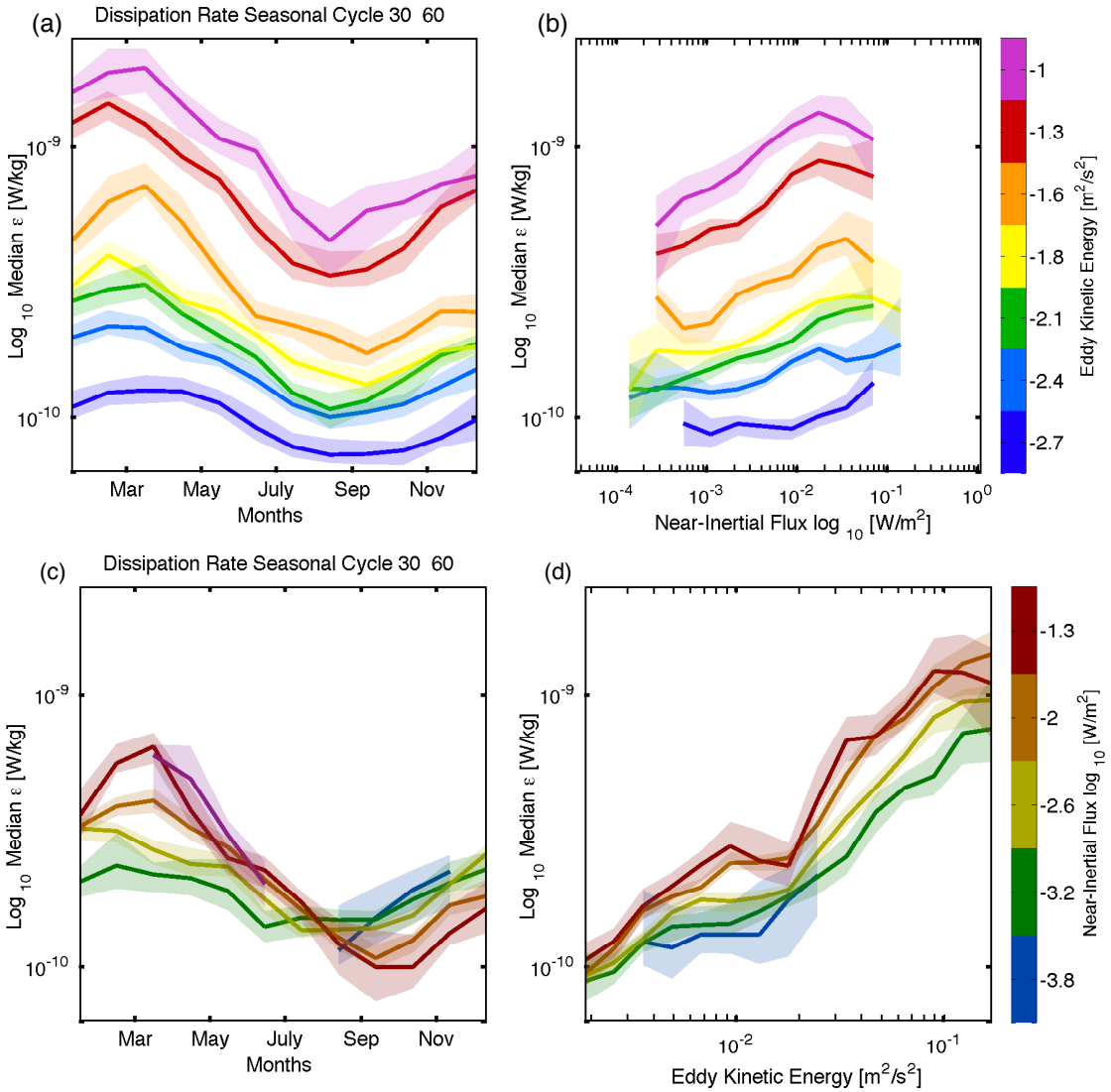

Figure 4.9: The median dissipation rate averaged between 30-60°N and 300-500 m. For (a,b) the colors indicate eddy kinetic energy values, and for (c,d) the colors show the average near-inertial energy flux down from the mixed layer calculated from a slab model between 50-60 days prior to the dissipation rate estimate. (a,c) show the seasonal cycle in the dissipation rate, (b) shows the dissipation rate as a function of near-inertial flux 50-60 days prior, and (d) is a function of the eddy kinetic energy. At least 100 dissipation rate estimates are required to plot each median. Shaded areas represent 90% bootstrapped confidence intervals.

Chapter 5

Conclusions

This work strives to illuminate the geographic patterns of the turbulent energy dissipation rate in the ocean, and possible mechanisms responsible for those patterns. To achieve this a finescale method was applied to Argo float profiles, an approach that we find to agree within a factor of 2-3 with measurements taken on smaller length scales using microstructure instruments.

Spatially, the dissipation rate varies by multiple orders of magnitude throughout the global ocean. The dissipation is correlated with a number of energy sources of internal waves, including the tidal kinetic energy and the near-inertial kinetic energy. A correlation is also found with seafloor roughness, consistent with a uneven seafloor scattering internal waves and dissipating their energy. The dissipation rate is also correlated with eddy kinetic energy, which is associated with an energetic mesoscale. Our observations suggest that this correlation with eddy kinetic energy is both consistent with the mesoscale acting as a source for inertial waves and facilitating their destruction.

Temporally we see a distinct seasonal cycle in the dissipation rate. This seasonal cycle is especially clear in the Northwest Pacific, likely due to the significant near-inertial wind forcing in that region. There also is a seasonal cycle in the dissipation rate extending down to the 2000 m limit of our measurements in both hemispheres between 30-60°, but no observed seasonal cycle in zonally-averaged profiles at lower latitudes. In regions of elevated eddy kinetic energy the amplitude of the seasonal cycle is larger, and the dissipation rate is elevated more when there

is strong near-inertial energy flux.

While a number of questions were addressed in this work, quite a few additional questions were uncovered in the process. A selection of those questions is included below to spark future research:

Eddy kinetic energy:

- What is causing the correlation between the dissipation rate and eddy kinetic energy that appears to be independent of the near-inertial wind forcing? Is it the generation of internal waves from mesoscale features or some other process?

- What are the dominate mechanisms in areas of high eddy kinetic energy that are causing a stronger response from the near-inertial winds?

- Are there limitations in applying finescale parameterizations in regions with strong eddies and large fronts?

Equatorial region:

- Are the Argo-float derived finescale estimates of equatorial diapycnal mixing consistent with microstructure measurements? If they differ, to what extent and under which circumstances?

- Can the locally elevated strain variance along the equator be linked to any of the large scale equatorial dynamics? Is strain variance beneath the equatorial undercurrent correlated with ENSO? Tropical instability waves?

- To what extent is the equatorially elevated strain variance simply related to enhanced eddy kinetic energy and hence to the same mechanisms that will be explored for regions of high eddy kinetic energy at other latitudes?

Further questions:

- Is energy dissipation rate that we observe consistent with the known energy input from tidal sources?

- What sets the geography of the mixing in the ocean deeper than what we can observe with 2000 m Argo profiles? Does the seasonal cycle in the dissipation rate extend to the seafloor?

Chapter 6

Bibliography

Alford, M., Cronin, M., and Klymak, J. (2012). Annual cycle and depth penetration of wind-generated near-inertial internal waves at Ocean Station Papa in the Northeast Pacific. *J. Phys. Oceanogr.*, 42(6):889–909.

Alford, M. H. (2010). Sustained, full-water-column observations of internal waves and mixing near Mendocino Escarpment. *J. Phys. Oceanogr.*, 40:2643–2660.

Alford, M. H. and Gregg, M. C. (2001). Near-inertial mixing: Modulation of shear, strain and microstructure at low latitude. *J. Geophys. Res.-Oceans*, 106:16947–16968.

Alford, M. H., MacKinnon, J. A., Nash, J. D., Simmons, H., Pickering, A., and Klymak, J. M. e. a. (2011). Energy flux and dissipation in Luzon Strait: Two tales of two ridges. *J. Phys. Oceanogr.*

Alford, M. H., Shcherbina, A. Y., and Gregg, M. C. (2013). Observations of near-inertial internal gravity waves radiating from a frontal jet. *J. Phys. Oceanogr.*, 43(6):1225–1239.

Alford, M. H. and Whitmont, M. (2007). Seasonal and spatial variability of near-inertial kinetic energy from historical moored velocity records. *J. Phys. Oceanogr.*, 37(8):2022–2037.

Bell, T. (1975). Topographically generated internal waves in the open ocean. *J. Geophys. Res.*, 80(3):320–327.

Bray, N. A. and Fofonoff, N. P. (1981). Available potential-energy for mode eddies. *J. Phys. Oceanogr.*, 11(1):30–47.

Bühler, O. and McIntyre, M. E. (2005). Wave capture and wave–vortex duality. *J. Fluid Mech.*, 534:67–95.

Cairns, J. L. and Williams, G. O. (1976). Internal wave observations from a midwater float, 2. *J. Geophys. Res.*, 81(12):1943–1950.

Chaigneau, A., Pizarro, O., and Rojas, W. (2008). Global climatology of near-inertial current characteristics from Lagrangian observations. *Geophys. Res. Lett.*, 35.

Chelton, D. B., Schlax, M. G., and Samelson, R. M. (2011). Global observations of nonlinear mesoscale eddies. *Prog. Oceanogr.*, 91(2):167–216.

Danioux, E., Klein, P., and Rivière, P. (2008). Propagation of wind energy into the deep ocean through a fully turbulent mesoscale eddy field. *J. Phys. Oceanogr.*, 38(10):2224–2241.

Danioux, E., Vanneste, J., Klein, P., and Sasaki, H. (2012). Spontaneous inertia-gravity-wave generation by surface-intensified turbulence. *J. Fluid Mech.*, 699:153–173.

D'Asaro, E. A. (1985). The energy flux from the wind to near-inertial motions in the surface mixed layer. *J. Phys. Oceanogr.*, 15(8):1043–1059.

D'Asaro, E. A., Eriksen, C. C., Levine, M. D., Niiler, P., Paulson, C. A., and Vanmeurs, P. (1995). Upper-ocean inertial currents forced by a strong storm. I: Data and comparisons with linear-theory. *J. Phys. Oceanogr.*, 25:2909–2936.

de Boyer Montegut, C., Madec, G., Fischer, A. S., Lazar, A., and Iudicone, D. (2004). Mixed layer depth over the global ocean: An examination of profile data and a profile-based climatology. *J. Geophys. Res.-Oceans*, 109(C12).

Decloedt, T. and Luther, D. S. (2010). On a simple empirical parameterization of topography-catalyzed diapycnal mixing in the abyssal ocean. *J. Phys. Oceanogr.*, 40:487–508.

Desaubies, Y. and Gregg, M. C. (1981). Reversible and irreversible fine-structure. *J. Phys. Oceanogr.*, 11(4):541–556.

Egbert, G. D. and Ray, R. D. (2003). Semi-diurnal and diurnal tidal dissipation from TOPEX/Poseidon altimetry. *Geophys. Res. Lett.*, 30.

Ferrari, R. and Wunsch, C. (2008). Ocean circulation kinetic energy: Reservoirs, sources, and sinks. *Ann. Rev. Fluid Mech.*, 41(1):253.

Ferrari, R. and Wunsch, C. (2010). The distribution of eddy kinetic and potential energies in the global ocean. *Tellus Series a-Dynamic Meteorology and Oceanography*, 62(2):92–108.

Ford, R. (1994). Gravity wave radiation from vortex trains in rotating shallow water. *J. Fluid Mech.*, 281:81–118.

Frants, M., Damerell, G. M., Gille, S. T., Heywood, K. J., MacKinnon, J., and Sprintall, J. (2013). An Assessment of Density-Based Finescale Methods for Estimating Diapycnal Diffusivity in the Southern Ocean. *J. Atmos. Oceanic Technol.*, 30(11):2647–2661.

Fu, L.-L. (1981). Observations and models of inertial waves in the deep ocean. *Rev. Geophys.*, 19(1):141–170.

Gargett, A. E. (1990). Do we really know how to scale the turbulent kinetic-energy dissipation-rate-epsilon due to breaking of oceanic internal waves? *J. Geophys. Res.-Oceans*, 95(C9):15971–15974.

Gregg, M. and Kunze, E. (1991). Shear and strain in Santa Monica basin. *J. Geophys. Res.-Oceans*, 96(C9):16709–16719.

Gregg, M. C. (1989). Scaling turbulent dissipation in the thermocline. *J. Geophys. Res.-Oceans*, 94:9686–9698.

Gregg, M. C., Sanford, T. B., and Winkel, D. P. (2003). Reduced mixing from the breaking of internal waves in equatorial waters. *Nature*, 422:513–515.

Gregg, M. C., Seim, H. E., and Percival, D. B. (1993). Statistics of shear and turbulent dissipation profiles in random internal wave-fields. *J. Phys. Oceanogr.*, 23(8):1777–1799.

Griffiths, M. and Reeder, M. J. (1996). Stratospheric inertia–gravity waves generated in a numerical model of frontogenesis. I: Model solutions. *Q. J. Roy. Meteor. Soc.*, 122(533):1153–1174.

Harrison, M. J. and Hallberg, R. W. (2008). Pacific subtropical cell response to reduced equatorial dissipation. *J. Phys. Oceanogr.*, 38:1894–1912.

Hennon, T. D., Riser, S. C., and Alford, M. H. (2014). Observations of Internal Gravity Waves by Argo Floats. *J. Phys. Oceanogr.*, 44(9):2370–2386.

Henyey, F. (1991). Dynamics of Internal Gravity Waves in the Ocean: Proceedings, Aha Hulikoa Hawaiian Winter Workshop. SOEST, Univ. Hawaii.

Henyey, F. S. and Pomphrey, N. (1983). Eikonal description of internal wave interactions - a non-diffusive picture of induced diffusion. *Dyn. Atmos. Oceans*, 7(4):189–219.

Henyey, F. S., Wright, J., and Flatte, S. M. (1986). Energy and action flow through the internal wave feild - an eikonal approach. *J. Geophys. Res.-Oceans*, 91(C7):8487–8495.

Hibiya, T., Furuichi, N., and Robertson, R. (2012). Assessment of fine-scale parameterizations of turbulent dissipation rates near mixing hotspots in the deep ocean. *Geophys. Res. Lett.*, 39:6.

Huussen, T. N., Naveira-Garabato, A. C., Bryden, H. L., and McDonagh, E. L. (2012). Is the deep Indian Ocean MOC sustained by breaking internal waves? *J. Geophys. Res.-Oceans*, 117:18.

Inoue, R., Gregg, M. C., and Harcourt, R. R. (2010). Mixing rates across the Gulf Stream, Part 1: On the formation of Eighteen Degree Water. *J. Mar. Res.*, 68(5):643–671.

Jing, Z. and Wu, L. (2013). Low-frequency modulation of turbulent diapycnal mixing by anticyclonic eddies inferred from the HOT time series. *J. Phys. Oceanogr.*, 43(4):824–835.

Johnson, G. C., Kunze, E., McTaggart, K. E., and Moore, D. W. (2002). Temporal and spatial structure of the equatorial deep jets in the Pacific Ocean. *J. Phys. Oceanogr.*, 32(12):3396–3407.

Johnston, T. M. S., Merrifield, M. A., and Holloway, P. E. (2003). Internal tide scattering at the Line Islands Ridge. *J. Geophys. Res.-Oceans*, 108.

Joyce, T., Toole, J., Klein, P., and Thomas, L. (2013). A Near-Inertial Mode observed within a Gulf Stream Warm-Core Ring. *J. Geophys. Res.*

Kilbourne, B. F. and Girton, J. B. (2015). Quantifying High-Frequency Wind Energy Flux into Near-Inertial Motions in the Southeast Pacific. *J. Phys. Oceanogr.*, 45(2):369–386.

Klein, P., Smith, S. L., and Lapeyre, G. (2004). Organization of near-inertial energy by an eddy field. *Q. J. Roy. Meteor. Soc.*, 130(598):1153–1166.

Klymak, J. M., Moum, J. N., Nash, J. D., Kunze, E., Girton, J. B., Carter, G. S., Lee, C. M., Sanford, T. B., and Gregg, M. C. (2006). An estimate of tidal energy lost to turbulence at the Hawaiian Ridge. *J. Phys. Oceanogr.*, 36(6):1148–1164.

Klymak, J. M., Pinkel, R., and Rainville, L. (2008). Direct breaking of the internal tide near topography: Kaena ridge, Hawaii. *J. Phys. Oceanogr.*, 38:380–399.

Kunze, E. (1985). Near-inertial wave-propagation in geostrophic shear. *J. Phys. Oceanogr.*, 15(5):544–565.

Kunze, E. (1995). The energy-balance in a warm-core rings near-inertial critical layer. *J. Phys. Oceanogr.*, 25:942–957.

Kunze, E., Firing, E., Hummon, J. M., Chereskin, T. K., and Thurnherr, A. M. (2006). Global abyssal mixing inferred from lowered ADCP shear and CTD strain profiles. *J. Phys. Oceanogr.*, 36(8):1553–1576.

Kunze, E., Rosenfeld, L. K., Carter, G. S., and Gregg, M. C. (2002). Internal waves in Monterey Submarine Canyon. *J. Phys. Oceanogr.*, 32(6):1890–1913.

Kunze, E. and Sanford, T. B. (1984). Observations of near-inertial waves in a front. *J. Phys. Oceanogr.*, 14(3):566–581.

Ledwell, J. R., Montgomery, E. T., Polzin, K. L., St Laurent, L. C., Schmitt, R. W., and Toole, J. M. (2000). Evidence for enhanced mixing over rough topography in the abyssal ocean. *Nature*, 403(6766):179–182.

Ledwell, J. R., St Laurent, L. C., Girton, J. B., and Toole, J. M. (2011). Diapycnal mixing in the Antarctic Circumpolar Current. *J. Phys. Oceanogr.*, 41:241–246.

Lee, C. M., Kunze, E., Sanford, T. B., Nash, J. D., Merrifield, M. A., and Holloway, P. E. (2006). Internal tides and turbulence along the 3000-m isobath of the Hawaiian Ridge. *J. Phys. Oceanogr.*, 36(6):1165–1183.

Lee, D.-K. and Niiler, P. P. (1998). The inertial chimney: The near-inertial energy drainage from the ocean surface to the deep layer. *J. Geophys. Res.-Oceans*, 103(C4):7579–7591.

Liang, X. and Thurnherr, A. M. (2012). Eddy-modulated internal waves and mixing on a midocean ridge. *J. Phys. Oceanogr.*, 42(7):1242–1248.

Lumpkin, R. and Garraffo, Z. (2005). Evaluating the decomposition of tropical Atlantic drifter observations. *J. Atmos. Oceanic Technol.*, 22:1403–1415.

MacKinnon, J. A. and Gregg, M. C. (2003). Mixing on the late-summer New England shelf - Solibores, shear, and stratification. *J. Phys. Oceanogr.*, 33(7):1476–1492.

Mauritzen, C., Polzin, K. L., McCartney, M. S., Millard, R. C., and West-Mack, D. E. (2002). Evidence in hydrography and density fine structure for enhanced vertical mixing over the Mid-Atlantic Ridge in the western Atlantic. *J. Geophys. Res.-Oceans*, 107.

Meyer, A., Sloyan, B. M., Polzin, K. L., Phillips, H. E., and Bindoff, N. L. (2015). Mixing variability in the Southern Ocean. *J. Phys. Oceanogr.*, 45(4):966–987.

Molemaker, M. J., McWilliams, J. C., and Yavneh, I. (2005). Baroclinic instability and loss of balance. *J. Phys. Oceanogr.*, 35(9):1505–1517.

Moum, J. N., Lien, R. C., Perlin, A., Nash, J. D., Gregg, M. C., and Wiles, P. J. (2009). Sea surface cooling at the Equator by subsurface mixing in tropical instability waves. *Nature Geosci.*, 2(11):761–765.

Muller, P., Holloway, G., Henyey, F., and Pomphrey, N. (1986). Nonlinear-interactions among internal gravity-waves. *Rev. Geophys.*, 24(3):493–536.

Nikurashin, M. and Ferrari, R. (2010). Radiation and dissipation of internal waves generated by geostrophic motions impinging on small-scale topography: Theory. *J. Phys. Oceanogr.*, 40:1055–1074.

Nikurashin, M. and Ferrari, R. (2011). Global energy conversion rate from geostrophic flows into internal lee waves in the deep ocean. *Geophys. Res. Lett.*, 38.

Osborn, T. R. (1980). Estimates of the local-rate of vertical diffusion from dissipation measurements. *J. Phys. Oceanogr.*, 10:83–89.

Padman, L., Levine, M., Dillon, T., Morison, J., and Pinkel, R. (1990). Hydrography and microstructure of an Arctic Cyclonic Eddy. *J. Geophys. Res.-Oceans*, 95:9411–9420.

Pinkel, R. and Anderson, S. (1992). Toward a statistical description of finescale strain in the thermocline. *J. Phys. Oceanogr.*, 22(7):773–795.

Pinkel, R. and Anderson, S. (1997). Shear, strain, and Richardson number variations in the thermocline. Part I: statistical description. *J. Phys. Oceanogr.*, 27(2):264–281.

Pinkel, R., Sherman, J., Smith, J., and Anderson, S. (1991). Strain: Observations of the vertical gradient of isopycnal vertical displacement. *J. Phys. Oceanogr.*, 21(4):527–540.

Plueddemann, A. and Farrar, J. (2006). Observations and models of the energy flux from the wind to mixed-layer inertial currents. *Deep-Sea Res. II*, 53(1):5–30.

Pollard, R. T. and Millard, R. C. (1970). Comparison between observed and simulated wind-generated inertial oscillations. In *Deep Sea Research and Oceanographic Abstracts*, volume 17, pages 813–821. Elsevier.

Polzin, K. (1996). Statistics of the Richardson number: Mixing models and finestructure. *J. Phys. Oceanogr.*, 26(8):1409–1425.

Polzin, K. and Ferrari, R. (2004). Isopycnal dispersion in NATRE. *J. Phys. Oceanogr.*, 34(1):247–257.

Polzin, K. L. (2008). Mesoscale Eddy-Internal Wave Coupling. Part I: Symmetry, Wave Capture, and Results from the Mid-Ocean Dynamics Experiment. *J. Phys. Oceanogr.*, 38(11):2556–2574.

Polzin, K. L. (2010). Mesoscale Eddy-Internal Wave Coupling. Part II: Energetics and Results from PolyMode. *J. Phys. Oceanogr.*, 40(4):789–801.

Polzin, K. L. and Lvov, Y. V. (2011). Toward regional characterizations of the oceanic internal wavefield. *Rev. Geophys.*, 49(4).

Polzin, K. L., Naveira Garabato, A. C., Huussen, T. N., Sloyan, B. M., and Waterman, S. N. (2014). Finescale parameterizations of turbulent dissipation. *J. Geophys. Res.-Oceans*, 119.

Polzin, K. L., Toole, J. M., Ledwell, J. R., and Schmitt, R. W. (1997). Spatial variability of turbulent mixing in the abyssal ocean. *Science*, 276:93–96.

Polzin, K. L., Toole, J. M., and Schmitt, R. W. (1995). Finescale parameterizations of turbulent dissipation. *J. Phys. Oceanogr.*, 25:306–328.

Rainville, L. and Pinkel, R. (2004). Observations of energetic high-wavenumber internal waves in the Kuroshio. *J. Phys. Oceanogr.*, 34(7):1495–1505.

Reeder, M. J. and Griffiths, M. (1996). Stratospheric inertia–gravity waves generated in a numerical model of frontogenesis. II: Wave sources, generation mechanisms and momentum fluxes. *Q. J. Roy. Meteor. Soc.*, 122(533):1175–1195.

Rossby, C. (1937). On the mutual adjustment of pressure and velocity distributions in certain simple current systems. *J. Mar. Res*, 1(19):280.

Rudnick, D. L., Boyd, T. J., Brainard, R. E., Carter, G. S., Egbert, G. D., Gregg, M. C., Holloway, P. E., Klymak, J. M., Kunze, E., Lee, C. M., Levine, M. D., Luther, D. S., Martin, J. P., Merrifield, M. A., Moum, J. N., Nash, J. D., Pinkel, R., Rainville, L., and Sanford, T. B. (2003). From tides to mixing along the Hawaiian ridge. *Science*, 301(5631):355–357.

Schmitt, R. W. (1994). Double diffusion in oceanography. *Ann. Rev. Fluid Mech.*, 26(1):255–285.

Schmitt, R. W. (2003). Observational and laboratory insights into salt finger convection. *Prog. Oceanogr.*, 56(3-4):419–433.

Shcherbina, A. Y., Talley, L. D., Firing, E., and Hacker, P. (2003). Near-surface frontal zone trapping and deep upward propagation of internal wave energy in the Japan/East Sea. *J. Phys. Oceanogr.*, 33(4):900–912.

Sheen, K., Brearley, J., Naveira Garabato, A., Smeed, D., Laurent, L. S., Meredith, M., Thurnherr, A., and Waterman, S. (2015). Modification of turbulent dissipation rates by a deep Southern Ocean eddy. *Geophys. Res. Lett.*

Sheen, K., Garabato, A. N., Brearley, J., Meredith, M., Polzin, K., Smeed, D., Forryan, A., King, B., Sallée, J., Laurent, L. S., et al. (2014). Eddy-induced variability in Southern Ocean abyssal mixing on climatic timescales. *Nature Geosci.*, 7:577582.

Silverthorne, K. E. and Toole, J. M. (2009). Seasonal kinetic energy variability of near-inertial motions. *J. Phys. Oceanogr.*, 39(4):1035–1049.

Simmons, H. L. and Alford, M. H. (2012). Simulating the long-range swell of internal waves generated by ocean storms. *Oceanography*, 25(2):30–41.

Smith, W. H. F. and Sandwell, D. T. (1997). Global sea floor topography from satellite altimetry and ship depth soundings. *Science*, 277:1956–1962.

Sokolov, S. and Rintoul, S. R. (2009). Circumpolar structure and distribution of the Antarctic Circumpolar Current fronts: 2. Variability and relationship to sea surface height. *J. Geophys. Res.-Oceans*, 114(C11).

St Laurent, L. and Garrett, C. (2002). The role of internal tides in mixing the deep ocean. *J. Phys. Oceanogr.*, 32:2882–2899.

St Laurent, L. C., Simmons, H. L., and Jayne, S. R. (2002). Estimating tidally driven mixing in the deep ocean. *Geophys. Res. Lett.*, 29.

St Laurent, L. C., Toole, J. M., and Schmitt, R. W. (2001). Buoyancy forcing by turbulence above rough topography in the abyssal Brazil Basin. *J. Phys. Oceanogr.*, 31(12):3476–3495.

Thompson, A. F., Gille, S. T., MacKinnon, J. A., and Sprintall, J. (2007). Spatial and temporal patterns of small-scale mixing in Drake Passage. *J. Phys. Oceanogr.*, 37:572–592.

Thorpe, S. A. (1977). Turbulence and mixing in a Scottish Loch. *Philos. Trans. R. Soc. Lond., A*, 286(1334):125–181.

Thurnherr, A. M. and St Laurent, L. C. (2011). Turbulence and diapycnal mixing over the East Pacific Rise crest near 10 degrees N. *Geophys. Res. Lett.*, 38:4.

Toole, J. M., Polzin, K. L., and Schmitt, R. W. (1994). Estimates of diapycnal mixing in the abyssal ocean. *Science*, 264(5162):1120–1123.

Vanneste, J. (2013). Balance and spontaneous wave generation in geophysical flows. *Ann. Rev. Fluid Mech.*

Waterhouse, A. F., MacKinnon, J. A., Nash, J. D., Alford, M. H., Kunze, E., Simmons, H. L., Polzin, K. L., Laurent, L. C. S., Sun, O., Pinkel, R., et al. (2014). Global patterns of diapycnal mixing from measurements of the turbulent dissipation rate. *J. Phys. Oceanogr.*

Waterman, S., Garabato, A. C. N., and Polzin, K. L. (2013). Internal Waves and Turbulence in the Antarctic Circumpolar Current. *J. Phys. Oceanogr.*, 43(2):259–282.

Waterman, S., Polzin, K. L., Naveira Garabato, A. C., Sheen, K. L., and Forryan, A. (2014). Suppression of internal wave breaking in the Antarctic Circumpolar Current near topography. *J. Phys. Oceanogr.*, 44.

Whalen, C. B., MacKinnon, J. A., Talley, L. D., and Waterhouse, A. F. (2015). Estimating the Mean Diapycnal Mixing Using a Finescale Strain Parameterization. *J. Phys. Oceanogr.*, 45(4):1174–1188.

Whalen, C. B., Talley, L. D., and MacKinnon, J. A. (2012). Spatial and temporal variability of global ocean mixing inferred from Argo profiles. *Geophys. Res. Lett.*, 39.

Whitt, D. and Thomas, L. (2012). Near-inertial waves in strongly baroclinic currents. *J. Phys. Oceanogr.*

Wijesekera, H., Padman, L., Dillon, T., Levine, M., Paulson, C., and Pinkel, R. (1993). The application of internal-wave dissipation models to a region of strong mixing. *J. Phys. Oceanogr.*, 23:269–286.

Winkel, D. P., Gregg, M. C., and Sanford, T. B. (2002). Patterns of shear and turbulence across the Florida Current. *J. Phys. Oceanogr.*, 32(11):3269–3285.

Wu, L. X., Jing, Z., Riser, S., and Visbeck, M. (2011). Seasonal and spatial variations of Southern Ocean diapycnal mixing from Argo profiling floats. *Nature Geosci.*, 4:363–366.

Young, W. and Jelloul, M. B. (1997). Propagation of near-inertial oscillations through a geostrophic flow. *J. Mar. Res.*, 55(4):735–766.